POLITECNICO DI TORINO

Corso di Laurea in Ingegneria Meccanica

Tesi di Laurea Magistrale

Experimental and numerical study of passive solar membrane distillation driven by the heat recovered from a photovoltaic module

Relatori
dr. Matteo Fasano
prof. Pietro Asinari

Giovanni Antonetto
matricola: 242562

Luglio 2019

A mia nonna Adriana,
che avrebbe tanto desiderato accompagnarmi nel mio percorso durante questi anni.

Summary

This thesis investigates the possibility of coupling the photovoltaic (PV) technology with an innovative desalination technique based on passive multi-stage distillation, which is driven by low-temperature heat. The term "passive" distillation is here intended as a process that relies only on evaporation and capillarity without requiring any mechanical or electrical devices. The aim is to demonstrate the possibility to cogenerate both electricity (from the PV module) and distilled water (from the passive distiller). Instead of exposing the distiller to direct sunlight, the necessary heat is recovered from the back side of the PV module. Therefore, other than the cogeneration of electricity and distilled water, a synergic effect can be eventually achieved, since a gain in efficiency of the PV is sought due to the reduction of the panel's temperature. Laboratory experiments are carried out to evaluate the performance and thermal properties of both PV and desalination technologies. Both 1D and 3D modeling approaches are used for interpreting the observed experimental results. In the thesis, also the prototyping work made of design and manufacturing steps is presented, which followed simplicity and cost reduction as main guidelines. The result is a desalination rate of up to 2 l/m^2h under one sun (1000 W/m^2) constant irradiation, and around 1,3 l/m^2h during continuative operation along five consecutive days. Furthermore, a relative photovoltaic efficiency gain of 4,5% is obtained by reducing the panel's temperature by 8 °C. The results are promising for a hypothetical scale-up of the prototype; in fact, the possibility to implement a high-yield, low-cost and easy to use device able to cogenerate both electricity and distilled water by PV and membrane distillation process has been demonstrated. Despite some current issues with reliability and long term performance, this work paves the way to floating installations made of such passive cogeneration units, which could rapidly provide energy and safe water in off-grid areas, especially in case of emergency conditions (e.g. after natural disasters).

Sommario

Questa tesi verte sullo studio di un possibile accoppiamento tra la tecnologia fotovoltaica (FV) con un'innovativa tecnica di desalinizzazione basata sulla distillazione passiva multistadio, alimentata da calore a bassa temperatura. Il termine distillazione "passiva" è qui inteso come un processo che si basa solo su evaporazione e capillarità senza richiedere alcun dispositivo meccanico o elettrico. L'obiettivo è dimostrare la possibilità di cogenerare sia l'elettricità (dal modulo FV) che l'acqua distillata (dal distillatore passivo). Invece di esporre il distillatore alla luce diretta del sole, il calore necessario viene recuperato dal lato posteriore del modulo FV. Pertanto, oltre alla cogenerazione di energia elettrica e acqua distillata, si può ottenere un effetto sinergico, poiché si cerca di ottenere un aumento di efficienza del fotovoltaico grazie alla riduzione della temperatura del pannello. Sono stati effettuati esperimenti di laboratorio per valutare le prestazioni e le proprietà termiche sia del fotovoltaico che delle tecnologie di desalinizzazione. Per interpretare i risultati sperimentali osservati sono stati utilizzati approcci di modellazione 1D e 3D. Nella tesi viene presentato anche il lavoro di sviluppo del prototipo costituito dalle fasi di progettazione e costruzione, in cui semplicità e riduzione dei costi sono state le linee guida principali. Il risultato è una produttività di distillazione fino a 2 l/m^{2}h sotto un'irradiazione costante di 1000 W/m^2 e di circa 1,3 l/m^{2}h durante il funzionamento continuativo per cinque giorni consecutivi. Inoltre, si ottiene un guadagno relativo di efficienza fotovoltaica del 4,5% riducendo la temperatura del pannello di 8 °C. I risultati sono promettenti per un'ipotetica evoluzione del prototipo; è stata infatti dimostrata la possibilità di realizzare un dispositivo ad alto rendimento, a basso costo e di facile utilizzo in grado di cogenerare sia energia elettrica che acqua distillata tramite il modulo FV ed il processo di distillazione a membrana. Nonostante alcuni problemi attuali di affidabilità e di prestazioni a lungo termine, questo lavoro apre la strada ad impianti galleggianti di tali unità di cogenerazione passiva, che potrebbero fornire rapidamente energia e acqua sicura in aree sconnesse dalla rete, in particolare in caso di situazioni di emergenza (ad es. in seguito a calamità naturali).

Acknowledgements

I would like to express my sincere gratefulness to my professor and supervisor Matteo Fasano, who one year ago gave me the opportunity to participate in this ambitious project and recognized in me the capacity to accomplish it. I would also like to acknowledge his involvement in following my work, helping me clarifying my doubts and writing the thesis. Eventually, I would like to say thank for involving me into important meetings during which I met many people and I could proudly show my work.

I would like to say thank to Matteo Alberghini and Matteo Morciano for their precious help in introducing me in the laboratory, teaching me how to use many instrumentation and avoiding me to commit mistakes. I would also like to say thank for providing me their work and direct help for running the experiments and shaping my thesis with essential materials and informations.

I would like to thank Professor Filippo Spertino and his team formed by Gabriele Malgaroli and Alessandro Ciocia for giving their important contribution in the outdoor characterization of the PV module, for which otherwise it wouldn't have been possible to achieve it.

A special thank must be addressed to the ILOOXS® team for their collaboration in the design and manufacturing of the PV module, crucial component of this project.

Eventually, I express my gratitude to my family and everybody who supported me over the years in accomplishing my studies with determination and passion.

Contents

List of Tables

List of Figures

List of Symbols

$_0$	Reference (STC) conditions	
a	Characteristic length of a crystalline unit cell	[Å]
$a(Y)$	Chemical activity at mass fraction Y	
A_{cells}	Total area of the cells of a PV module	[m^2]
b^t	Specific total exergy	[kJkg^{-1}]
D_{iK}	Knudsen diffusion coefficient for species i	[m^{2}s^{-1}]
D_{ij}	Maxwell-Stefan diffusion coefficient for species i in j	[m^{2}s^{-1}]
d_a	Air gap thickness	[m]
d_m	Membrane's thickness	[m]
d_p	Membrane's pore diameter	[m]
E_0	Reference (STC) solar irradiance/specific heat flux	[Wm^{-2}]
E_c, E_v	Conduction (c) and valence (v) energy band	[eV]
E_g	Energetic band gap between valence and conduction energy bands	[eV]
E_s	Solar irradiance	[Wm^{-2}]
FF	Filling factor	
GOR	Gained Output Ratio	
h	Specific enthalpy	[kJkg^{-1}]
h_a	Heat transfer coefficient of air	[Wm^{-2}K^{-1}]
Δh_{LV}	Latent heat of vaporization of water	[Jkg^{-1}]
I_0	Reverse saturation current	[A]
I_{diff}	Diffusion current of a p-n junction	[A]
I_{drift}	Drift current of a p-n junction	[A]
I_L	Light generated current of a solar cell	[A]
I_{mpp}	Maximum Power Point current	[A]
I_{net}	Net current without losses generated by a solar cell	[A]
I_{sc}	Short circuit current	[A]
J	Specific mass flow rate	[kgm^{-2}s^{-1}]
$J_{exp,m}$	Experimental mean specific mass flow rate	[kgm^{-2}s^{-1}]
$J_{sim,ref}$	Reference conditions simulated specific mass flow rate	[kgm^{-2}s^{-1}]
J_{sc}	Short circuit current density of the solar cell	[Am^{-2}]
K	Permeability coefficient of the membrane	[sm^{-1}]
k_a	Thermal conductivity of air	[Wm^{-1}K^{-1}]
k_f	Thermal conductivity of dry fabric	[Wm^{-1}K^{-1}]
k_{layer}	Thermal conductivity of a layer	[Wm^{-1}K^{-1}]
k_{PTFE}	Thermal conductivity of PTFE	[Wm^{-1}K^{-1}]

k_{tape}	Thermal conductivity of tape	[Wm^{-1}K^{-1}]
k_w	Thermal conductivity of water	[Wm^{-1}K^{-1}]
k_B	Boltzmann's constant	[JK^{-1}]
k_I	Temperature coefficient for short circuit current	[A°C^{-1}]
k_P	Temperature coefficient for maximum power	[W°C^{-1}]
k_V	Temperature coefficient for open circuit voltage	[V°C^{-1}]
K_v	Viscous permeability coefficient	[m^2]
Kn	Knudsen number	
$\dot{m}$	Mass flow rate	[kg s^{-1}]
M	Molar mass	[kg kmol^{-1}]
N_A, N_D	Doping densities of acceptor (A) and donor (D) elements	
n	Ideality factor of the solar cell	
n_i	Intrinsic carrier concentration	
N_i	Molar flux of species i	[molm^{-2}s^{-1}]
N_{ion}	Number of ions of an ionic species	
N_P, N_S	Number of cells/modules connected in parallel (P) or series (S)	
$P_{in,distillers}$	Incoming power into the distillers	[W]
$P_{in,eff,distillers}$	Effective incoming power into the distillers	[W]
$P_{distillation}$	Equivalent power needed for distillation	[W]
P_{mpp}	Maximum Power Point power	[W]
P_{solar}	Incoming solar power into the cells	[W]
p_v	Vapour pressure	[Pa]
q	Elementary charge	[C]
q_{Border}	Border contribution to the incoming specific heat flux	[Wm^{-2}]
$q_{Convective}$	Convective losses on the panel	[Wm^{-2}]
q_{el}	Equivalent electric specific heat flux	[Wm^{-2}]
q_{in}	Incoming specific heat flux into the distiller	[Wm^{-2}]
$q_{l,layer}, q_{l,mem}$	Lateral losses in layer or membrane	[Wm^{-2}]
$q_{Radiative}$	Radiative losses on the panel	[Wm^{-2}]
q_{Solar}	Solar specific heat flux	[Wm^{-2}]
$q_{x,Frontal}$	Frontal, x-directed specific heat flux in the panel	[Wm^{-2}]
$q_{y,Lateral}$	Lateral, y-directed specific heat flux in the panel	[Wm^{-2}]
r	Ratio between mass of water and mass of dry fabric	
r_c	Critical value of mass of water in fabric	
R	Universal gas constant	[Jmol^{-1}K^{-1}]
R_s, R_{sh}	Series (s) and shunt (sh) resistances of a cell/module	[Ω]
s	Tape thickness	[mm]
s	Specific entropy	[kJkg^{-1}K^{-1}]
$S_{aluminium}$	Surface of aluminium plates	[mm^2]
$S_{condenser}$	Surface of condensers	[mm^2]
$S_{condensation}$	Surface of condensation	[mm^2]
T_0	Reference (STC) temperature	[°C]
$T_{c14,m}$	Mean temperature in the middle of cells 1 and 4 during prototype tests	[°C]

$T_{cell,m}$	Simulated mean temperature of the cells	[°C]
T_m	Mean temperature of the distiller	[°C]
ΔT	Temperature differential across the distiller	[°C]
$T_{mem,m}$	Mean temperature of the membrane	[°C]
ΔT_{mem}	Temperature differential across the membrane	[°C]
u	Uncertainty	
$U_{distiller}$	Distiller transmittance	[Wm^{-2}K^{-1}]
U_{gap}	Air/tape gap transmittance	[Wm^{-2}K^{-1}]
U_{HS}	Heat sink transmittance	[Wm^{-2}K^{-1}]
U_{layer}	Layer transmittance	[Wm^{-2}K^{-1}]
U_{mem}	Membrane transmittance	[Wm^{-2}K^{-1}]
U_{out}	Output transmittance	[Wm^{-2}K^{-1}]
V_0	Junction potential of a semi-conductor	[V]
V_{mpp}	Maximum Power Point voltage	[V]
V_{oc}	Open circuit voltage	[V]
W_t	Mechanical work	[W]
x_i	Molar fraction of species i	
Y	Mass fraction	
ε	Gray body emissivity	
ϵ_m	Membrane porosity	
η_{II}	Second Law efficiency	
η_v	Dynamic viscosity	[Pa s]
η_{PV}	Photovoltaic efficiency	
$\eta_{Prototype}$	Prototype global efficiency	
$\eta_{Recovery}$	Heat recovery equivalent efficiency	
θ	Carnot's factor	
λ_w	Mean free path of water molecules	[m]
μ_i	Chemical potential of species i	[Jmol^{-1}]
σ	Stefan-Boltzmann constant	[Wm^{-2}K^{-4}]
σ_i	Standard deviation of the mean value measured during test i	
σ_R	Standard deviation of the mean value of the mean values of all the tests	
σ_w	Collision diameter of water molecules	[m]
τ	Membrane tortuosity	
ϕ	Heat flux	[W]
Ψ	Exergetic flux	[W]
Ψ_{irr}	Exergetic irreversibility	[W]

Chapter 1

Introduction: Sustainable water supply

Water is a fundamental resource for the humankind, essentially its basic needs of drinking and eating. However, most of the water goes primarily into food production, industry and eventually household necessities. Depending on the lifestyle and region of the world, about $2000 \div 5000$ litres per day per person are required to satisfy those needs. [1] The water resources employed should be renewable in order to avoid a detrimental impact on the environment. The FAO defines as water *stressed* condition when the renewable water resource available daily per person goes below 4600 l. Water *scarcity* is declared when this amount goes below 2700 l and *absolute scarcity* for less than 1400 l. Today, as also depicted in figure 1.1, 19 countries suffer from water stress, some of which also in Europe; 9 face water scarcity and 21 severe water scarcity. In fact, not only impoverished countries but also developed need to address this issue. This situation concerns 2 billion people all over the planet. [1, 2]

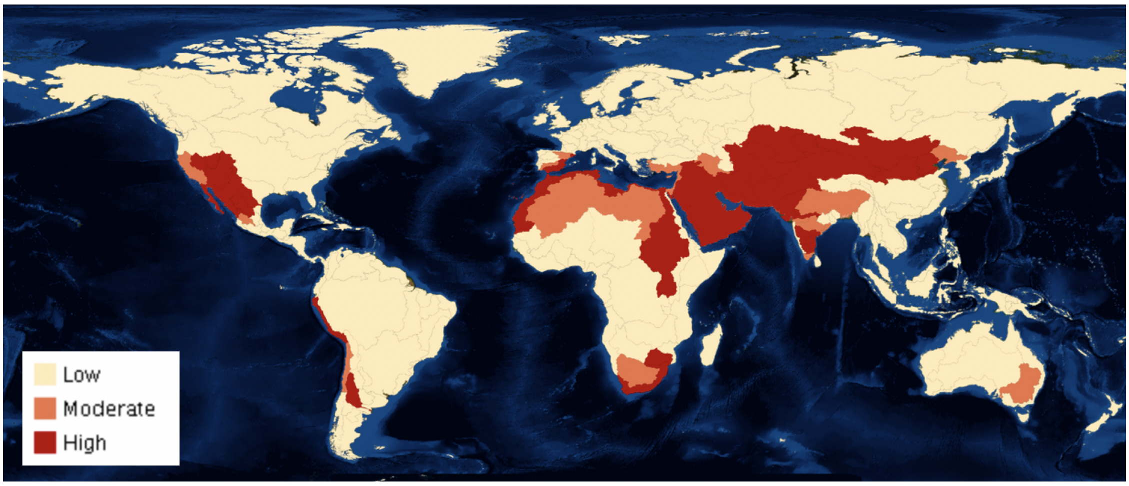

Figure 1.1: Global distribution of water scarcity by major hydrological basin. Adapted from www.fao.org/nr/water/aquamaps/index.html

The expectations for 2050 are a growing population up to 9 ÷ 10 billion people, mostly in developing countries, which means that the water withdrawal will increase further. Over the last century it increased 70% faster. [1] Furthermore, this growing population will accelerate climate change and soil and underground water resources exploitation along with pollution. Climate change has uncertain effects depending on the geographic localization, causing increased aridity or rainfall and extreme meteorological events. [3] An increasing population will lead to a decreasing availability of freshwater. Consequently, water stress and scarcity will be accentuated putting in danger the health and economy of the most affected regions.

A sustainable water supply is the challenge of the century. Sustainability must be both environmental and economic. Water must be provided by technologies able to satisfy the increasing amount of the population but should be sustainable too. Oceans are an endless source of water, but desalination is energetically expensive. Renewable energies must be chosen to develop desalination systems. Solar energy is abundant and very powerful, particularly in areas affected by water scarcity. The energy incoming into the Earth from the sun in some few hours is theoretically enough to satisfy the worldwide consumption for a whole year. [4] Although solar energy is not constantly provided over the days, it is still able to satisfy energetic needs even in areas far from the equator. For example, potentially also UK could meet its energetic needs by using only 1% of its land to install

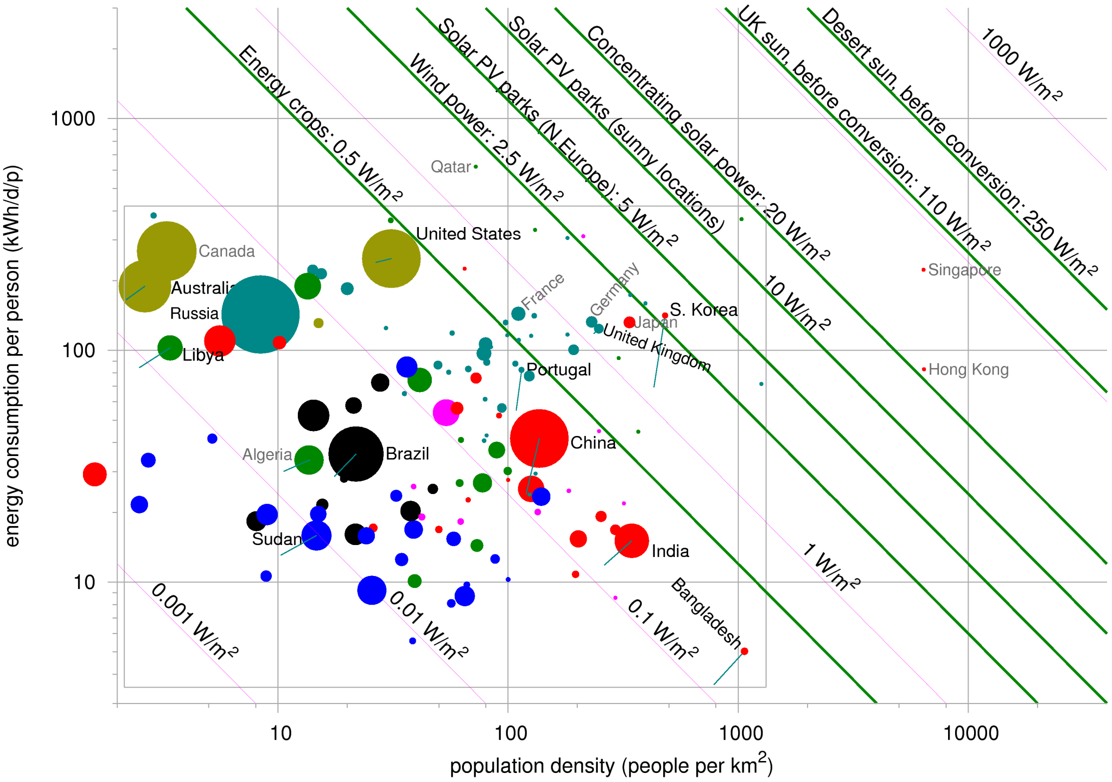

Figure 1.2: Power consumption per person versus population density. Adapted from [5]

solar power plants. [5] This statement can be observed by watching figure 1.2: the diagonal lines are contours of equal power consumption per unit area and UK is close to 1 W/m^2 of power consumed, while the average solar irradiance in the UK is 110 W/m^2. This means that it could harness from the sun the amount of power required by only using about 1/100 of its land. The size of the dots is proportional to the size of the countries, meaning that many big countries could satisfy their needs by using a very small portion of their land.

Taking inspiration from the work originally developed at the Department of Energy at Politecnico di Torino [6], in this work a prototype which implements desalination through solar thermal energy is presented, developed and studied. The solar desalination is carried out in a multi-stage device able to recover the latent heat of vaporization during the condensation of the distillate and to use it to feed the following evaporations throughout the stages. Water feed and collection are driven by capillarity thanks to hydrophilic materials. The materials forming the device are cheap and components easy to assemble, thus its working principle is completely passive. To further enhance the efficiency and pave the way for new and more performing applications, heat for distillation is here provided from the waste heat of a photovoltaic module. Briefly, the prototype shown in this work is a device which encloses into a tailor made structure eight distiller modules in contact with the back side of the photovoltaic panel. The thesis is divided in the following Chapters:

Chapter 2 discusses the photovoltaic technology and applications from a theoretical point of view and an applied one. Furthermore, an overview of the most important desalination technologies is provided to introduce the innovative ones and explain in the detail the theory behind the passive solar membrane distillation of this thesis.

Chapter 3 is dedicated to the testing of the PV module in indoor and outdoor conditions to determine its electric characteristics, develop an algorithm to calculate intrinsic magnitudes and obtain the mathematical model to simulate its behavior in different external conditions.

Chapter 4 is a thorough characterization of the distiller recovering thermal energy from the PV module. Experiments are performed to measure the performance, the heat transfer properties and determine the possible issues of the device. It follows the development of the 1D and 3D thermal models of the overall assembly.

Chapter 5 describes the development of the prototype structure in terms of design, manufacturing and assembly during working operation.

Chapter 6 is eventually dedicated to the testing of the prototype in indoor conditions to evaluate performance and reliability over the time. A modeling interpretation of experiments is also done to provide an energetic and exergetic analysis.

Appendices include insights on photovoltaic and desalination technologies, and detailed results of the experiments, simulations and analysis.

The attached documents include technical drawings of the parts that constitute the PV+distiller prototype.

Chapter 2

State of the art

2.1 Fundamentals of solar cells

Semiconductors are materials that completely revolutionized the world of technology and permitted the development of electronics as we know it today. The early history of semiconductors and photovoltaic effect starts at the beginning of the 19th century. The first official semiconductor dates back to 1874 thanks to the contribution of german physicist K. F. Braun. Semiconductors had been used in a minor way until the end of World War II, after which in 1947 in Bell Telephone Laboratories the first transistor was developed by Nobel prices W. Shockley, J. Bardeen and W. Brattain [7]. Since then, this device and all the other devices related to the same basic principle spread all over the world. One of them is the solar cell which was ultimately conceived in a viable version by G. Pearson, D. Chapin, and C. S. Fuller in 1954 in Bell Laboratories [8]. Its working principles and characteristics are explained in the following subsections.

2.1.1 Theoretical principles of semiconductors and solar cells

A semiconductor is a combination of two layers of doped materials. On one side there is a positively doped material called *p-type* in which some atoms of his microstructure are replaced by elements from the previous group of the elementary table, hence with an electron less, leaving electronic holes inside the framework and generating a net positive charge. On the other hand, the negatively doped material or *n-type* sees part of his atoms being substituted by elements of the subsequent group, letting some free electrons inside the crystal. The layers then are joined in what is called a *p-n junction*. When the junction is made, electrons from the donor atoms of the n-side tend to diffuse towards the p-side, leaving behind them positively charged ions stuck in the crystalline structure. Inversely, holes from the acceptor atoms of the p-side move to the n-side and leave negatively charged fixed ions. This phenomenon is the *diffusion current* of the *majority carriers* (electrons in n-side and holes in p-side) and it comes to an end at a certain point. Free electrons in p-side and holes in in-side are the *minority carriers*. The positive and negative ions that are created in the finite region surrounding the junction cannot move, so they generate an electric field which counters the diffusion current by establishing a *drift current* of the majority carriers. These currents balance each other and the result is the creation of a stable and electrically charged region around the junction called *space charge region* or *depletion region.* The electric charge induces a *junction potential* V_0, whose equation is:

$$V_0 = \frac{k_B T}{q} ln(\frac{N_A N_D}{n_i^2}) \tag{2.1}$$

where k_B is Boltzmann's constant, q the elementary charge, N_A and N_D are the doping densities of the acceptor and donor element and n_i is the intrinsic carrier concentration [7, 9]. A scheme of the p-n junction is shown in figure 2.1.

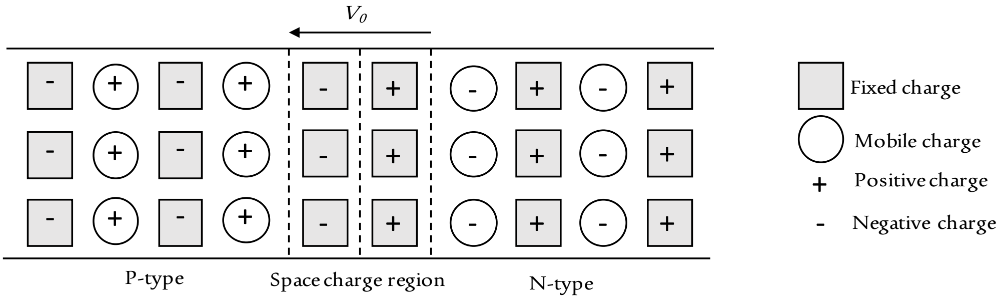

Figure 2.1: Scheme of a p-n junction. Adapted from [9]

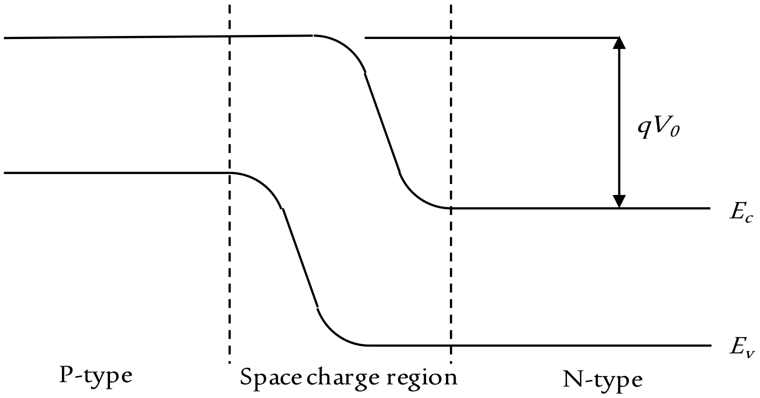

Figure 2.2: Energy band diagram of a p-n junction. Adapted from [9]

Figure 2.2 depicts the energy band diagram in the junction. A flow of electrons from the n-side towards the p-side is only possible if they overcome the junction potential and reach the energetic conduction band of the p-side. By applying a voltage in opposition to the potential barrier, it is possible to overcome the barrier and establish a current. *Forward biasing*, as shown in figure 2.3, consists in connecting a voltage generator with the positive pole to the p-side and the negative pole to the n-side, and applying a voltage larger than V_0 so that the diffusion current is dominant compared to the drift current. Connecting the voltage generator reversing the poles is called *reverse bias*, and operates the semiconductor as an insulator: instead of countering the potential barrier, it raises it.

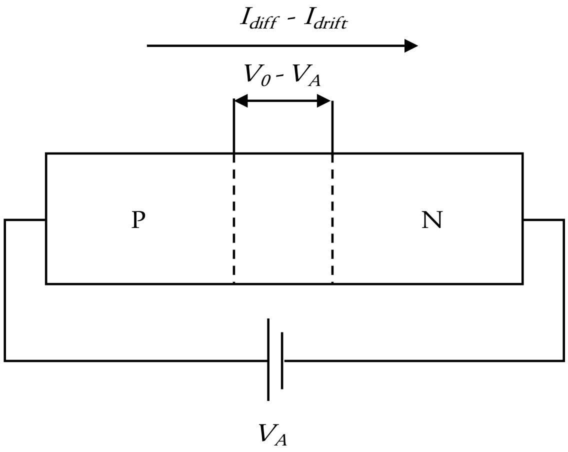

Figure 2.3: Forward bias of a p-n junction. Adapted from [9]

One effect of enlightening a semiconductor of a solar cell is the forward biasing, thanks to the rise of the energy of the conduction band on the n-side, but does not create the useful current looked for. Instead, another current deriving from the drift one is sought. When the light hits the p-n junction, pairs of electrons and holes are created in the space charge region and in both p-side and n-side. Electrons in the space charge region go towards the n-side, under the effect of the junction potential, and inversely for the holes. Outside the depletion region the pairs of electrons and holes created move randomly because no electric forces are present. Part of the electrons in the p-side and close to the depletion region fall inside it and are transported to the n-side, while the rest recombines. Similarly for the holes generated in the n-side, part of them flow to the p-side and the others recombine. Both phenomenons of drift currents contribute to establish a *photovoltage* across the cell and a *light generated current* I_L. When the poles of the cell are connected, both the diffusion and the light generated current flow, but the latter one is superior in magnitude than the diffusion current [9, 10].

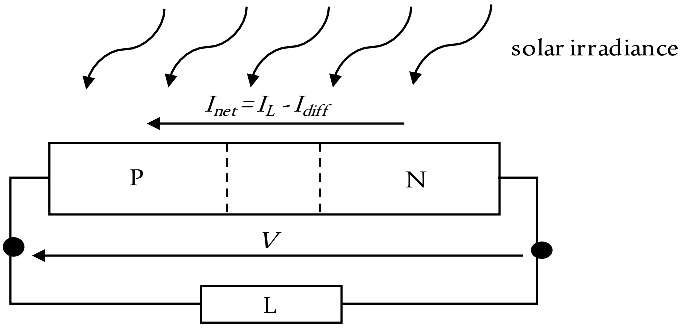

Figure 2.4: Solar cell submitted to light and connected to a load. Adapted from [9]

The expression of the net current flowing is:

$$I_{net} = I_L - I_0(e^{\frac{qV}{k_BT}} - 1) \tag{2.2}$$

where I_0 is the reverse saturation current. As shown in figure 2.4, the cell works as a generator. By varying the load from open circuit to short circuit, it is possible to obtain the I - V and P - V characteristics of the solar cell drawn in figure 2.5, where $P = VI$ is the power generated by the cell.

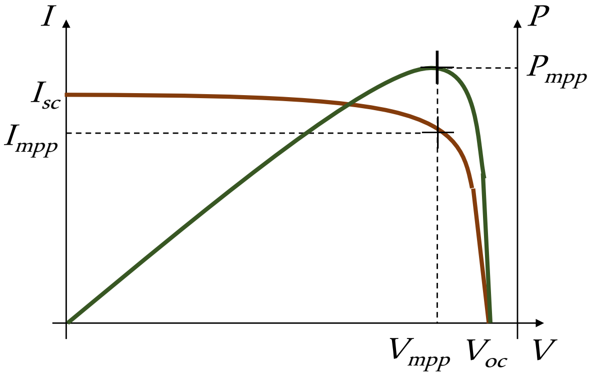

Figure 2.5: Typical $I - V$ and $P - V$ characteristics of a solar cell

When connecting in short circuit the cell, the tension across it is null thus the net current flowing is the *short circuit current* $I_{sc} = I_L$ as stated by equation (2.2). In open circuit, the voltage generated is equal to the *open circuit voltage* V_{oc}. With the condition that current is null, the expression deriving from equation (2.2) is:

$$V_{oc} = \frac{k_BT}{q} ln(\frac{I_L}{I_0} + 1) \tag{2.3}$$

For an optimal magnitude of the resistive load, the cell works at his *Maximum Power Point* (MPP). A parameter that express the performance of the cell is the *filling factor FF*. It is the ratio between the maximum power and the ideal maximum power:

$$FF = \frac{V_{mpp}I_{mpp}}{V_{oc}I_{sc}} \tag{2.4}$$

The quality of the cell is measured by the efficiency η. It is expressed by the ratio between the maximum power produced and the power provided by the sun, which is the product of the solar irradiance E_s and the area of the cell A:

$$\eta = \frac{V_{mpp}I_{mpp}}{E_sA} \tag{2.5}$$

To sum up, a solar cell is a p-n junction able to produce a photovoltage using the photovoltaic effect. Its relevant parameters constitute its ideal model, without losses, which has been exposed until now. In the next subsection a more realistic model is presented.

2.1.2 One diode model of a solar cell

A solar cell is a physical device and, as such, it has a non ideal behavior depending on different types of losses. These losses exist because of limits in the material properties and in its processing capabilities, resulting in losses of photon's energy conversion. The fundamental losses related to the physical limits are listed below [9]:

- **Low energy photons**: photons whose energy is below the *energetic band gap* of the material $E_g = E_c - E_v$ (figure 2.2) do not produce pairs of electron-holes that contribute to the photovoltaic effect, hence all the power provided by these photons gets lost. The entity of this loss is about 23%;
- **High energy photons**: photons whose energy is more than E_g generate pairs of electron-holes but the excess of this energy gets dissipated in heat into the material which represents 33% of the total losses;
- **Voltage loss**: theoretically, the cell could be able to produce a maximum voltage equal to E_g/q but, due to Auger recombinations that provoke heat losses in the lattice [11], the voltage is instead equal to V_{oc}. The ratio between these two voltages is around 0,65 and 0,72;
- **Filling factor loss**: the $I - V$ characteristic of the cell is ideally a rectangle, so with $FF = 1$. In real solar cells, FF is less than 0,89 due to two parameters: the *series resistance* R_s due to all the resistances in the path of the current (e.g. semiconductor, contact between semiconductor and metal plate connection, metal plate), and the *shunt resistance* R_{sh} which is caused by peripheral losses in the cell and due to impurities and defects in the junction.

These previous losses cannot be reduced below a certain limit, while technological issues that limit processing capabilities can be minimized. These secondary type include **reflection**, **incomplete absorption** due to reduced thickness of the cell, **recombination** of pairs of electron-holes when thickness is excessive and optical losses due to **metal coverage**.

The one diode model is an electric model with concentrated parameters broadly used in the literature to describe the real functioning of the solar cell. It is able to take into account of the losses previously declared inside the electrical components that form it. The components of the scheme of figure 2.6 are listed below:

Ideal current source: the first element is an ideal current source which provides a value of light generated I_L proportional to the solar irradiance E_s; it considers already the optical losses.

Diode: a diode connected in parallel simulates the effect of the recombination in that part of the semiconductor matrix far enough from the space charge region. Although a two-diode model exists and takes into account also of recombinations in the space charge region, these are negligible and a more simple one diode model is sufficient. This component also behaves differently depending on the temperature.

Shunt Resistance: in parallel there is a shunt resistance as described previously.

Series Resistance: a resistance connected in series which role is declared previously.

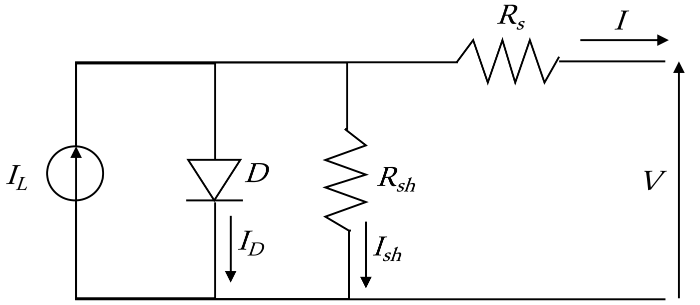

Figure 2.6: One diode model scheme

The equation of the current extracted from the solar cell is the following one [12]:

$$I = I_L - I_D - I_{sh} \tag{2.6}$$

namely:

$$\Leftrightarrow I = I_L - I_0 \left[\exp\left(\frac{q(V + IR_s)}{nk_BT}\right) - 1\right] - \frac{V + IR_s}{R_{sh}} \tag{2.7}$$

where n is the ideality factor, a number between 1 and 2 that depends on the technology of the solar cell. As it can be seen, the current equation is non linear and implicit and is valid for only one cell. In the next section the equations for systems of multiple cells will be shown. To implement the effect of temperature and irradiance in the model, constant coefficients of temperature for the open circuit voltage k_V and for the short circuit current k_I are used in the equations as follows [13]:

$$V_{oc} = (V_{oc,0} + k_V(T - T_0)) \tag{2.8}$$

$$I_{sc} = (I_{sc,0} + k_I(T - T_0))\,\frac{E}{E_0} \tag{2.9}$$

where *0* refers to standard test conditions ($T_0 = 25$°C, $E_0 = 1000 W/m^2$). In chapter 3 more details will be provided concerning the test procedures or to identify the parameters required for the equations above.

2.2 Technologies and applications of PV panels

The technologies to produce solar cells are numerous and vary depending on the sectors of interest. Price and performance are the criteria that influence the choice of the materials, hence the production process, of the photovoltaic cells. The technologies can be classified in three main generations. The first one encompasses all the different types of *silicon wafers* technologies: monocrystalline (Mono c-Si) and polycrystalline (Poly c-Si). These represent

80% of all the solar panels around the world since they are the oldest and popular technology and with high levels of efficiency and reliability. A particularly detailed explanation of Mono c-Si principles and production process will be shown in the following subsection, since it is the technology of the panel object of this work. The second generation refers to the more recents *thin film* based technologies, whose main peculiarity is the low-price for amorphous silicon a-Si, or the very high efficiencies for CdTe, CIGS and GaAs types. In the third generation is possible to find all the brand new technologies developed to solve costs, environmental and health issues that come with the other generations. New materials as perovskite, organic pv's and dye sensitized solar cells can guarantee high efficiencies but still need more improvements in stability over the time [14]. A summarizing table of the efficiencies, filling factors and other characteristics of the previous technologies can be found in Appendix A.

2.2.1 Silicon wafer technologies

The silicon wafer technology rely on the peculiarity of the Si crystalline structure. The atomic arrangement is based on a fcc unit cell combined with another fcc cell displaced by 1/4 in each x, y and z direction. In formulae, the resulting unit cell of characteristic length a is expressed by [9]:

$$fcc(x,y,z) + fcc(x+\frac{1}{4}x, y+\frac{1}{4}y, z+\frac{1}{4}z) \tag{2.10}$$

The characteristic length a for Si measures 5,43Å. Each atom is combined with other four atoms inside a tetrahedral structure as shown in figure 2.7a.

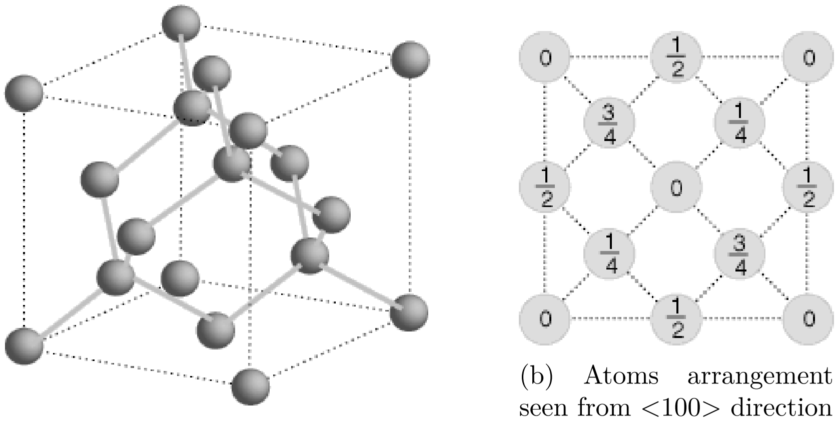

(a) Unit cell for Si

(b) Atoms arrangement seen from <100> direction

Figure 2.7: Crystalline structure of Si. Adapted from http://hyperphysics.phy-astr.gsu.edu/hbase/Solids/sili2.html

In figure 2.7b is displayed the atomic arrangement seen from a <100> direction. The numbers represent the distance of the atoms from the (100) plane in terms of fractions of a. During the production process, the molten silicon is mixed with dopant substances as B or P, which replace some of the Si atoms of the crystalline structure. This enables the conductivity providing free electrons or free holes.

Silicon is the second most abundant element on Earth after oxygen. It is found mainly under the shape of silicon oxide SiO_2, derives from most of the common minerals found on the planet (e.g. quartz, sand, silicates), and is accompanied by many different impurities. Therefore the interest for this material comes from the very low cost of extraction at the beginning of the process. From the minerals, metallurgical silicon is obtained by heating them mixed with carbon at 1900 ℃. The first step in the production of pure silicon for electronic purposes is its purification. [9, 16] Metallurgical silicon powder is reacted with hydrochloric acid at 300 ℃. The exothermic reaction produces gaseous trichlorosilane and hydrogen:

$$\mathrm{Si(s)} + 3\,\mathrm{HCl(g)} \longrightarrow \mathrm{SiHCl_3(g)} + \mathrm{H_2} \tag{2.11}$$

Thanks to fractioned distillation, high purity gases of trichlorosilane are obtained. Two different processes then can be chosen to produce pure solid Si. The most common is to convert trichlorosilane into solid silicon inside a *Siemens type reactor*. Thin rods of silicon are introduced inside the reactor and heated at around 1100 ℃ and exposed to the trichlorosilane and hydrogen mixture gas. H_2 reduces $SiHCl_3$ to solid Si and deposits on the rods as follows:

$$2\,\mathrm{SiHCl_3(g)} + 2\,\mathrm{H_2} \longrightarrow 2\,\mathrm{Si(s)} + 6\,\mathrm{HCl(g)} \tag{2.12}$$

The rods grow until they reach 30 cm of diameter, then the process is stopped and the rods are removed from inside the reactor.

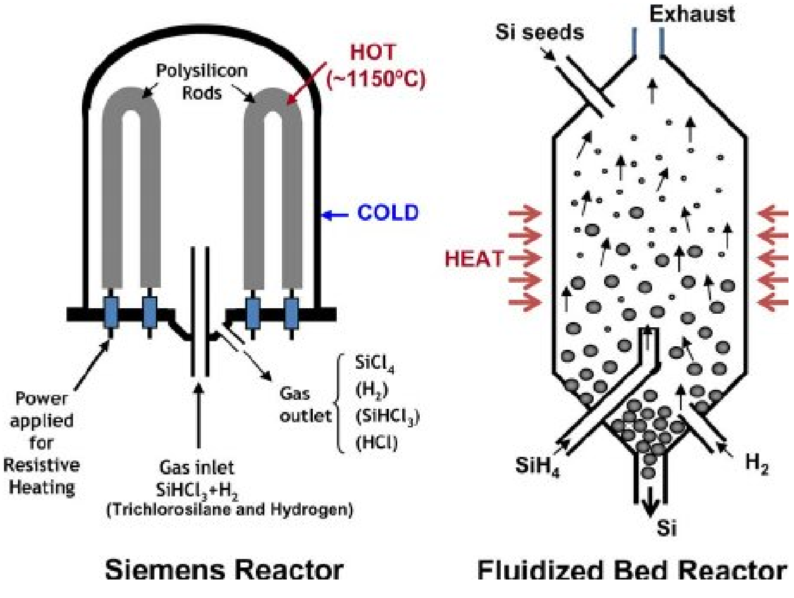

Figure 2.8: Schemes of Siemens type and Fluidized-bed reactors. Adapted from [16]

The alternative process is to decompose $SiHCl_3$ into silane and use it inside a *fluidized-bed reactor* (FBR):

$$4\,\mathrm{SiHCl_3(g)} \longrightarrow \mathrm{SiH_4(g)} + 3\,\mathrm{SiCl_4(g)} \tag{2.13}$$

Inside this reactor, Si seeds are kept in suspension by a mixture of silane and hydrogen gas flowing upwards and heated at 600 °C. The reduction of silane and deposition of solid Si over the seeds occurs as follows:

$$\mathrm{SiH_4(g)} \longrightarrow \mathrm{Si(s)} + 2\,\mathrm{H_2(g)} \tag{2.14}$$

The pure silicon seeds grow up to 2 mm until they become too heavy to float and fall automatically in the collector. While the first process is more common, the second has many advantages as it is continuous, hence with higher productivity, permits to obtain purer Si and requires less energy. The obtained solid Si is amorphous and needs further processes in order to become useful for electronic devices. A scheme of Siemens type reactor and FBR is shown in figure 2.8.

The production of silicon wafers starts from the solid silicon that has just been produced in the above mentioned processes. Different techniques exist depending on the type of wafers required.

- **Mono-crystal Si**: The best available Si technology for semiconductors is represented by Mono-c Si. In fact, for the conduction of electrons, grain boundaries, impurities - excepted from dopants - and defects, are counterproductive. The *Czochralski method* (CZ) is the most common technique to produce unique crystals (up to 90% of the total production). It consists in melting the pure silicon at 1400 °C and adding dopants (adding *boron* to produce p-type semiconductor, or *phosphorous* for n-type) and a small amount of interstitial oxygen to provide mechanical strength. The molten material is contained in a rotating quartz crucible. The seed crystal, i.e. the stick from where the crystallization of the Si starts, is dipped into the molten material. Its shape determines the orientation of the crystal ingot which must be <100> or <111>. At this point the formation of the ingot starts and the seed is rotated in the opposite direction and pulled out slowly as shown in figure 2.9. Both speeds of rotation and pull-out determine the amount of defects. The diameter and length of ingots is quite variable, up to 450 mm in diameter and 2 m in length. The ingots are then cut in thin wafers by inner diameter sawing (circular saw) or wire sawing. Their thickness depend on their diameter, from 275 μm for 51 mm wide wafers to 925 μm for 450 mm wide wafers. [17]

- **Multi-crystalline Si**: Nowadays 75% of all the silicon cells are Multi-c Si wafers. This trend is due to the extremely reduced price of production compared to Mono-c Si, thanks to a higher output rate of the production process and a greater margin of tolerance. [9] Furthermore, the shape of Multi-c Si wafers is squared, thus it improves the packaging of cells into the solar module. The difference in efficiency of Multi-c Si modules compared to Mono-c Si is in the order of 1% to 2%. In solar PV industry, multi-crystalline ingots are produced with *directional casting* process. Silicon is melted in a box-shaped, SiO-SiN coated graphite crucible. The bottom is cooled and the solidification is controlled in both speed and direction. Crystals in the ingot measure around mm to cm and contain much more impurities than the one obtained with CZ method. Ingots measure 600 x 600 x 200 mm and are cut in smaller blocks depending on the size of the cross section required for the cells. These blocks are then cut into thin wafers.

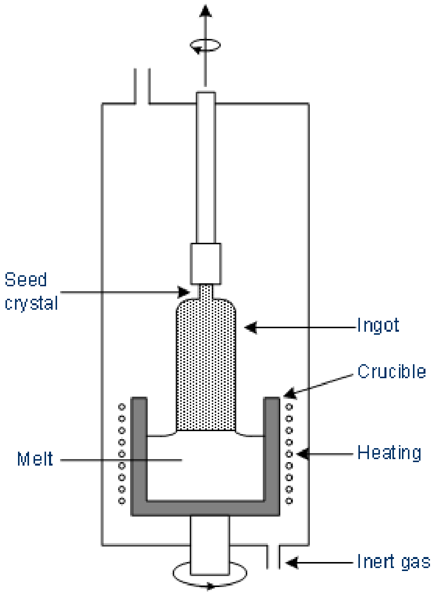

Figure 2.9: Illustration of Czochralski process. Adapted from www.halbleiter.org/en/waferfabrication/singlecrystal/

Once wafers are cut, the next steps to come to the end of the global process and obtain fully functional cells are the following. P-type wafers are used as substrate, or *base*, to form the p-n junction. Since after the process of sawing the surface of the material is damaged, a *chemical etching* is done by dipping the wafer into a NaOH alkaline bath. It cleans the surface and enhances a better anti-reflection property of the cell surface by giving a serrated texture. The formation of the p-n junction occurs exposing the cleaned wafer to a high temperature dopant atmosphere of phosphorous. By diffusion, the n-type region (known as *emitter*), as well as the junction, form all around the wafer with a thickness of less than a micrometer. The n-type region must be kept only onto one of the four sides of the wafer, so the edges are cut and the other face is treated later. On the side that must be conserved, an *anti reflective coating* (ARC), which further reduces the reflection, is applied thanks to a process called *plasma enhanced chemical vapour deposition* (PECVD). This coating is typically made with hydrogenated non-stoichiometric silicon nitride (SiN_x-H). The next step is to provide both faces of the wafer with electrodes by the mean of *screen-printing*, which consists in the deposition of a paste of metals and solvents. On the emitter side, which is the one exposed to sunlight, a grid pattern of Al-Ag paste is laid. On the back side, all the surface is covered with a Al only paste. The wafers are then put into a furnace which starts the *contact firing* process, where the solvents are dried and the metal connections are done thanks to the diffusion of metallic elements. These phenomena happen on both sides, while on the back side the contact firing induces also the removal of the n-type layer. Since Al is also a p-type dopant element, while it diffuses into the lattice, it neutralizes the effect of P, hence neutralizing the n-region. The final result is the photovoltaic cell. A resume of the operations is shown in figure 2.10. Several cells are produced this way starting from from an ingot sliced into wafers. Cells like this are then connected together to form bigger systems as explained in the next subsection.

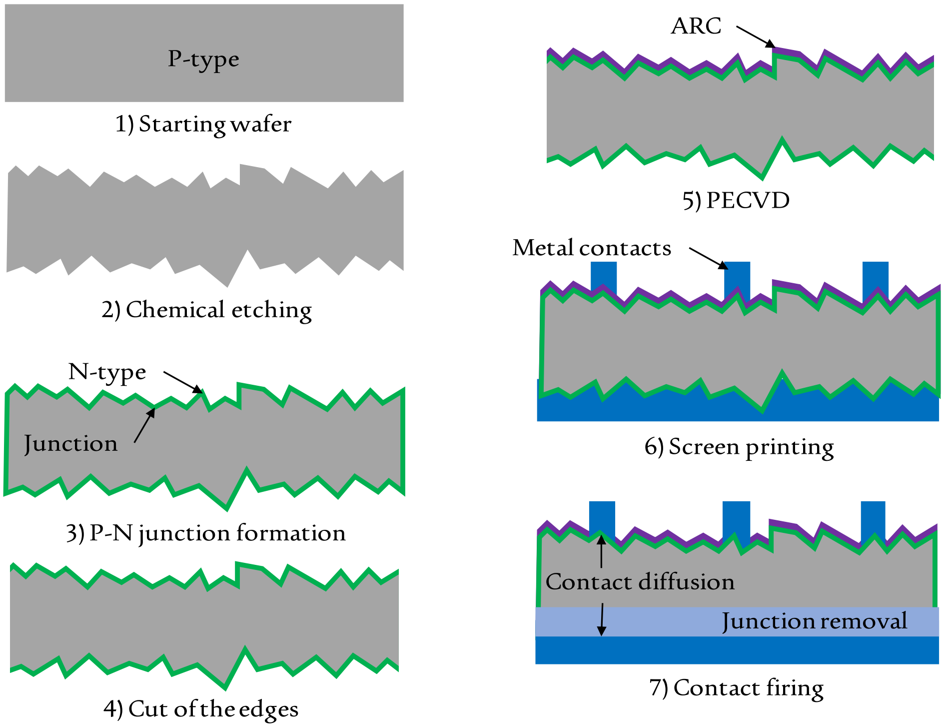

Figure 2.10: Process flow of the manufacturing of solar cells from Si wafers. Adapted from [9]

2.2.2 Solar modules and arrays

Solar cells are the fundamental elements of PV systems. For typical applications, such as small battery chargers, homes, small to large factories until solar panel fields, is necessary to connect several cells in order to provide the amount of power required. Every technology, as stated in tables A.1 and A.2, has its own fixed voltage, current density and efficiency. Only the current is related to the surface of the cell, which is nowadays standardized. Once also this magnitude is set, the only way to generate more power, through voltage and current, is to combine many cells. The interconnection of cells can occur in series and in parallel. A network of a certain number of cells connected and forming a unique device is a *module*. Similarly, modules can be connected in series and parallel to form an *array* of solar modules (figure 2.11). To rise the overall output voltage, series connections are needed. Otherwise, parallel connections rise the total output current. For N_s cells connected in series and N_p cells connected in parallel, the open circuit voltage and short circuit current become [9]:

$$V_{oc,module} = N_s V_{oc,cell} \tag{2.15}$$

$$I_{sc,module} = N_p I_{sc,cell} \tag{2.16}$$

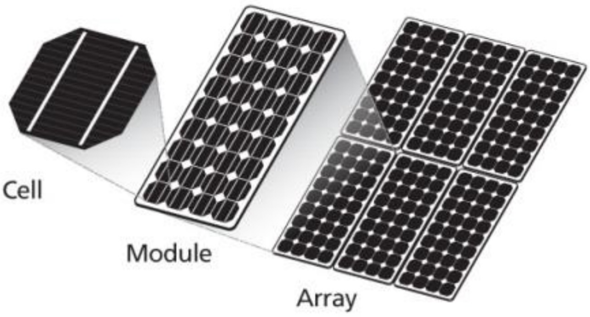

Figure 2.11: Interconnection's levels of solar cells. Adapted from Afrouzi H. N., Vahabi-Mashak S., Zulkurnain A.-M., Mehranzamir K., Salimi B, *Solar Array and Battery Sizing for a Photovoltaic Building in Malaysia*, Jurnal Teknologi, 64:4, p.80, 2013

The same happens for modules and arrays. If considering a module with N_s cells, as typically modules are only made up of only cells in series, and neglecting the shunt resistance R_{sh} which is generally very high, the current produced by the module is expressed as:

$$I = I_{L,cell} - I_{0,cell}\left[\exp\left(\frac{q(V + IN_sR_{s,cell})}{N_snk_BT}\right) - 1\right] \tag{2.17}$$

Similarly, for N_p cells connected in parallel into a module, the output current corresponds to:

$$I = N_pI_{L,cell} - N_pI_{0,cell}\left[\exp\left(\frac{q(V + IR_{s,cell}/N_p)}{nk_BT}\right) - 1\right] \tag{2.18}$$

The combination of both series and parallel cells leads to the following expression of the current of the module:

$$I = N_pI_{L,cell} - N_pI_{0,cell}\left[\exp\left(\frac{q(V + IN_sR_{s,cell}/N_p)}{N_snk_BT}\right) - 1\right] \tag{2.19}$$

The above equation is valid when all the cells have the same technical characteristics and are exposed to the same solar irradiance, i.e. have the same V_{oc}, I_{sc} and resistances. When the previous conditions are not respected, *mismatching* between cells occur and is followed by negative aftermaths which can lead to damages. Two different types of mismatches need to be distinguished: mismatching in *series* or in *parallel* [9].

Mismatching in series: When connecting identical cells in series, ideally the current remains the same and voltages are summed up. This means that for different values of V_{oc} per cell, the overall value is just their sum. The problem occurs when the I_{sc} are different. In figure 2.12 are shown the work operating points of two cells 1 and 2 whose short circuit currents are $I_{sc,1} > I_{sc,2}$. In this situation, the current in the circuit is limited by the smallest one, hence inducing a power loss. The power output of the module is lower than the sum of the power of the cells separately. The working point current is obtained by drawing the mirror image of the cell with greater current (cell 1), and by intersecting this curve with the characteristic of cell 2 in the domain of reverse bias, or power dissipator. The voltages then correspond to the intersection of the previous current and the respective $I - V$ curves of cells 1 and 2. The result is that cell 2 is reverse biased and causes a power loss. This loss occurs in cell 2 under the form of thermal heating. In this case, cell 2 is a *hot spot* in the module. If the mismatch between currents is strong, this phenomenon is greater and can lead to severe damages in the reverse biased cell until its break down.

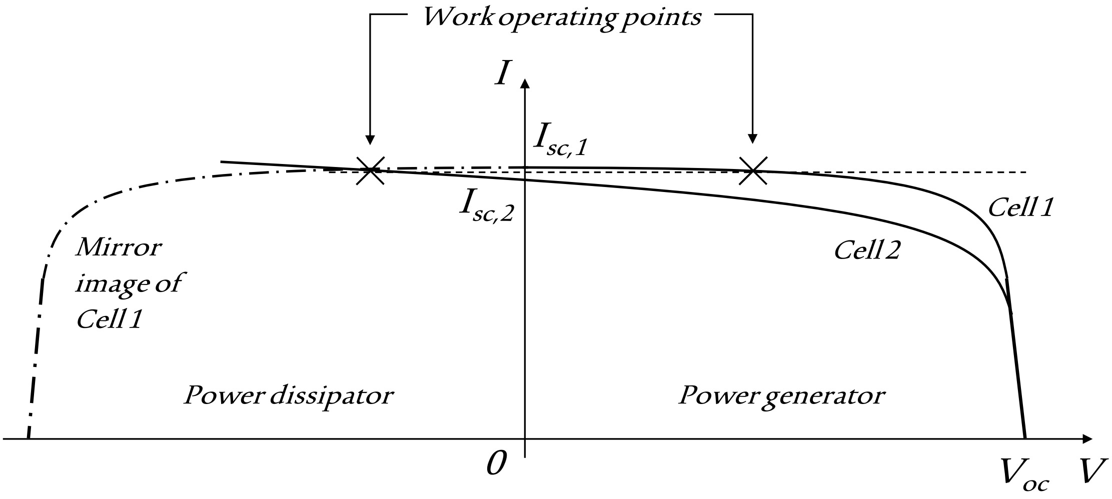

Figure 2.12: Mismatch in short circuit currents in two series connected cells. Adapted from [9]

Mismatching in parallel: For identical cells connected in parallel, ideally the voltage is the same while currents are summed up. Hence, if there is a mismatch in short circuit currents, the total value is just their sum. What happens for a mismatch in open circuit voltages is shown in figure 2.13 for two cells 1 and 2 with $V_{oc,1} > V_{oc,2}$. Cell 2 limits the output current of the module, thus inducing a power loss. The working operating points are obtained similarly as how it has been done for series mismatching. The result is that cell 2 is forward biased by the greater voltage of cell 1, which constitutes the power loss before mentioned. Forward biasing is not harmful for the cell. This problem is more typical in solar arrays, as usually in modules cells are connected in series while in arrays both set-ups are common.

Mismatch between the properties of similar cells or modules are due to:

- partial shading of cells or modules;
- differences in cells' processing during manufacturing;
- aging of cell's materials due to prolonged exposure to UV light;
- damages.

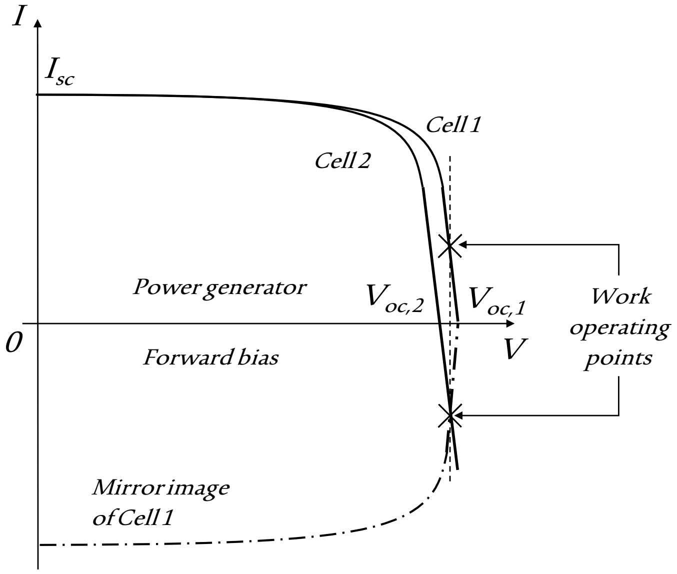

Figure 2.13: Mismatch in open circuit voltages of two parallel connected cells. Adapted from [9]

It turns out that an extreme care must be taken during the manufacturing of cells and modules and during the installation of arrays. A particular care should be taken also in the maintenance of the system. For normal outdoor working conditions, as stated in [18], nowadays solar panels are guaranteed 25 years, corresponding to a loss in efficiency of 0,8%/year until the reaching of a total loss of 20%. This value is the mean value measured for all the commercial technologies available and it lowers to 0,7%/year for Si-based technologies.

2.3 Desalination: a brief overview

Water desalination is the process by which mineral salts are removed from a solution of salted water. Feed water can come from seawater, brackish water, rivers and industrial feed or process waters. The history of desalination is older than 2000 years, with first documented methods described by Aristotle back in 4th century B.C. Its development slowly continued during the centuries, seeing its first industrial application in 1872 in the mine of Las Salinas, Chile, designed by Swedish engineer C. Wilson. However, the development kept a slow pace until the end of World War II. In 1952 the Office of Saline Water (OSW) was created in the United States as an institution addressed to research in the desalination field. Since then, the growth of this market took a rising pace as shown in figure 2.14 [19].

Many techniques exist for this purpose and can be classified depending on the leading phenomenon of the process or on the nature of the energy source [20]. The phenomena involved are phase changes in water, such as evaporation or crystallization, and membrane filtration (see figure 2.15). Desalination with evaporation is commonly know as *distillation*

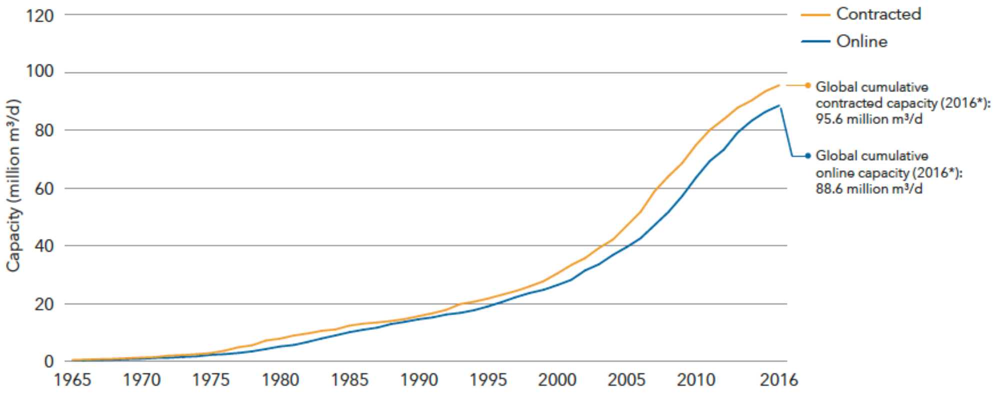

* Values through June 2016

Source: GWI DesalData / IDA

Figure 2.14: Cumulative worldwide online and contracted desalination capacity from 1965 to 2016. Adapted from *IDA Desalination Yearbook 2016-2017*, Water Desalination Report.

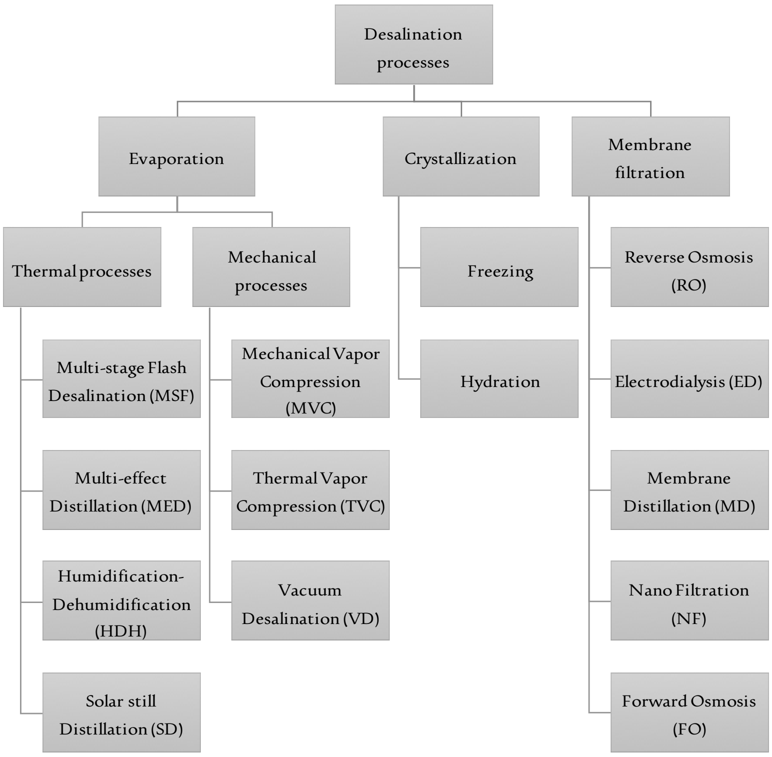

Figure 2.15: Desalination technologies classified by process. Adapted from [20]

and consists in evaporating the salt water and collecting the pure condensate. The nature of the energy sources to drive the phenomenon can be thermal, mechanical, electric or chemical (see figure 2.16). The source of these energies can be supplied by *passive* systems, in which only natural processes are featured, or *active* systems, which operate thanks to electro-mechanical components.. Nowadays, active systems participate almost for the totality of the worldwide production of desalinated water, while innovative technologies that include passive systems and renewable energies are being developed. In the next subsections will be presented the commercial technologies on one hand, and the emerging solutions on the other.

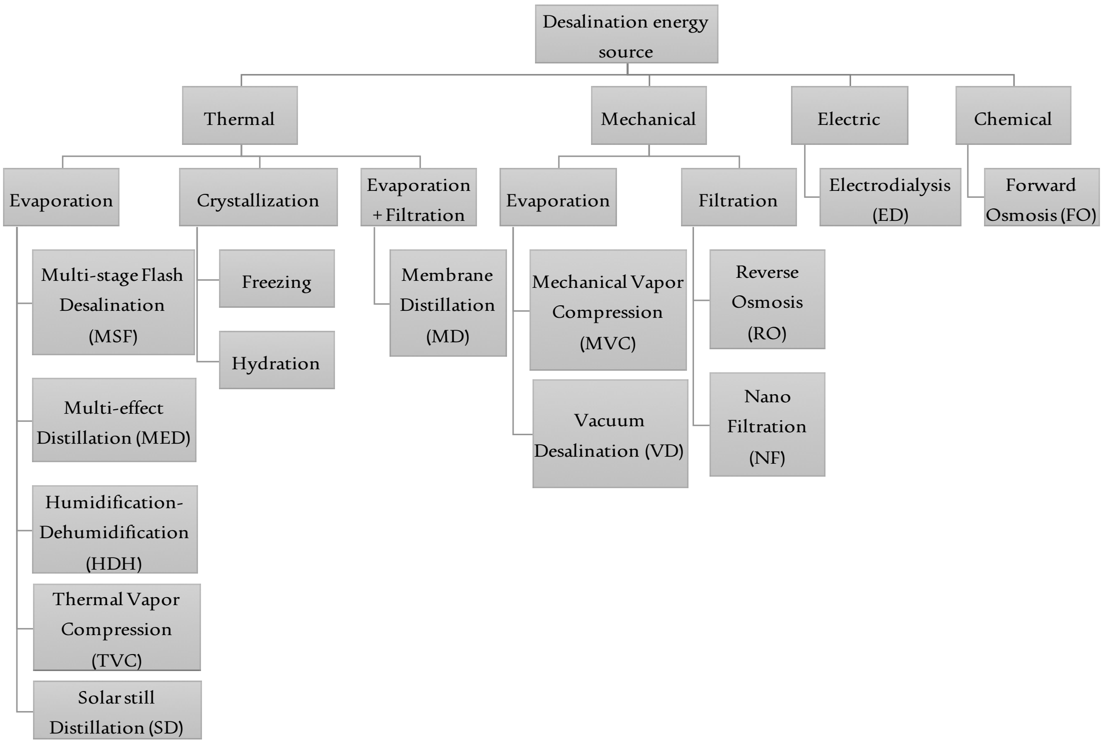

Figure 2.16: Desalination technologies classified by energy source. Adapted from Kabeel A. M. et al., *Water Desalination Using a Humidification-Dehumidification Technique: A Detailed Review*, Natural Resources, 4, p. 287, 2013.

2.3.1 Commercial desalination technologies

The most typical desalination technologies at commercial scale include: thermal/mechanical technologies such as Multi-stage Flash Distillation (MSF), Multi-effect Distillation (MED), Thermal Vapour Compression (TVC) and Mechanical Vapour Compression (MVC); membrane separation technologies such as Reverse Osmosis (RO), Electrodialysis (ED), Electrodialysis Reversal (EDR) and Nanofiltration (NF) [21]. A review on the contribution of each of these technologies to the worldwide production of desalinated water is shown in figure 2.17.

RO, MSF and MED, accounting for more than 90% of the global production, are introduced briefly in the next lines [23]:

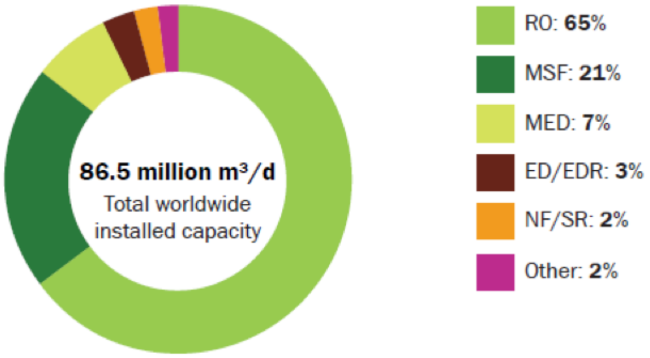

Figure 2.17: Desalination technology contribution to worldwide desalinated water production in 2014. Adapted from *The First Global Integrated Marine Assessment: World Ocean Assessment I*, Division for Ocean Affairs and the Law of the Sea, Office of Legal Affairs, United Nations, 2016.

Multi-stage Flash Distillation (MSF): MSF is the most common thermally driven technology. It works with heat and sub-atmospheric pressure. Saline water evaporates in each stage under the effect of heat and reduced pressure, technically called *flashing*. The vapour condenses on the cold pipes of saline feed water, which crosses every section and is collected in trays. The latent heat is recovered and gives additional heat to the feed water before getting into the main heater and later entering every stage. The number of stages is between 15 and 25.

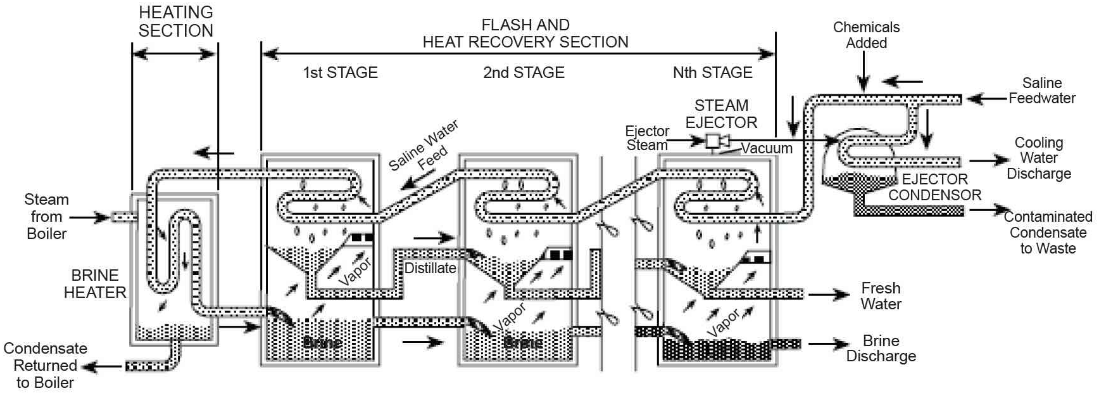

Figure 2.18: Scheme of a Multi-stage Flash Distillation plant. Adapted from [23]

Multiple Effect Distillation (MED): MED relies on multiple chambers like MSF, but optimizes the reuse of latent heat inside each chamber or *effect*. Each stage has decreasing temperatures and pressures in order to always guarantee the evaporation. Saline water is sprayed over a hot pipe in the first chamber. Vapour gets through a pipe and condenses inside the next stage, releasing the latent heat which is totally used to boil the saline water sprayed over the pipe in the next stage. This process is repeated over 8 to 16 stages. MED is less energy demanding than MSF.

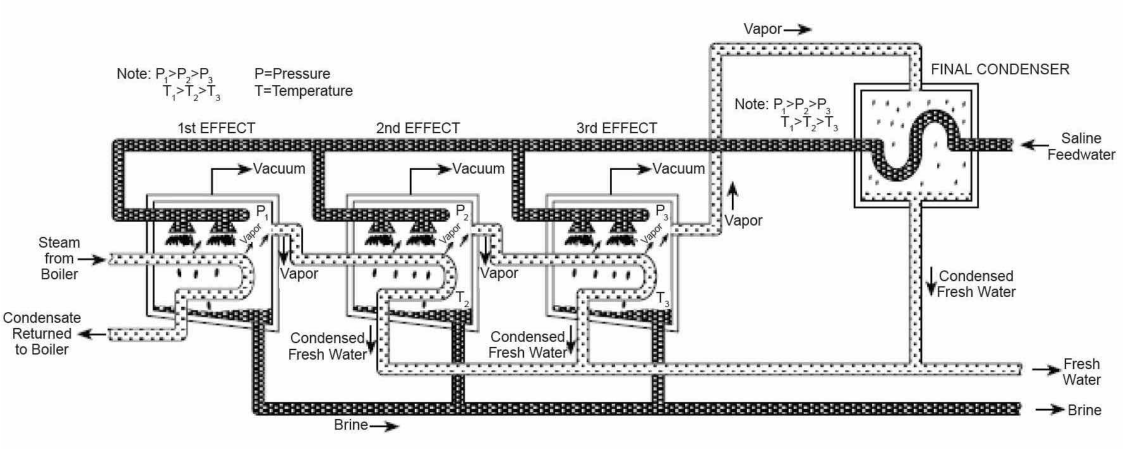

Figure 2.19: Scheme of a Multi Effect Distillation plant. Adapted from [23]

Reverse Osmosis (RO): RO is a membrane driven technique for desalinating water. The principle is to overcome the osmotic pressure that exists when two solutions with different salinity are kept in contact with a semipermeable membrane. Osmosis tends to attract the solvent in the salty solution through the membrane. By applying a hydraulic pressure on the salty side, the phenomenon can be reversed and desalination achieved. RO does not require thermal energy, is low energy demanding, and is able to remove up to 99,8% of the total dissolved solids. RO needs a pre-treatment of the feed water in order to prevent damages to the membranes or reduced performances because of scaling and fouling.

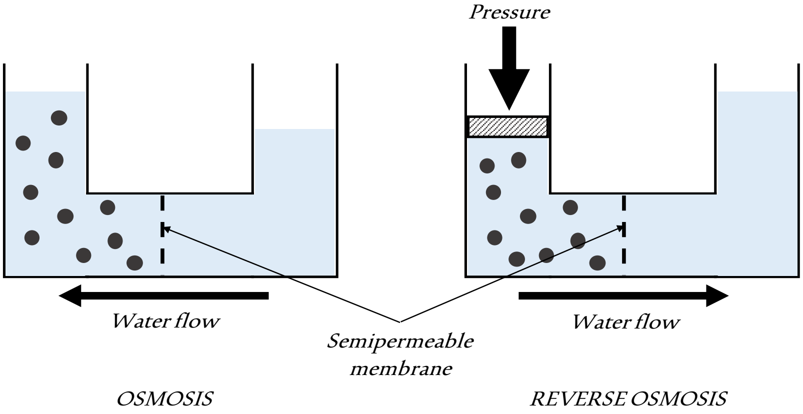

Figure 2.20: Osmosis and Reverse Osmosis comparative scheme

All the above mentioned technologies rely on active systems, thus demanding mechanical moving devices, artificial heat sources and electric power - which could be provided by fossil fuels - large initial investments and subsequent ordinary and maintenance costs. Trained workforce is also required to run the plants. Only large facilities justify their construction by reducing the price per cubic meter of pure water produced (see table 2.1). In the next subsection, recently developed techniques which are characterized by low cost, low energy and low technical efforts are presented.

Table 2.1: Overview upon key data on commercial desalination technologies. Reprinted from [24]

CONVENTIONAL WATER DESALINATION				
Technology	**MSF**	**MED**	**RO**	**ED**
Energy input	Heat + Electricity	Heat + Electricity	Electricity	Electricity
Feed water	> 60% Sea W + Brackish W; RO needs pre-treatment			Brackish W
Energy use	80,6 $\text{kWh}_\text{t}/\text{m}^3$ + 2,5-3,5 $\text{kWh}_\text{e}/\text{m}^3$	80,6 $\text{kWh}_\text{t}/\text{m}^3$ + 1,5-2,5 $\text{kWh}_\text{e}/\text{m}^3$	3,5-5 $\text{kWh}_\text{e}/\text{m}^3$	1,5-4 $\text{kWh}_\text{e}/\text{m}^3$
Operation temp.	90-110 °C	70 °C	Room temp.	Room temp.
Average plant capacity	4000-5000 m^3/day			
Largest plant capacity	800000 m^3/day			
Waste	Brine (high salinity water)			
Desalination Costs	**Typical current international values for new installed capacity**			
Capital cost per unit	800-1500 $/$\text{m}^3$day, variable depending on local labor cost, interest rate and technology			
O&M cost per year	1,5-2,5% of the investment cost per year			
Production cost	1-2 $/$\text{m}^3$ (0,5 $/$\text{m}^3$ for large plants), depending on energy cost and location			

2.3.2 Innovative desalination technologies

The actual challenge is to provide freshwater at a low price, reducing the carbon footprint and, if possible, also with simple and self-sustaining systems. Very few technologies are partially or purely passive. Although the previously presented commercial techniques can be integrated with renewable energies, here the goal is to show two technologies which are meant to be exploitable for impoverished and remote areas where no prepared personnel is available to run the plant and low-cost is overriding. These technologies must be applicable at small scales which do not justify the construction of large facilities. The techniques are Solar Distillation (SD) and Membrane Distillation (MD).

Solar Distillation (SD): The most antique technique is SD using *solar stills* which can be purely passive. It is based on the simplest and intuitive way of making distilled water by taking inspiration from nature. Again, already Aristotle described the daily cycle of evaporation, forming of clouds and return of freshwater under the shape of rain [19]. Starting from this simple principle, solar stills are implemented to replicate the same phenomenon. A solar still is basically made of a basin which contains the non-potable water: this one can be salted or brackish water. A tilted transparent cover made of glass or plastic lets the sun rays pass through it and heat the water. Vapour condenses when comes into contact with the cover and, thanks to gravity, the generated water flows down and is collected at the base of the cover.

In figure 2.21 is shown one of the simplest designs of solar stills, although many other configurations exists. [22] Furthermore, more optimized designs have been implemented over the time, rising the performance of this technology which is limited by

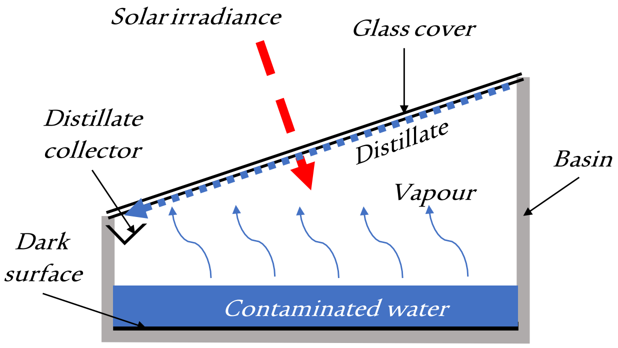

Figure 2.21: Scheme of a single slope, single-effect passive solar still

the waste of the latent heat of evaporation. The loss occurs during the condensation. Some designs, called *multi-effect*, allow to reuse part of the latent heat, contrary to *single-effect* stills which lose it completely. For this reason, passive solar stills are largely inefficient and their performance is strongly limited.

Membrane Distillation (MD) [25]: MD is a hybrid thermal/membrane technique. Thermal energy heats the feed water. The feed side is separated by a hydrophobic membrane from the permeate side. Vapour is generated and is driven through the membrane because of a gradient in temperature between the feed and permeate water, which causes a gradient in vapour pressure.

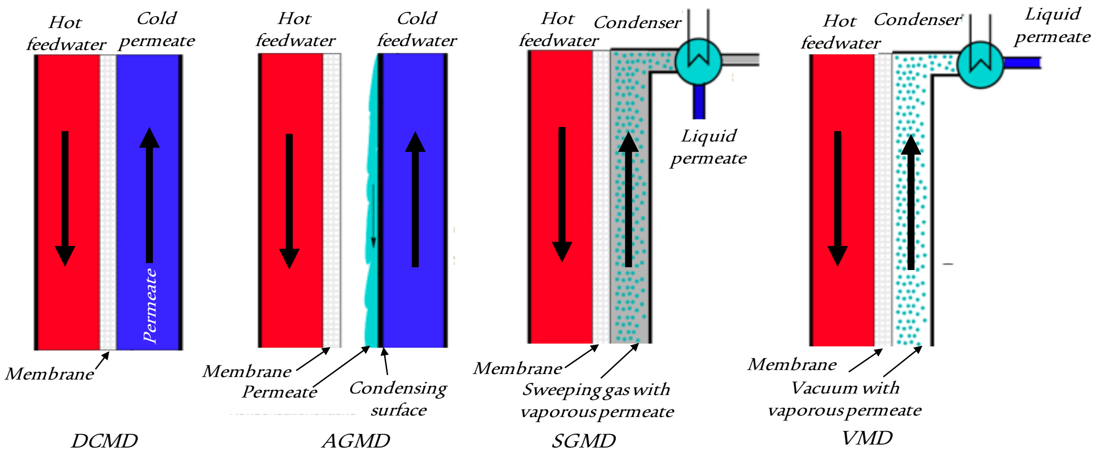

Figure 2.22: Membrane distillation configurations. Adapted from Koschikowski J., *Entwicklung von energieautark arbeitenden Wasserentsalzungsanlagen auf Basis der Membrandestillation*, Fraunhofer Verlag, 2011 .

Liquid water cannot cross the hydrophobic membrane, hence only the vapour phase passes through it, leading to a *distillation* process. Different configurations exists to generate the vapour pressure gradient across the membrane. The most common and simple is Direct Contact Membrane Distillation (DCMD), where feed (hot) and permeate (cold) flows are kept in direct contact with the membrane. DCMD is the simplest to implement, but its yield suffers from direct heat conduction losses across the membrane. Alternatively, the condensate can be collected on a separate surface. In Air-Gap Membrane Distillation (AGMD), the condensation surface is separated from the membrane by stagnant air and is cooled by a cooling fluid, which can be the same feed water that later evaporates. When the permeate condenses on the surface, it releases its latent heat and gives additional heat to the feed stream. AGMD enables to reduce heat losses but increases mass transfer resistances. With Sweeping Gas Membrane Distillation (SGMD), a stream of inert gas carries the permeate outside the membrane module where it later condenses. This way, mass transfer resistances are reduced but a larger condenser is required to condense a small amount of water inside a large volume of gas. Similarly, instead of using a gas, vacuum can be employed to replicate the mechanism in Vacuum Membrane Distillation (VMD). MD works with low temperatures and does not need additional pressure. It can be coupled to renewable energy sources, like solar collectors to heat the feed water and PV panels to provide the electric energy to drive the pumps. Furthermore, the distillation is theoretically complete, leaving behind ions, macromolecules, colloids, organic compounds, etc. Low mass flow rates in comparison to typical active systems, membrane fouling and degradation are the challenges that need to be overcome.

The above mentioned technologies demonstrate that is possible to distill water with self-sustaining devices for both cases and also at a low price when referring to SD. However, if SD is known to have a very little productivity, MD as it is conceived until today is more productive but needs mechanical parts like pumps to work, which need maintenance. Furthermore, other competing technologies based on renewable energy sources exist and show good performances (see table 2.2). In the next section, a fully passive solar membrane distiller is presented in both its technical and theoretical aspects.

Table 2.2: Overview upon key data on commercial desalination technologies. Acronyms' meaning are: Solar Distillation (SD); Multiple Effect Distillation (MED); Concentrated Solar Power (CSP); Membrane Distillation (MD); PV (Photovoltaic); Reverse Osmosis (RO); Electrodialysis (ED); Seawater (SW); Brackish water (BW). Reprinted from [24]

<table>
<tr><th colspan="8">RENEWABLE WATER DESALINATION</th></tr>
<tr><th>Technology</th><th>SD</th><th>Solar MED</th><th>Solar MD</th><th>Solar CSP/MED</th><th>PV/RO</th><th>PV/ED</th><th>Wind/RO</th></tr>
<tr><td>Development Status</td><td>Appl.</td><td>Appl./R&D</td><td>R&D</td><td>R&D</td><td>Appl./R&D</td><td>R&D</td><td>Appl./R&D</td></tr>
<tr><td>Energy input kWh_e/m^3</td><td>Solar</td><td>1,5</td><td>0</td><td>1,5-2</td><td>0,5-1,5 BW</td><td>3-4 BW</td><td>0,5-1,5 BW</td></tr>
<tr><td>$+kWh_t/m^3$</td><td>passive</td><td>+ 27,8</td><td>+ 55,6</td><td>+ 16,7-19,4</td><td>4-5 SW + 0</td><td>+ 0</td><td>4-5 SW + 0</td></tr>
<tr><td>Current capacity m^3/day</td><td>0,1</td><td>1-100</td><td>0,1-100</td><td>>5000</td><td><100</td><td><100</td><td>50-20000</td></tr>
<tr><td>Production cost $/$m^3$</td><td>1,3-6,5</td><td>2,6-6,5</td><td>10,4-19,5</td><td>2,3-2,9</td><td>6,5-15,6</td><td>10,4-11,7</td><td>3.9-9.1</td></tr>
</table>

2.4 Passive solar membrane distillation

In this work, a unique and breakthrough technology based on membrane distillation is studied to provide desalinated water. As stated in subsection 2.3.2, Membrane Distillation has been implemented only as an active system. Here, the difference relies on the fact that MD is driven only by natural phenomenons. The idea was conceived by the engineering research team SMaLL, Department of Energetics at Politecnico di Torino (Italy) back in 2016. After two years of research and development, the official publication came out in December 2018, showing very promising results in the field of ecologically and economically sustainable desalination [6]. In this section, the first part is dedicated in explaining the design and the mechanism of the passive distiller. The second part shows the theoretical principles behind its operation.

2.4.1 Design and mechanism of the passive distiller

The key aspect of this passive solar distiller is simplicity in its design and operating condition. The input power comes uniquely from the sun which provides the useful heat necessary to drive the distillation. The feed of saline water and the collection of the product is driven by capillary forces exerted by the hydrophilic cloths employed for this purpose. The separation between saltwater and freshwater is guaranteed by the hydrophobic membranes. The device manages to reach high productivities thanks to the reuse of the latent heat of vaporization inside several stages of distillation. Low maintenance is required as the distiller is capable of rinsing by its own, again using natural phenomenons. The bill of materials of such distiller is formed by:

- **Solar absorber** which can be simply a black metal surface, a selective spectral solar absorber (e.g. TiNOX®) or a PV panel as demonstrated in this work;
- **Hydrophilic cloths** made of synthetic microfiber, materials of common use for cleaning;
- **Hydrophobic membranes**. In this work were chosen 0,1 µm microporous PTFE membranes; however, an air gap obtained with a plastic spacer is also a possible solution, as well as a combination thereof;
- **Aluminium sheets**;
- Aluminium **heat sink**.

A cloth for the feed of saltwater, a membrane in between, and a cloth for the collection of distillate constitute the base unit of a *stage*. The distiller here presented has 3 stages, but 10 or more are possible. In figure 2.23 are shown schematically the components and the flows occurring when the distiller is irradiated.

In detail, the sequence of phenomena starts with the feed of saline water in the Evaporator 1. Water overcomes gravity and rises with the help of capillary forces that appear in the hydrophilic cloth dipped in the saltwater. When the water reaches the horizontal exchange surface, heat collected by the solar absorber is conducted through the aluminium

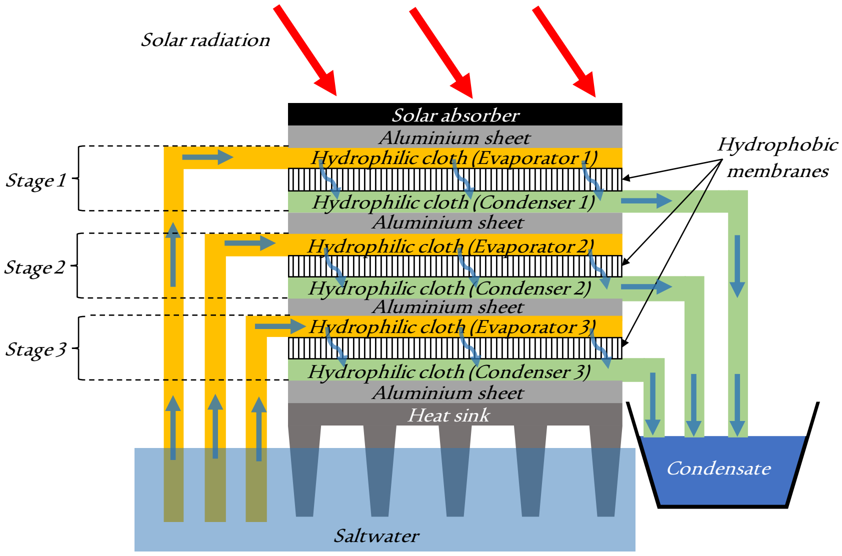

Figure 2.23: Scheme of components and operative flows inside a 3-stage distiller during daytime

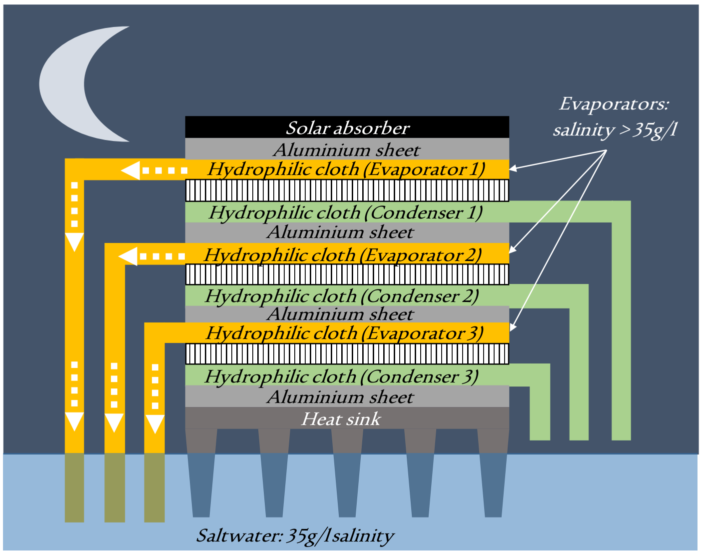

Figure 2.24: Autonomous salt removal during nighttime

and rises the temperature of the saltwater. A gradient in partial vapour pressure of water, due to the gradient of temperature, is established between saltwater in the evaporator and freshwater in the condenser, thus generating a net flux of vapour through the membrane. Liquid water cannot cross the membrane because of its hydrophobicity and because no external pressures are applied as the device works under atmospheric pressure only. Once vapour crosses the membrane, it condenses onto the cloth of Condenser 1, which reaches its full capacity to absorb water and spills the surplus, furthermore helped by gravity, inside the collection basin. When condensation occurs, the latent heat of vaporization is released and conducted through the aluminium plate that separates Stage 1 from 2. This heat is recovered by Stage 2 inside Evaporator 2 and a new process of distillation begins: the sequence is reiterated until it reaches the last stage, here named as Stage 3. The remaining heat of vaporization is dissipated through the heat sink. In this work, it has been chosen to dip the fins of the heat sink in the saltwater, to mimic a possible use onboard a floating device on seawater, in order to get a more efficient convective exchange. By the way, the heat sink can transfer the heat with air as done in previous works. Until here, only the operation during daytime has been explained and the phenomenon of cloth saturation not considered. During the nighttime, no radiation heats the distiller, hence no gradient of temperature exists inside the device and distillation is interrupted.

As shown in figure 2.24, after a day of distillation, salinity inside the evaporators reaches values greater than the saltwater (here considered as seawater with 35 g/l of NaCl). The evaporator cloths are still dipped in the saltwater, so the gradient of salinity, because of Fick's Law of diffusion, tends to vanish, thus re-establishing the initial salinity. This process is furthermore helped by gravity, because of the higher density of salt in comparison with water. This way, the evaporators clean themselves autonomously during nighttime. However, this process of diffusion is slow as declared in [6].

2.4.2 Theoretical principles of membrane distillation

Membrane distillation is a process in which a gradient in temperature generates a gradient in partial vapour pressure of water, Δp_v. Evaporation occurs and only the vapous phase crosses the membrane with a net mass flow rate J [kg/(m^{2}s)] proportional to Δp_v via the permeability coefficient K [kg/(Pa·m^{2}s)=s/m] [6]:

$$J = K\Delta p_v \tag{2.20}$$

Equation 2.20 is the linearized result of the integral of Maxwell-Stefan (M-S) equations combined with the Dusty Gas Model (DGM). M-S with DGM describe the mass transfer of multi-components mixture of gases through porous media, such as membranes or air gaps [6, 26]:

$$-\frac{x_i}{RT}\frac{d\mu_i}{dz} = \frac{x_i K_v \tau}{\eta_v \epsilon_m D_{iK}}\frac{dP}{dz} + \sum_{\substack{j=1 \\ j\neq i}}^{n}\left(\frac{x_j N_i - x_i N_j}{\frac{P\epsilon_m D_{ij}}{RT\tau}}\right) + \frac{N_i}{\frac{P\epsilon_m D_{iK}}{RT\tau}} \tag{2.21}$$

where P and T are the absolute pressure and mean temperature; R is the universal gas constant; x_i, μ_i and N_i are the molar fraction, chemical potential and molar flux of species i respectively; ϵ_m and τ are the medium porosity and tortuosity respectively; D_{iK} is the Knudsen diffusion coefficient for species i and D_{ij} is the M-S diffusion coefficient for species i in j; K_v is the viscous permeability coefficient and η_v the dynamic viscosity of the gas mixture; z is the coordinate along the thickness of the membrane. The term on the left represents the chemical potential driving force for species i. On the right, the first term represents the viscous flow driven by the gradient in absolute pressure across the membrane. The second term represents the molecular diffusion, while the third Knudsen diffusion. In short, molecular diffusion is a flow regime dictated by losses due to molecule-molecule interactions, while in Knudsen diffusion losses are due to molecule-wall interactions. Equation 2.21 can be simplified considering some assumptions:

- The mixture of N_2, O_2 and vapour here is considered only as a mixture of two ideal gases, air (a) and water vapour (w);
- $\mu_w = \mu_w^0 + RT \cdot \ln x_w$, hence $d\mu_w/dz = (RT/x_w)(dx_w/dz)$;
- Since the distiller works at ambient pressure, $dP/dz = 0$ so the viscous term disappears;
- Air is assumed to be stationary inside the membrane since water has a low solubility in air, hence $N_a = 0$;

It is important to highlight that both molecular and Knudsen diffusions participate to the mass transport, so no further simplifications can be done. In fact, Knudsen diffusion can occur in membranes, i.e. when the *mean free path* of water molecules λ_w is comparable to the pore size d_p. λ_w is modeled by the following expression [27]:

$$\lambda_w = \frac{k_B T}{\sqrt{2} P \sigma_w^2} \tag{2.22}$$

where k_B is Boltzmann's constant and $\sigma_w = 2{,}641 \cdot 10^{-10}$ m is the collision diameter of water molecules. The flow regime is described by Knudsen number:

$$Kn = \lambda_w / d_p \tag{2.23}$$

If $Kn < 0{,}01$, only molecular diffusion is considered. For $0{,}01 < Kn < 10$, the flow regime is defined in *transition region* and both Knudsen and molecular diffusion occur. Otherwise, when $Kn > 10$, only Knudsen diffusion takes place. In the case investigated in this work, transition region describes the flow across the membranes. So, the simplified equation is:

$$-\frac{dx_w}{dz} = \frac{RT\tau J \left(1 - x_w + \frac{D_{wa}}{D_{wK}}\right)}{P\epsilon_m D_{wa} M_w} \tag{2.24}$$

where M_w is the molar mass of water, D_{wa} is the diffusion coefficient of water vapour in air and D_{wK} is the Knudsen diffusion coefficient of water vapour. Considering a configuration with a membrane followed by an air gap, the boundary conditions to solve equation 2.24 are:

- $z = 0 \Rightarrow x_w^E = \frac{a(Y_E)p_v(T_E)}{P}$;
- $z = d_m \Rightarrow x_w^i = \frac{a(Y_i)p_v(T_i)}{P}$;
- $z = d_m + d_a \Rightarrow x_w^C = \frac{a(Y_C)p_v(T_C)}{P}$;

where d_m and d_a are the membrane and air gap thicknesses, $a(Y)$ is the activity at a mass fraction $Y = m_{salt}/m_{solution}$, E refers to evaporator side, C to condenser and i to the interface between membrane and air gap. The resulting integral describing the flow in the membrane is:

$$J = \frac{M_w \epsilon_m P D_{wa}}{RT\tau d_m} \cdot ln\left(\frac{1 - x_w^i + \frac{D_{wa}}{D_{wK}}}{1 - x_w^E + \frac{D_{wa}}{D_{wK}}}\right) \tag{2.25}$$

while in the air gap, considered as a porous medium with $\epsilon_m = 1$, the equation is:

$$J = \frac{M_w P D_{wa}}{RT d_a} \cdot ln\left(\frac{1 - x_w^C}{1 - x_w^i}\right) \tag{2.26}$$

As stated in [25, 28], Fuller equation permits to state that $PD_{wa} = 1{,}19 \cdot 10^{-4} T^{1{,}75}$ [Pa·m^2/s]. Knudsen diffusion coefficient of water vapour has the following expression [27]:

$$D_{wK} = \frac{d_p}{3}\sqrt{\frac{8RT}{\pi M_w}} \tag{2.27}$$

Mackie-Meares equation models the correlation between porosity and tortuosity:

$$\tau = \frac{(2 - \epsilon_m)^2}{\epsilon_m} \tag{2.28}$$

Since $x_w \ll 1$, equations 2.25 and 2.26 can be approximated by a first-order Taylor series, thus resulting in equation 2.20. The permeability coefficient of the membrane, which includes the contributions of molecular and Knudsen diffusion, has the following expression:

$$K = \frac{M_w}{RT}\left(\frac{p_a \tau d_m}{\epsilon_m P D_{wa}} + \frac{3\tau d_m}{\epsilon_m d_p}\sqrt{\frac{\pi M_w}{8RT}} + \frac{p_a d_a}{P D_{wa}}\right)^{-1} \tag{2.29}$$

where p_a is the air partial pressure in the membrane pore. In equation 2.20, the vapour pression differential is calculated with Raoult's law:

$$\Delta p_v = a(Y_E)p_v(T_E) - a(Y_C)p_v(T_C) \tag{2.30}$$

Raoult's law shows the effect of salinity and temperature on the overall vapour pressure gradient.

To evaluate the activity, the following expression is employed:

$$a(Y) = \frac{M_{NaCl}(1 - Y)}{M_{NaCl}(1 - Y) + N_{ion} M_w Y} \tag{2.31}$$

in which M_{NaCl} is the molar mass of sodium chloride and $N_{ion} = 2$. For a feed water salinity of 35 g/l, $Y_E = 0{,}035$ hence $a(Y_E) = 0{,}978$, while for distilled water $a(Y_C) = 1$. This implies that a more saline solution reduces the performance of the distiller. The vapour pressures of pure water can be calculated with Antoine's correlation [27]:

$$p_v(T) = \exp\left(23{,}1964 - \frac{3816{,}44}{T - 46{,}13}\right) \tag{2.32}$$

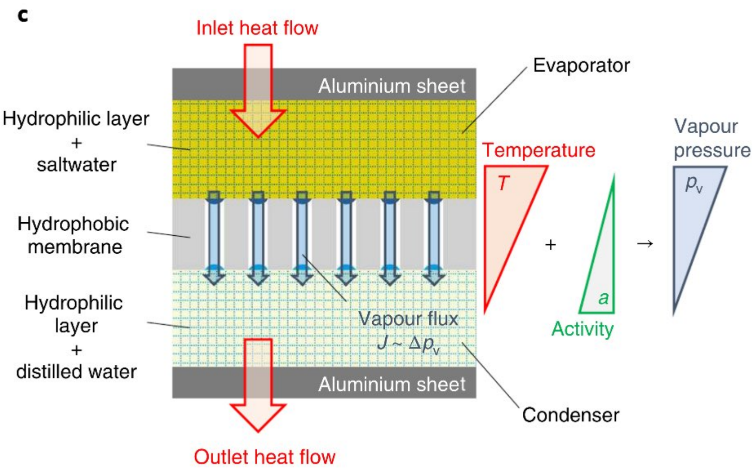

Figure 2.25: Scheme of vapour flux through the membrane in one stage. Adapted from [6]

with p_v in [Pa] and T in [K]. The greater is the temperature in the evaporator, the greater is the vapour pressure thus the flow rate. The contribution of temperature gradient to the permeate flux is much more important than the counter effect induced by an increasing salinity and represented by the magnitude of the activity $a(Y)$ (see figure 2.25). However, greater salinities accelerate the scaling of membranes, which reduces the performance of the process.

Chapter 3

Characterization of the solar module

3.1 Indoor experiments

This work aims to demonstrate the possibility to use a PV module as a solar absorber, in order to provide the necessary heat to run the distillation process. Hence, a cogeneration system is implemented. This part is dedicated to the study of the electric characteristics alone of the PV module used in this work. The quantities sought are useful for further efficiency analysis and for simulations. The first step in determining the characteristic of a solar module is a series of experiments aimed to measure these ones under certain precise, or *standard*, conditions. This section describes the experimental set-up and the procedure adopted. The results obtained are then analyzed and discussed.

3.1.1 Experimental set-up

The aim of the experiments needed for the characterization of a solar module is to first trace its $I - V$ characteristic. This specific chart contains many informations about the technical properties of the panel, its absolute performance and relative performance compared to other panels. In order to get this curve and make it comparable with other ones, a standardized procedure must be set-up. What mainly affects the performance of a solar panel are the overall irradiance, its spectrum, and the temperature of the cell. The most spread standard is **Standard Test Conditions** (STC). It is the one that all manufacturers use when declaring the data provided in the technical data-sheet of their products. It imposes a 1000 W/m^2 irradiance, a cell temperature of 25 ℃, zero wind and an *air mass spectrum* AM1.5. This index describes the sunlight spectrum and power of rays coming from an angle of 41,87° degrees above the horizon and hitting a plane tilted 37° from the ground. To test the panel which needs to be mounted on the distiller device in the previous conditions, the following list of materials had been used:

- Semi-flexible solar panel provided by XDISC®: 4 SunPower® 125 × 125 mm Mono-c Si cells connected in series with an innovative aesthetic camouflage coating from iLooxs™. The camouflage is intended to reduce the visual impact of the panel on the environment, thus enhancing the social acceptance of such installation. In this work, the camouflage reproduces a surface of water slightly rippled, in the case of an application into a floating device;

- Solar simulator;
- Ammeter;
- Voltmeter;
- 100 Ω variable load;
- Water cooled plate;
- Refrigerated circulator;
- Data acquisition hardware and software;
- 5 type K thermocouples;
- Pyranometer;

The experimental set-up was made positioning the cooling plate into the solar simulator. The plate was fed by the refrigerated circulator. Above the plate was placed the solar panel. In order to fill the gap between the panel and the plate, caused by the thickness of the thermocouples, and establish a good heat conduction, some wet towels were sandwiched between the two. Finally both panel and plate were clamped with vices, as shown in figure 3.1 to allow a good thermal contact between the PV panel and the cooling plate..

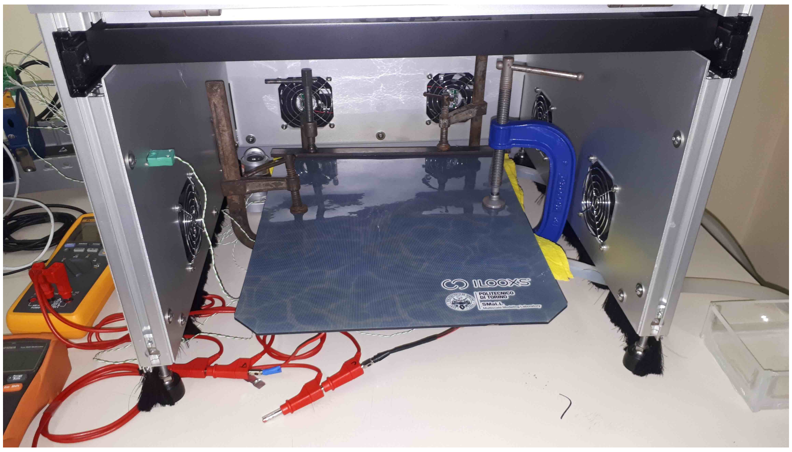

Figure 3.1: Positioning and clamping of the solar panel into the solar simulator

To check the temperatures of the cells required by the STC, four thermocouples (noted as 0, 1, 2 and 3), one for each cell, were mounted at the center of each cell (on the backside) as shown in figure 3.2. The fifth thermocouple (noted as 4) was placed in a corner in order to monitor the ambient temperature. To obtain the values of current and voltage that permit to trace the $I - V$ curve, the following schematic installation (figure 3.3a) was made and, by adjusting the load, the values displayed by the ammeter and voltmeter were noted manually. Thanks to this set-up, properties like open-circuit voltage, short-circuit current, maximum power point, filling factor, efficiency and temperature coefficients were obtained as explained in the next subsection.

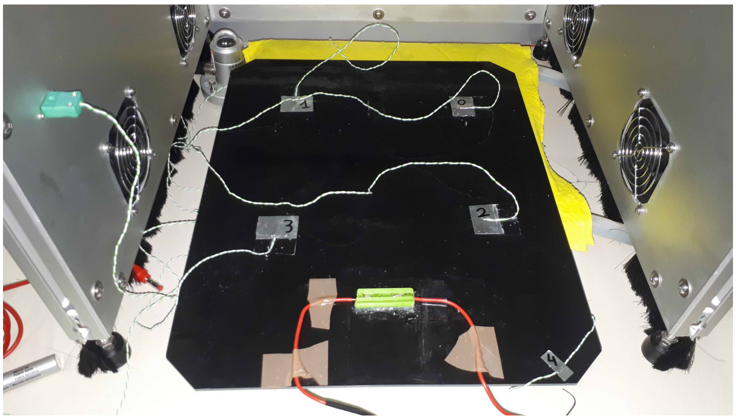

Figure 3.2: Positioning of thermocouples

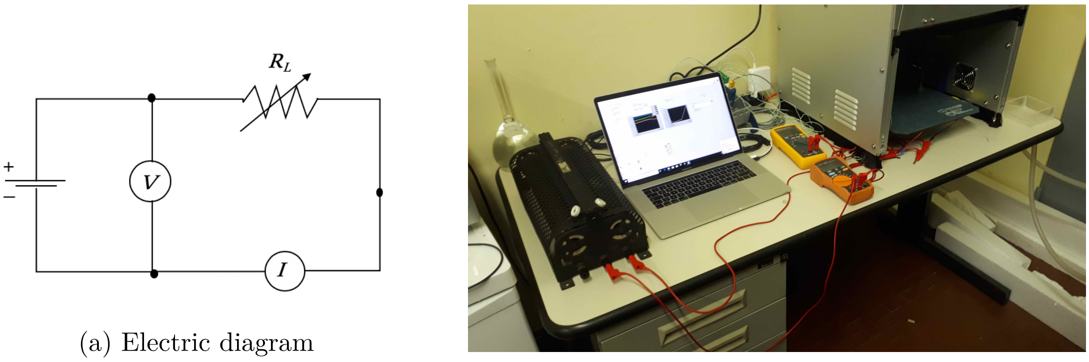

(a) Electric diagram

(b) Disposition of material

Figure 3.3: Experimental set-up

3.1.2 Test procedure and data analysis

In this subsection are explained the steps made to obtain the data sought and to guarantee the standard test conditions before mentioned. All the detailed results can be found in Appendix B. The first test consisted in setting the power of the lamp of the solar simulator, and checking the uniformity of its emission above the underlying surface. For this purpose, first a manual triggering of the power of the lamp was carried out, checking the irradiance measured in the middle of the test area. Then five measurements in different positions shown in figure 3.4 were performed during 10 seconds each. The results of each measurement by the pyranometer are listed in table B.1. The mean value of the five positions was **1009,6 ± 8,8 W/m^2**, so the aimed irradiance was attained with a quite uniform exposure.

The differences between points are negligible (±1%) and could depend not necessarily on the position but on the variability of power emitted by the lamp, which is not perfectly constant in time.

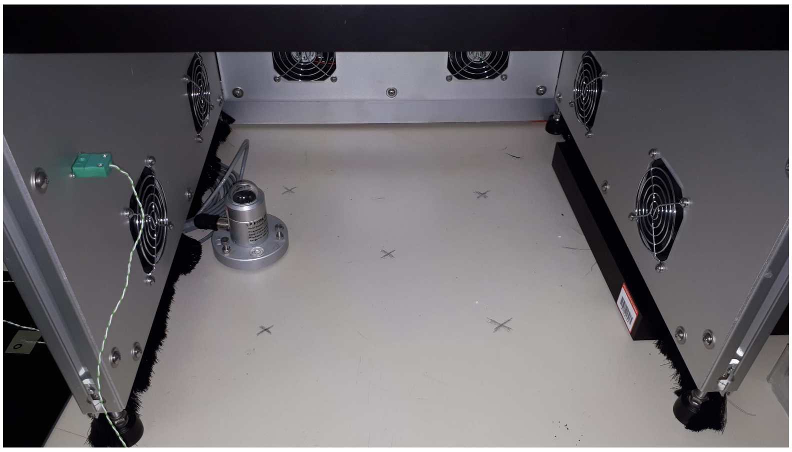

Figure 3.4: Measurement points employed for the irradiance uniformity test

The core of the experiments of the characterization consisted in reading the values displayed by the amperemeter and the voltmeter when varying the external load from a condition of short-circuit until open-circuit. During this operation, the temperatures of the cells were kept in a range between 23 °C and 27 °C by adjusting the temperature of the water circulating in the cooling plate, which was approximately at 9,6 °C. Once all the values were measured, including I_{sc} and V_{oc}, the maximum power point was identified by calculating for each couple of $I-V$ values their product, obtaining the power, hence finding the greatest value P_{mpp} and its corresponding I_{mpp} and V_{mpp}. Then, by applying equations 2.4 and 2.5, FF and η_{PV} were calculated respectively. This procedure was repeated three times for a greater repeatability of the experimental data.

Table 3.1: Results of STC tests n. 1, 2 and 3, and comparison with XDISC® Datasheet

	Test 1	Test 2	Test 3	Average	XDISC® Datasheet
$\boldsymbol{V_{oc}}$ **[V]**	2,654	2,653	2,656	$2{,}654 \pm 0{,}002$	2,72
$\boldsymbol{I_{sc}}$ **[A]**	3,21	3,146	3,178	$3{,}178 \pm 0{,}032$	4,72
$\boldsymbol{V_{mpp}}$ **[V]**	1,845	1,839	1,849	$1{,}844 \pm 0{,}005$	2,32
$\boldsymbol{I_{mpp}}$ **[A]**	2,930	2,880	2,911	$2{,}907 \pm 0{,}025$	4,44
$\boldsymbol{P_{mpp}}$ **[W]**	5,41	5,30	5,38	$5{,}36 \pm 0{,}06$	10,3
$\boldsymbol{FF}$ **[%]**	63,45	63,45	63,76	$63{,}55 \pm 0{,}18$	80,23
$\boldsymbol{\eta_{PV}}$ [%]	9,01	8,83	8,97	$8{,}93 \pm 0{,}1$	16,48

The results of the three tests under STC are resumed in table 3.1 and the charts are shown in figure 3.5. The recordings of the cells' temperature and the charts representing the MPP's of each test can be found in Appendix B. During the tests, cells's temperature were successfully kept in the prescribed range of 25 ± 2 °C as the average temperature of the cells was $24{,}8 \pm 0{,}5$ °C, hence the STC were respected. From the results, some observations

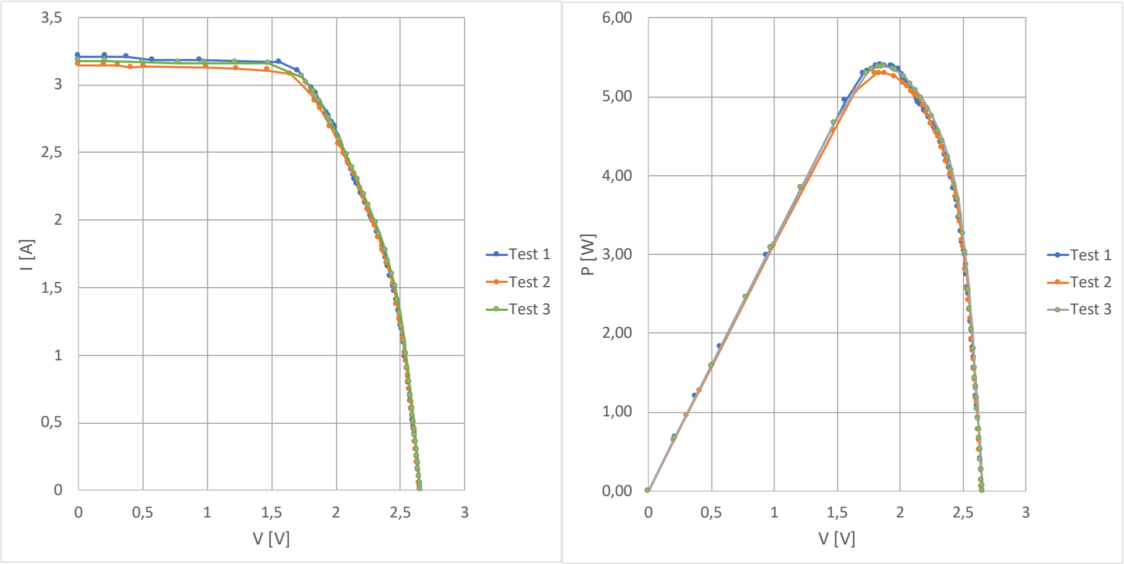

Figure 3.5: $I-V$ and $P-V$ charts obtained in tests n. 1, 2 and 3

need to be made:

- All the three tests show a good repeatability, with slight differences in the values and charts.
- V_{oc} of the module is around 4 times the nominal open-circuit voltage of the SunPower® cells (0,678 V), so it is the value predicted by equation 2.15. The value is also coherent with the original technical datasheet.
- I_{sc} of the module is around 49% less than the short-circuit current of a cell alone (5,75 A), and 43% less than what declared in the datasheet: this value is much lower than expected. Similarly to the previous observation, P_{mpp}, FF and η_{PV} have quite smaller values than expected. It is important to note how the surface camouflage influences the maximum power output: in table B.4, the manufacturer declares a P_{mpp} = 12,5 W for a 4 Mono-Si cells connected in series module, while the module employed here should have an output power of P_{mpp} = 10,3 W, thus proving that the coating reduces by 17,6% the maximum power, hence the efficiency.
- In figure B.1, in the first seconds of the tests when the working condition of the panel is in short-circuit or near, an anomalous increase in temperatures of the cells measured by T1 and T2 and a decrease of T0 and T3 is visible. This phenomenon reminds the mismatch in short-circuit currents mentioned in 2.2.2. The causes of this mismatch need to be determined. A possible explanation is the presence of a damaged cell.
- The difference of temperature during the rest of the test, for all the three trials, has always the same order. It shows that the panel was not sticking uniformly on the cooling plate, thus the left side, as seen from above, measured by thermocouples T1 and T3 was less strongly clamped and suffered from a greater heating.

An additional test was carried out in order to calculate just the temperature coefficient of the open-circuit voltage k_V, since the temperature coefficient of the short-circuit current k_I was difficult to obtain because of the unstable recording of the I_{sc}. The test consisted in rising step by step the temperature of the water circulating through the cooling plate, for each step waiting for the stabilization of the cells' temperature, then measuring the V_{oc} and the cells' temperature. Irradiance was kept constant at 1000 W/m^2. Eventually, considering a mean temperature of the four cells and applying equation 2.8, k_V was calculated for each step. The obtained value is between -0,005 V/°C and -0,006 V/°C, which is coherent with the predicted value corresponding to four times the value of k_V belonging to the SunPower® cell alone. The detailed results are listed in table B.3. However, the coefficients belonging to the module, as declared by the manufacturer, are listed in table B.5. The temperature coefficient for the power k_P is useful to foresee the actual performance of the panel in any temperature condition, as requested in the next chapters.

In conclusion laboratory results were not as satisfactory as wished. By the way, for the purpose of this work, the performance of the panel is not fundamental since the true goal is the production of distilled water. The probable cause of the low performance of the panel is that the cells which overheat are damaged. With the results obtained, a general mathematical model will be developed in the next section.

3.2 Mathematical modeling and validation

The other part of the work necessary to complete the characterization of the solar module is represented by the full capability to simulate its behavior in any situation. Hence, a general mathematical model is sought. Thanks to the implemented model, it is possible to predict the performance of the module under real conditions when tested in the environment. On the other hand, the model also needs to reproduce realistically the phenomenon, thus it needs to be validated. In this section are presented the development of the model and its mathematical validation.

3.2.1 Models development

In this subsection, the most consistent effort is dedicated into the development of the general model able interpret the characterization results obtained in the previous section. In the end, also an empirical model useful for comparison is implemented. The general model is based on the one-diode model shown in subsection 2.1.2. This model needs three further quantities not available neither in the data-sheet of the panel, nor after the tests: the series resistance R_s and the shunt resistance R_{sh}. Therefore, to obtain the general model two major steps must be taken: extraction of the resistances, and implementation of the equations of one-diode model. For the extraction of the resistances, an iterative model will be used. [12] The model needs as input data the characteristic points of the $I-V$ curve obtained during the STC test (noted with the subscript "0") and, by increasing step by step the value of R_s until matching the maximum power point, it calculates the shunt resistance. The procedure begins with the initialization of the value of the shunt resistance:

$$R_{sh,min} = \frac{V_{mpp,0}}{I_{sc,0} - I_{mpp,0}} - \frac{V_{oc,0} - V_{mpp,0}}{I_{mpp,0}} \tag{3.1}$$

and by calculating the reverse saturation current in STC:

$$I_{0,0} = \frac{I_{sc,0}}{exp\left(\frac{qV_{oc,0}}{N_s n k_B T_0}\right) - 1} \tag{3.2}$$

From now on, the magnitude $B(T) = \frac{q}{N_s n k_B T}$ will be employed to simplify the expressions. The iterative process is initialized with $R_s = 0$ and $R_{sh} = R_{sh,min}$ and begins with calculating the light generated current:

$$I_{L,0} = \frac{R_{sh} + R_s}{R_{sh}} I_{sc,0} \tag{3.3}$$

The shunt resistance is then recalculated as:

$$R_{sh} = \frac{V_{mpp,0}\left(V_{mpp,0} + I_{mpp,0}R_s\right)}{V_{mpp,0}I_{L,0} - V_{mpp,0}I_{0,0}exp\left[B(T_0)\left(V_{mpp,0} + I_{mpp,0}R_s\right)\right] + V_{mpp,0}I_{0,0} - P_{mpp,0,e}} \tag{3.4}$$

where $P_{mpp,0,e} = V_{mpp,0}I_{mpp,0}$ is the maximum power experimentally measured. Then, the one-diode model equation 2.7 is solved along the whole range of V from 0 to $V_{oc,0}$. The MPP resulting from the model is identified with $P_{mpp,0,m}$ and the error $err = |P_{mpp,0,m} - P_{mpp,0,e}|$ is calculated. If $err > err_{max}$, R_s is increased and the iteration restarts at equation 3.3.

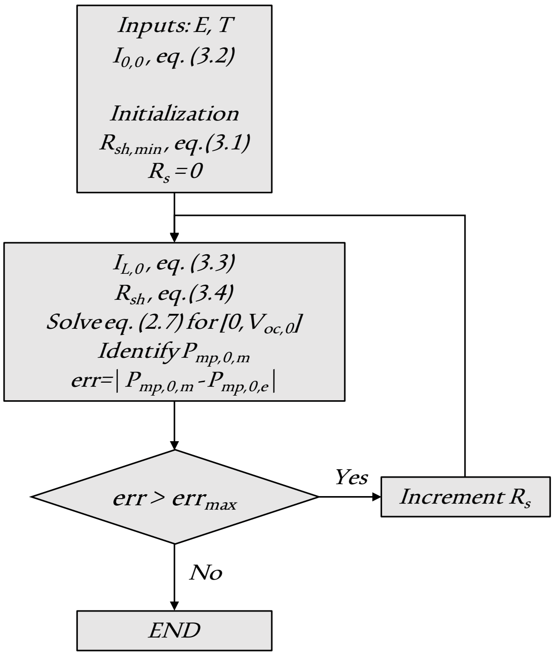

Figure 3.6: Flow-chart of the algorithm of extraction of the resistances

For the implementation of the model, a Matlab code has been developed. The maximum error has been chosen as $err_{max} = 0{,}1$ and the increase value for R_s during each iteration has been chosen as 0,001 in order to ensure a good level of precision. Thanks to this model, the resistances found are $\boldsymbol{R_s = 0{,}13\ \Omega}$ and $\boldsymbol{R_{sh} = 10{,}07\ \Omega}$. Starting from this point, different external conditions of temperature T and irradiance E can be simulated by implementing another model presented in the following lines. It calculates the light generated current and the reverse saturation current affected by temperature and irradiance as follows:

$$I_L = \frac{E}{E_0}\left[I_{L,0} + k_I\left(T - T_0\right)\right] \tag{3.5}$$

$$I_0 = \frac{I_{sc,0}}{exp\left(B(T)V_{oc,0}\right) - 1} \cdot \left(\frac{T}{T_0}\right)^3 \cdot exp\left[\frac{E_g}{nk_B}\left(\frac{1}{T_0} - \frac{1}{T}\right)\right] \tag{3.6}$$

where $E_g = 1{,}12$ eV $= 1{,}7942 \cdot 10^{-19}$ J is the energetic band gap of the cristalline Si semiconductor at 25 ℃. With these two quantities it is now possible to solve equation 2.7 with a code which requires to solve it until $I \geq 0$, since V_{oc} is unknown.

The other model implemented to obtain the expression of I, known the characteristic points of the $I - V$ curve obtained after a test, is an empirical model without physical meaning but able to reproduce the obtained results. Its equations are [29]:

$$I = I_{sc}\left\{1 - C_1\left[\exp\left(\frac{V}{C_2V_{oc}}\right) - 1\right]\right\} \tag{3.7}$$

where

$$C_2 = \frac{\frac{V_{mpp}}{V_{oc}} - 1}{ln\left(1 - \frac{I_{mpp}}{I_{sc}}\right)} \tag{3.8}$$

$$C_1 = \left(1 - \frac{I_{mpp}}{I_{sc}}\right) \cdot \exp\left(-\frac{V_{mpp}}{C_2V_{oc}}\right) \tag{3.9}$$

The first model is useful because of its capability to simulate the panel behavior, since it fully characterizes it. The second is used when comparing and validating the models to the experimental data.

3.2.2 Validation by experimental data

A comparison between different models and experimental evidence of PV performance is achieved in this subsection. In figure 3.7, $I-V$ and $P-V$ charts resulting from the iterative model, the empirical model and the STC test n. 3 are represented together. The iterative and the empirical model have been fitted on the average values of the three tests. Test n. 3 has been chosen for the comparison because it was pursued by measuring the most evenly spaced points on the $I - V$ chart: a good spacing is necessary for the goodness of fit analysis made later. By observing graphically the figure some comments can be made:

- The empirical model is visibly more similar to the experimental points than the iterative model.
- The differences between iterative model and experimental data, as long as they match in the MPP for definition, which are visible in the $I - V$ chart, occur in the sections

between short-circuit and MPP, and between MPP and open-circuit. The slope in the first section is related to the small value of the shunt resistance R_{sh}. [9] Indeed, the value calculated in subsection 3.2.1 is quite low, as typically it is in the order of hundreds of Ω. The slope in the other section is caused by increasing values of the series resistance R_s. The calculated value in this case is realistic but probably slightly high. R_s has a value comparable to the one declared in table B.4, while R_{sh} is far from being correct.

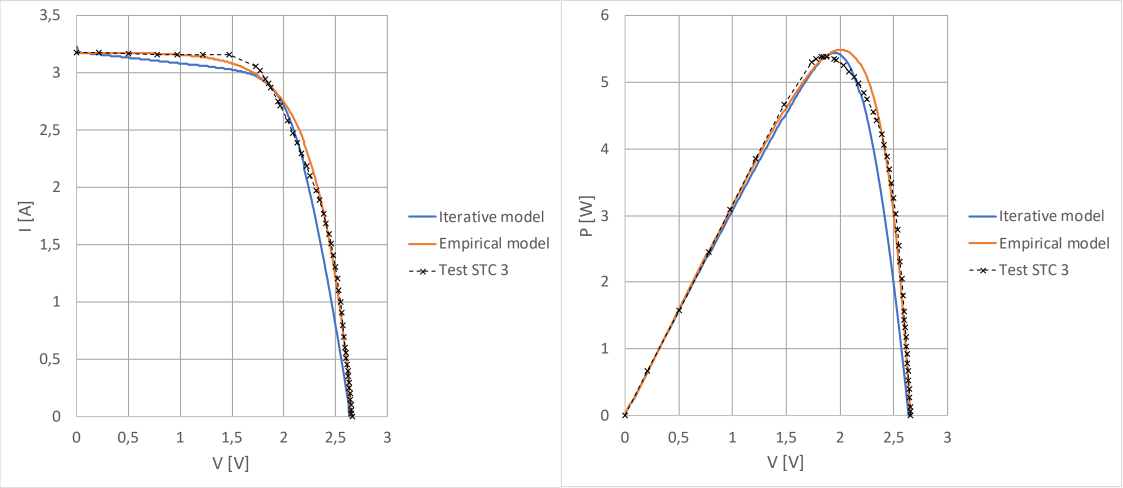

Figure 3.7: $I - V$ and $P - V$ charts obtained with iterative and empirical models, and in test n. 3. Test n. 3 was chosen because it had the better equally spaced points.

Table 3.2: Comparison of characteristics obtained by test n.3, mean value of tests n. 1, 2 and 3, iterative model and empirical model. Iterative and empirical model are based on the average values of tests 1, 2 and 3.

	Test 3	Average	Iterative mod.	Empirical mod.
$\boldsymbol{V_{oc}}$ [V]	2,656	2,654	2,638	2,654
$\boldsymbol{I_{sc}}$ [A]	3,18	3,18	3,22	3,18
$\boldsymbol{V_{mpp}}$ [V]	1,849	1,844	1,950	1,844
$\boldsymbol{I_{mpp}}$ [A]	2,91	2,91	2,79	2,91
$\boldsymbol{P_{mpp}}$ [W]	5,38	5,36	5,44	5,36
$\boldsymbol{FF}$ [%]	63,76	63,55	64,52	63,56
$\boldsymbol{\eta_{PV}}$ [%]	8,97	8,93	9,02	8,93

By analyzing the values in table 3.2, note that the empirical model and the average values match completely. The reason is that the empirical model curve is fitted precisely on V_{oc}, I_{sc}, V_{mpp} and I_{mpp}. Inversely, the iterative model uses all these values only for the calculations of the two resistances, then it solves, for $V = 0 \div V_{oc}$, equation 2.7. Because of the remaining error, the new calculated values differ from the average values they come from. To evaluate the differences between model and experimental results, it has been employed the *Root Mean Square Error* ($RMSE$) method. [30] It permits to compare and validate the data obtained by a mathematical model to its original experimental data from which is based on. It is defined as:

$$RMSE = \sqrt{\frac{\sum_{i=1}^{N} (O_i - P_i)^2}{N}} \tag{3.10}$$

where O_i are the observed experimental data, P_i are the values predicted by the model and $N = 42$ is the number of values measured during test 3. For each value of V measured during test 3, the corresponding I values obtained with the iterative and empirical models are considered and compared to the experimental ones. For having a better understanding of the difference, the $RMSE$, which has the same physical unit as the quantity it is evaluating, has been normalized in order to obtain a percentage magnitude. The *Normalized Root Mean Square Error* is formulated as:

$$NRMSE = \frac{RMSE}{O_{max} - O_{min}} \tag{3.11}$$

Both $I - V$ and $P - V$ characteristics have been evaluated for the iterative and empirical models with the ones belonging to test 3. The results are listed in table 3.3. These results confirm the better fitting achieved by the empirical model compared to the iterative one.

Table 3.3: $RMSE$ and $NMRSE$ of $I - V$ and $P - V$ characteristics of iterative and empirical model compared to test n. 3

	RMSE	**NMRSE**
Iterative Model		
$I - V$	0,284 A	8,94%
$P - V$	0,706 W	13,13%
Empirical Model		
$I - V$	0,081 A	2,54%
$P - V$	0,185 W	3,44%

The error of the latter is not negligible (8,94 % for the current and 13,13% for the power), but it is due to the way how it is evaluated. The evaluation is made upon the vertical direction, so in the range between MPP and V_{oc} the differences are high. However, if the evaluation was made comparing the absolute distance between the two curves, as it was made when they were compared just graphically, the error would not be that dramatic. Furthermore, the empirical model only works if provided, for each condition of irradiance and temperature, with the data obtained after the test in these particular conditions (i.e. V_{oc}, I_{sc}, V_{mpp} and I_{mpp}). The predictive capabilities of the iterative model will be demonstrated when the solar panel will be exposed to real outdoor conditions. Still, an anticipation of the way it works is shown in the next subsection.

3.2.3 Sensitivity analysis by the iterative model

This subsection is dedicated to testing the one-diode model developed with the iterative algorithm. The aim is to observe the sensitivity of the results when subjected to different conditions. This model has been developed in order to foresee the behavior of the panel under unknown conditions. In this part, the nominal $I-V$ and $P-V$ characteristic of the module were considered. In this case, the iterative model gives as output the following values for the resistances and the following graphs in figure 3.8: $\boldsymbol{R_s = 0\ \Omega}$ and $\boldsymbol{R_{sh} = 21{,}20\ \Omega}$.

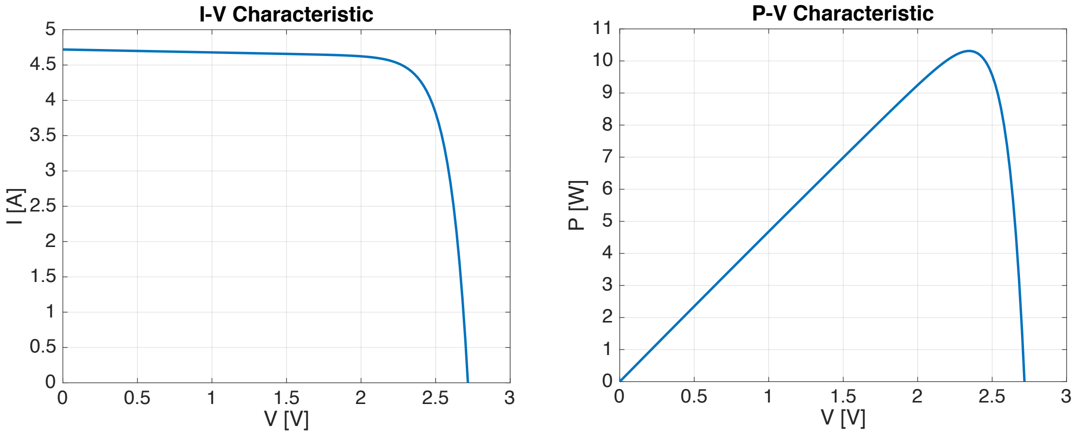

Figure 3.8: Nominal $I-V$ and $P-V$ charts obtained with the iterative model in STC conditions

The results obtained for the panel tested in this chapter and the ideal one are very different. Starting from comparing the charts in figures 3.5 and 3.8, their trends show different behaviors. The first has a smoother drop while the second shows a net drop after the MPP.

An example of the results obtained in different irradiance and temperature conditions is shown in figure 3.9. The temperatures coefficients used are the ones provided by the manufacturer in table B.5. As it can be seen in the $I-V$ chart in figure 3.9.a, the effect of the irradiance seems linear on the short-circuit current, while for the open-circuit voltage, the effect is more evident for decreasing values of E. The same trend is visible for the $P-V$ chart. The temperature on its side has very little influence on the short-circuit current, but a visible and linear negative effect on the open-circuit voltage. Both charts in figure 3.9.b demonstrate the reason why solar panels should be cooled down in order to be more powerful.

An additional analysis carried out concerns the variation of the efficiency under the effect of the external conditions. To do so, in figure 3.10 is plotted the maximum efficiency $\eta_{PV,MAX}$, which is always obtained in the Maximum Power Point, for a temperature range between 25 and 75 °C, and an irradiance range between 200 and 1000 $\mathrm{W/m^2}$. It is noticeable that a rise in temperature affects a strong linear fall of the efficiency. Irradiance on the other hand has a less strong impact on the efficiency, with a trend which seems greater at low irradiance and which decreases weakly at high irradiance.

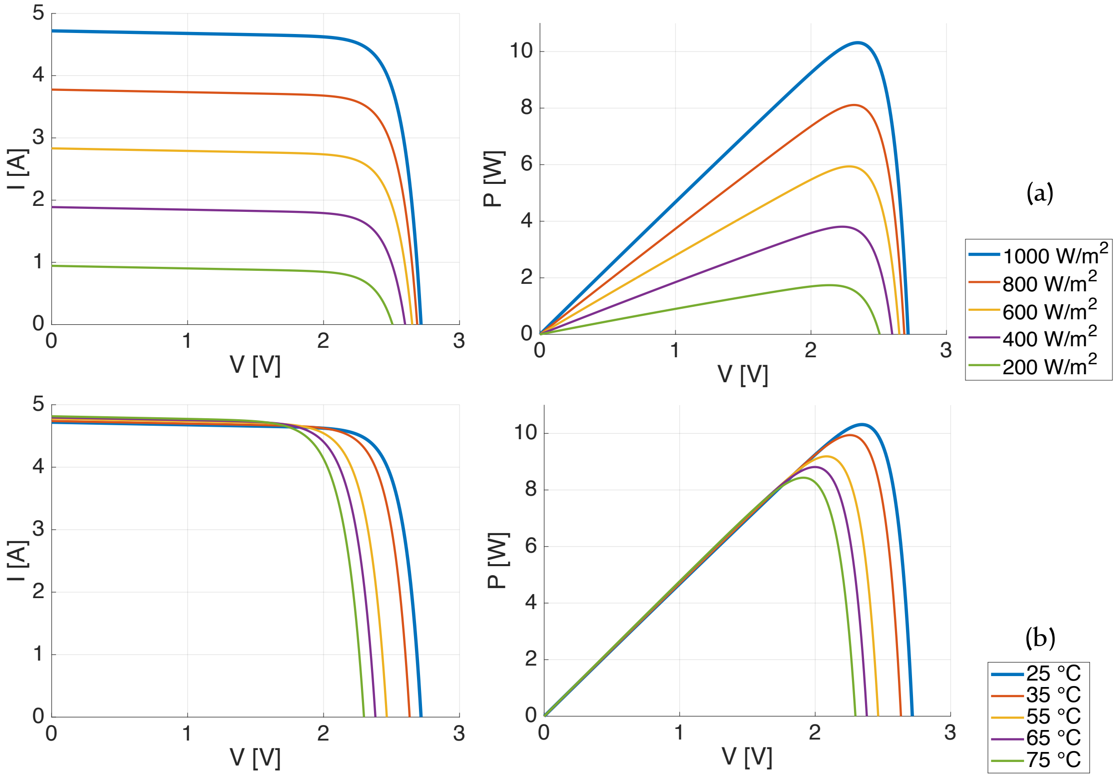

Figure 3.9: Simulation of the irradiance effect at $T = T_0 = 25$ °C (a) and temperature effect at $E = E_0 = 1000$ W/m^2 (b) on the characteristic curves of the module.

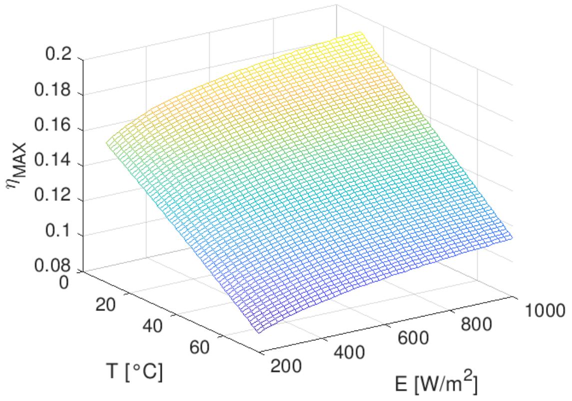

Figure 3.10: Maximum efficiency chart depending on irradiance and temperature

To better identify where the best and less spending optimization could be pursued in order to get an increase in efficiency, the gradient of the efficiency chart has been

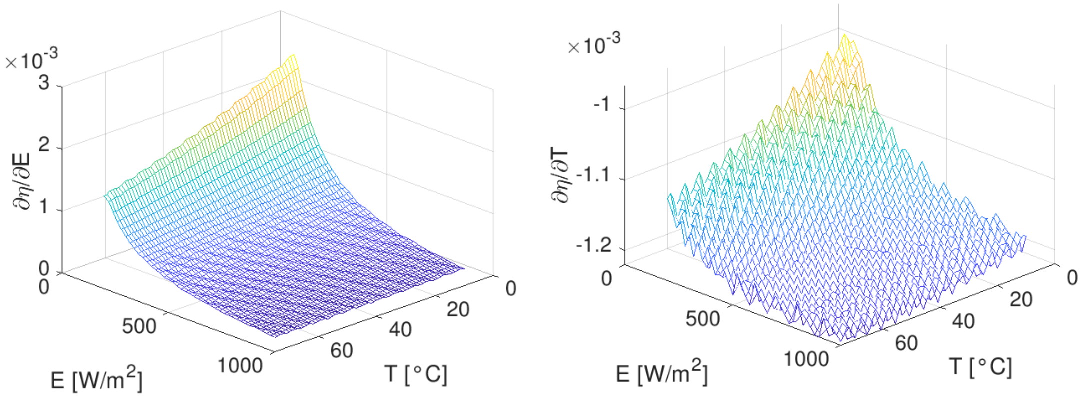

Figure 3.11: Components of the gradient vector of the efficiency depending on irradiance and temperature

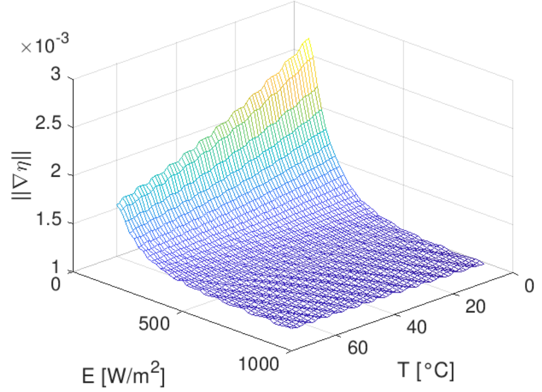

Figure 3.12: Norm of the gradient vector of the efficiency depending on irradiance and temperature

calculated, and the value of its two components and of its norm were plotted depending on temperature and irradiance, as shown in figures 3.11 and 3.12. The partial derivative along T is negative, as long as the efficiency decreases when the temperature rises. $\partial\eta_{PV}/\partial E$ is positive in accordance with the efficiency chart. A major rise in efficiency could be easily obtained by not going below 400 $\mathrm{W/m^2}$ and by cooling the panel as much as possible. Note that for increasing values of E and independently from T, $\partial\eta/\partial E$ tends to 0, meaning that the efficiency gain for increasing values of irradiance tends to be null. On the other hand, $\partial\eta/\partial T$ is always < 0, so for whatever value of E, a decrease of T produces a positive efficiency gain. Consequently, to generate energy efficiently with the module, is not needed an extremely sunny day but always a good cooling of the panel. For this same reason in the next chapter it will be shown how the distiller manages to cool the cells, thus allowing a virtuous synergic effect between both systems.

3.3 Outdoor experiments

Since the module tested in section 3.1 has been determined to be damaged, a new one was bought and hereby tested. In collaboration with the electric division of the Department of Energy, the new module was tested outdoor during a clear day to determine its characteristics under true sunlight. In this section are described briefly the experimental set-up, the procedure followed to get the magnitudes in STC and other conditions, and eventually are presented and discussed the results.

3.3.1 Experimental set-up

Similarly to section 3.1, the experimental set-up has been designed to guarantee STC testing conditions first and then also different testing conditions at controlled temperature. Since sunlight was used, irradiance could not be controlled. However, experiments have been done from 12 a.m. until 2 p.m., which allowed to provide high and quite stable values of solar irradiance. The material employed was the following:

- Semi-flexible solar panel provided by XDISC®: 4 SunPower® 125 × 125 mm Mono-c Si cells connected in series with aesthetic camouflage coating from iLooxs™ with the same technical characteristics of the previous panel and similar, rippled water alike camouflage;
- PV testing equipment;
- Water cooled plate;
- Refrigerated circulator;
- Data acquisition hardware and software;
- 5 type K thermocouples;
- Pyranometer;
- Tilted structure;

The set-up was made positioning the cooling plate fed by the refrigerated circulator on the tilted structure. The pyranometer was mounted too on the structure, in order to measure the correct irradiance. The panel has been clamped to the cooling plate with transparent tape and the gap between panel and plate compensated with a wet towel. Temperatures have been recorded on the four cells like during the indoor experiments, keeping the same nomenclature and order of the cells (0, 1, 2 and 3). A professional PV testing equipment was employed to get the $I-V$ and $P-V$ characteristics.

3.3.2 Test procedure and data analysis

The goal was to obtain the $I-V$ and $P-V$ curves in STC conditions and also in conditions of similar irradiance but different, controlled temperature. By measuring the open-circuit voltages, short-circuit currents and MPP voltages and currents each time,

Figure 3.13: Outdoor experimental set-up: 45°03’52"N 7°39’41"E global coordinates of the test.

it was eventually possible to calculate the temperature coefficient of power of the panel. Detailed results are listed in Appendix B. A common procedure was followed during each temperature step. Once the panel reached a stable temperature, a series of 3 repeated measurements was made with the PV testing equipment. Since the experimental set-up makes the measurement instantly, only the instant temperatures and irradiance were recorded. Steps of +10 ℃ each, starting from 25 ℃ (STC), were chosen until reaching around 65℃. The tests started when the solar irradiance managed to reach around 1000 W/m^2.

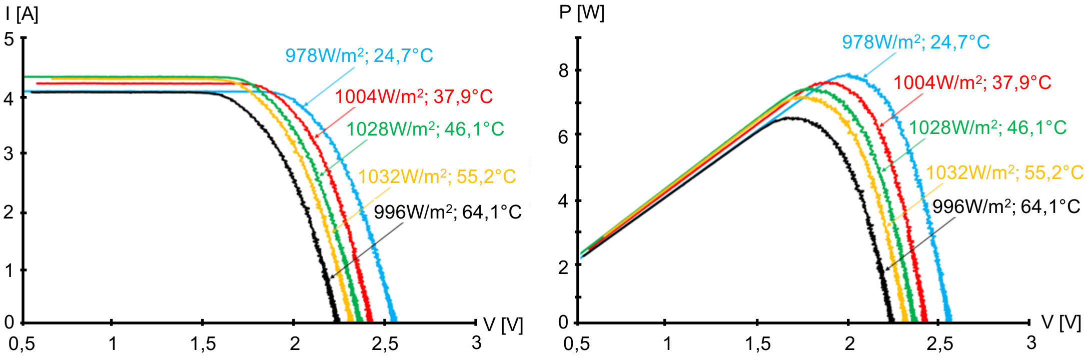

Figure 3.14: $I-V$ and $P-V$ charts for different temperatures of the cells

Figure 3.14 depicts the $I-V$ and $P-V$ characteristics obtained during the various tests under different temperature conditions. In the figure are also noted the values of irradiance at which the curves have been measured. It does not go unnoticed the similarity of trends between the real case and the simulations studied in the previous section, see figure 3.9. The data obtained here need a further manipulation in order to become suitable to determine the general characteristics. In fact, the curves have been measured under also slightly different irradiances, which means that they are not immediatly comparable for the calculation of the temperature coefficients and also to determine the precise STC values. So, the short-circuit currents have been scaled proportionally to the irradiances because of the direct relation between current and irradiance in accordance with equation 2.9, and voltages on a logarithmic ratio depending on irradiance according to equation 2.3. The corrected results are listed in table 3.4. These results show a more similar behavior to what declared by the manufacturer in table B.5. P_{mmp}, so the efficiency, in STC are 32% lower than what expected. The aesthetic camouflage could cause this loss in efficiency as it reduces a fraction of sunlight hitting the cells. With these results, the temperature coefficients calculated are listed in table 3.5.

Table 3.4: Corrected results of the outdoor characterization of the PV module

T [°C]	STC	37,9	46,1	55,2	64,1
$\boldsymbol{V_{oc}}$ **[V]**	2,56	2,45	2,38	2,30	2,23
$\boldsymbol{I_{sc}}$ **[A]**	4,11	4,15	4,17	4,2 0	4,22
$\boldsymbol{V_{mpp}}$ **[V]**	1,997	1,85	1,77	1,68	1,59
$\boldsymbol{I_{mpp}}$ **[A]**	3,98	4,04	4,06	4,08	4,10
$\boldsymbol{P_{mpp}}$ **[W]**	7,95	7,47	7,19	6,85	6,52
$\boldsymbol{FF}$ **[%]**	75,54	73,51	72,41	70,96	69,27
$\boldsymbol{\eta_{PV}}$ **[%]**	12,72	11,96	11,50	10,97	10,43

Table 3.5: Calculated temperature coefficients of the PV module

$\boldsymbol{k_V}$ **[V/°C]**	-0,0084
$\boldsymbol{k_I}$ **[A/°C]**	0,0028
$\boldsymbol{k_P}$ **[W/°C]**	-0,0361

These values are very similar to the nominal ones, thus it can be stated that there is coherence between the experimental results and the data sheet. With the true temperature coefficient of power k_P it is possible to estimate closely an efficiency gain achievable by reducing the cells' temperature with the passive distillers, as shown in the next chapters.

3.3.3 Application of mathematical modeling to experimental data

To predict the several combinations of working points at which the module could possibly operate, in this subsection are calculated the series and shunt resistances of the module previously tested.

Figure 3.15 depicts the output of the iterative model applied to the experimental data. The resistances calculated are $\boldsymbol{R_s = 0{,}032\ \Omega}$ and $\boldsymbol{R_{sh} = 200{,}5\ \Omega}$, which provide more realistic values with respect to the ones obtained in subsection 3.2.3. Thanks to these values, it is now possible to fit the model to the experimental results. In table 3.6 are listed the results of the simulations fitted on the experiments, e.g. 1000 W/m^2 and steps of +10 °C from STC until 65 °C. The differences between the following table and table 3.4 are small and affect the calculation of the MPP, mostly the V_{mpp} coordinate. Globally,

V_{mpp} is 8% higher and I_{mpp} 4% lower, thus the P_{mpp} and η_{PV} differ by around +3%. It can be stated that, for real systems, the iterative model is able to estimate with a good reliability the internal resistances of the module necessary to implement the one-diode model.

The one-diode model allows to predict the operation point of the module in different external conditions: the weather which affects solar irradiance and cell's temperature, and the type of load applied which affects the coordinate on the $I-V$ and $P-V$ curves. In realistic applications is installed a *Maximum Power Point Tracker* (MPPT). It is a device that implements an algorithm to regulate the load applied to the module, by acting on the voltage at the output pins on the PV, in order to track the MPP and guarantee always the most efficient exploitation of the module. For this reason, the other combinations of coordinates on the characteristic curves are never used.

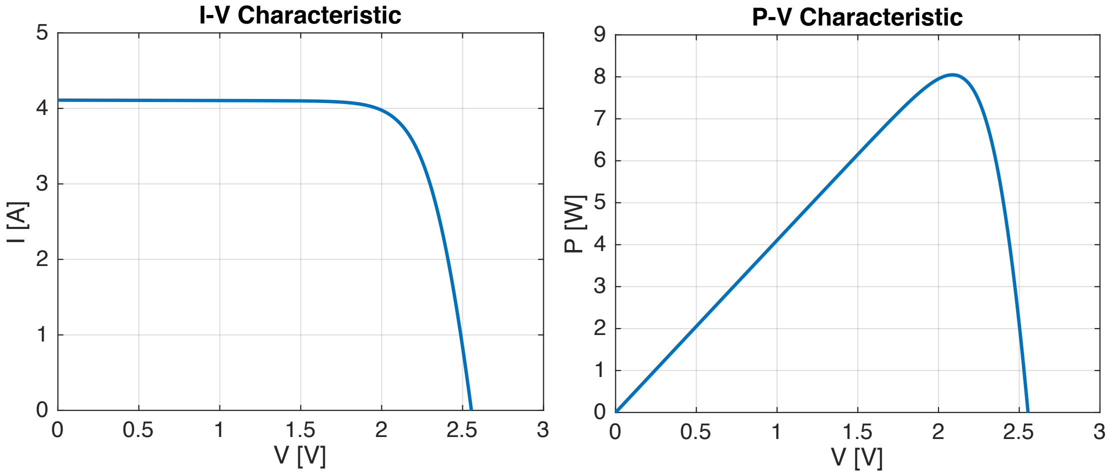

Figure 3.15: $I-V$ and $P-V$ charts of the undamaged panel obtained with the iterative model in STC conditions: Fitting on experimental results.

Table 3.6: Simulated results of the outdoor characterization of the PV module

T[°C]	STC	35	45	55	65
$\boldsymbol{V_{oc}}$ **[V]**	2,56	2,48	2,4	2,31	2,23
$\boldsymbol{I_{sc}}$ **[A]**	4,11	4,14	4,17	4,19	4,22
$\boldsymbol{V_{mpp}}$ **[V]**	2,09	2	1,92	1,83	1,75
$\boldsymbol{I_{mpp}}$ **[A]**	3,85	3,87	3,87	3,89	3,89
$\boldsymbol{P_{mpp}}$ **[W]**	8,05	7,74	7,43	7,12	6,79
$\boldsymbol{FF}$ **[%]**	76,48	75,39	74,24	73,55	72,15
$\boldsymbol{\eta_{PV}}$ **[%]**	12,72	12,38	11,89	11,39	10,86

Chapter 4

Characterization of the passive solar distiller

This chapter constitutes a broad study of the passive solar distiller, whose design is inspired by the work of [6] presented in section 2.4. Before addressing the study, it is first briefly introduced the design of the distiller used in this work and explained the reasons of such choices. The distiller is composed of:

- 3 hydrophilic cloths, 125 mm × 180 mm (length × width) for the evaporators;
- 3 hydrophilic cloths, 180 mm × 25 mm (length × width) for the condensers;
- 3 microporous PTFE membranes (pore size 0,1µm), size 125 mm × 40 mm;
- 4 aluminium 125 mm × 35 mm plates;
- Customized, 141 mm × 30 mm aluminium heat sink;

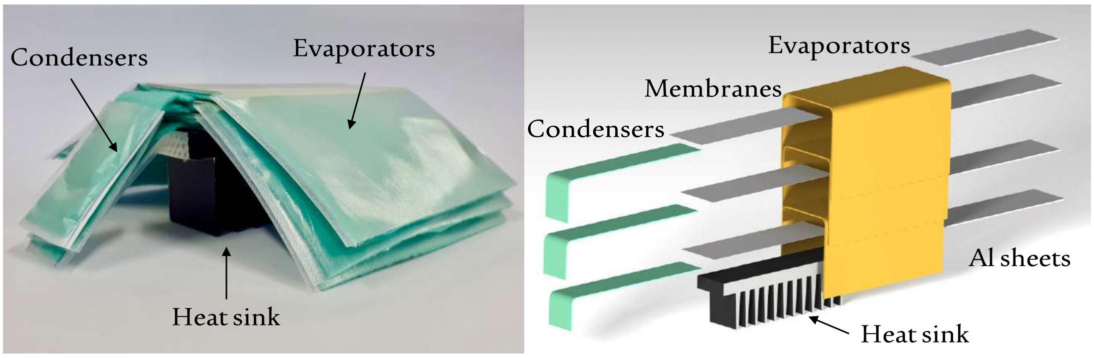

Figure 4.1: Prototype of a distiller and rendered exploded view

The assembly is made in accordance with what described in section 2.4. The choice of this particular shape is conceived to optimize the autonomous salt diffusion during night-time. In this configuration and as shown in figure 4.1, the saltwater feed is provided from the two long sides while the distillate collection occurs only from one short side. Since salt diffusion is slow, the shape is designed to help the exceeding salt accumulated during a day to diffuse back to the saltwater. Indeed, the salt diffuses along a shorter distance (in the width direction, i.e. 35/2 mm), and through a bigger cross section (125 mm on the two sides). In figure 4.1 are also shown the layers forming the stages. For this work it has been chosen to implement three stages with microporous membranes, although more (up to 10) could provide better performances [6], to reduce the complexity. In fact, in Chapter 5 is presented the entire prototype which incorporates eight distilling modules and is covered by a PV panel. So, because it is the first prototype of its kind, a first trial with only three stages allows to simplify the design process and assembly operation.

In this chapter a broad characterization of the distiller is done via different experiments to measure performance and thermal properties. Numerical 1D and 3D modeling is implemented for simulations which allow to estimate further quantities for the energetic analysis. All the detailed results are presented in Appendix C.

4.1 Experimental activity

The distiller presented in this work needs a preliminary full characterization as it is a unique piece, built and never tested in this precise configuration before. The data obtained after this task is important to foresee the performance of the overall prototype which mounts eight identical distiller modules. In order to get these informations, a campaign of several repeated tests has been pursued so that repeatability was guaranteed. In this section are shown the elements forming the experimental set-up, the procedures of the different tests and finally the data analysis of results.

4.1.1 Experimental set-up for the evaluation of the distillation performance

The core of this experimental campaign is testing the distillation performance of the device heated by the back side of the PV module. The conditions to test the distiller try to replicate as much as possible real conditions of application, i.e. desalination of seawater with heat provided by the sun. The data sought is first of all the specific mass flow rate J expressed in [l/m^{2}h] under reference conditions. Here, the solar input power is equal to $E = 1000$ W/m^2, also called *one sun*. Another reference condition concerns the salinity of the saltwater, which is chosen equal to 35 g/l of sodium chloride NaCl, value representing the mean salinity of the oceans. The last condition imposes that the temperature of the saltwater, which cools the heat sink of the distiller, is at 20 °C, being a reasonable value of the mean temperature of the seas during the year. The list of materials employed for the experiments is the following:

- Distiller, as presented above;
- PV panel;
- Solar simulator;

- Refrigerated circulator;
- Recordable balance;
- Data acquisition hardware and software;
- 5 type K thermocouples;
- Pyranometer;
- Containers for saltwater and distilled water;
- Refractometer to measure salinity.

The experimental set-up is made positioning into the solar simulator the PV panel which is above the distiller. The distiller is positioned so that the fins of the heat sink and the evaporator cloths are dipped in the saltwater. The layers of the condenser cloths are dipped in the freshwater inside the distillate container. The distillate container is positioned on the recordable balance, which records its weight continuously. To control the temperature of the water in the feed container, a cooling circuit connected to the refrigerated circulator is implemented.

Figure 4.2: Experimental set-up for testing the distiller

While the balance records the mass being distilled during the test, i.e. the volume V [ml], the five thermocouples measure the temperatures of: the back side of the panel next to the contact area with the distiller, T_{cell}; the first aluminium plate in contact with the first evaporator cloth, T_{evap}; the last aluminium plate between the last condenser cloth and the heat sink, T_{cond}; the saltwater, T_w; the air above the panel, T_a. The recorded mass of the distillate basin allows to calculate the mass flow rate and specific mass flow rate of the distiller, while the temperatures are useful to know the temperature profile and to evaluate the convection and radiative losses of both the distiller and panel. Before and after the test, salinity of saltwater is checked to keep it under control, and salinity of distillate is checked to ensure that only distillate has been produced and no contamination of salt occurred. After each trial, salinity in different points on each evaporator and condenser cloth is measured. On the evaporators it is useful to evaluate the extent of salt accumulation. On the condensers, it is required to further ensure that no salt contamination occurred, and, in the negative case, also identify which stage caused it.

4.1.2 Procedure of the distillation performance test

The first preliminary test pursued was to set the power emitted by the lamp in order to provide the requested irradiance and to check the uniformity of the radiation. The power was iteratively adjusted triggering the knob and measuring the irradiance in different points on the irradiated area. Once an acceptable value was obtained, the irradiance was measured in nine different points as shown in figure 4.3, which are highlighted with the green tape. The mean value of the nine positions was 1002,5 ± 51,3 W/m^2 (see table C.1).

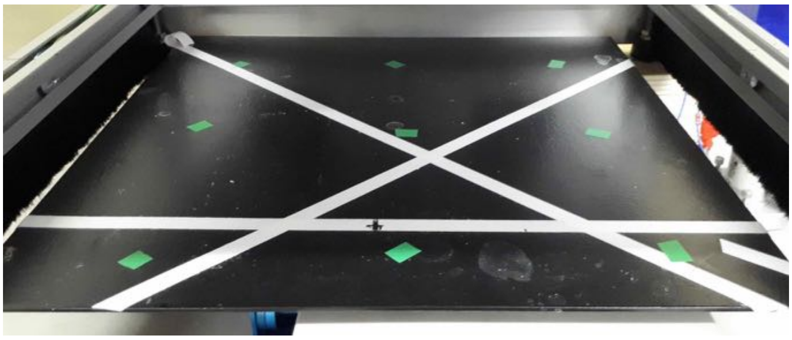

Figure 4.3: Measurement points of the heat flux test

Once the irradiance was set, the following operations have been carried out before every test:

- Setting of the desired level of the feed water inside the container in order to cool properly the heat sink and provide enough feed water to the dipped evaporator cloths;;
- Setting of the salinity of the saltwater at 35 g/l;
- Mounting of the different layers and thermocouples of the distiller;
- Positioning of the distiller, and laying the panel on top of it;
- Positioning of the distillate container on the balance;
- Filling with freshwater of part of the distillate container, so that the condenser cloths have their extremities dipped in it;
- Activation of the refrigeration circuit;
- Final check to ensure that all thermocouples were in the correct place after the operation of positioning; to ensure that no surrounding objects or the condenser layers

themselves touch the borders of the distillate container, thus interfering with the mass recording; and to ensure that the mounting is made correctly (correct alignment of the layers).

The operation of mounting the distiller required to previously wet the condenser layers with freshwater: to do so, 5 to 6 ml of freshwater were poured on each stage. After that, each layer forming a stage, i.e. one condenser, one membrane and one evaporator, were mounted in the correct order. During the positioning of the distiller in the designated place, the evaporators started absorbing the saltwater until all the surface became wet. After these operations and before launching the test, it was necessary to wait around 30 to 40 minutes in order to ensure the stability of the value of the mass displayed, which varied because of transient phenomena of absorption and release of water by the microfiber. Then the test was started: the solar simulator was switched on as well as the recording of mass and temperatures. After 5 hours, the light, the recorder and the refrigeration circuit were switched off and the following operations were carried out:

- Removal of the panel from above the distiller, of the distiller from above the saltwater basin and of the distillate container from above the balance;
- Disassembly of the distiller;
- Measurement of the salinities of the distillate and saltwater basins, and in the condenser and evaporator layers;
- Rinsing of all the components with freshwater.

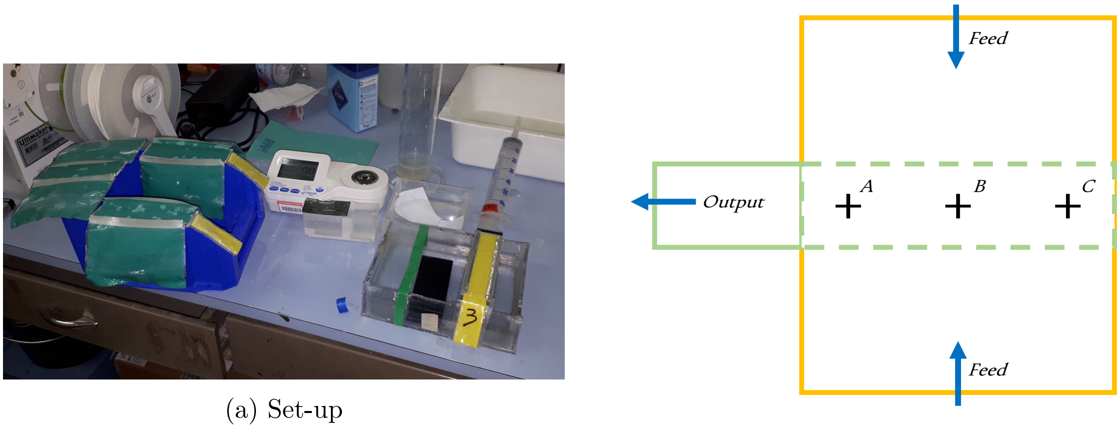

(a) Set-up

(b) Scheme of the sampling points on the cloths

Figure 4.4: Salinity measurement

To measure the salinity concentrations in the cloths three points were considered as sampling points, designated with A, B and C as shown in figure 4.4b on each condenser and on each evaporator. The values obtained were noted manually.

4.1.3 Results and data analysis of the performance test

In this subsection only the tests considered as successfully pursued are shown. By the way, the next subsection is also dedicated to the initial failures and their causes. Out of fourteen tests, only six showed the expected behavior. In the following lines, these are called depending on the dates when they have been carried out. 14/01, 16/01, 17/01 and 21/01 were done using a correctly built distiller after many unsuccseful trials. After this first campaign aiming at determining a robust assembly of the distiller, seven other identical distillers have been built for the prototype, so it was necessary to check that the design was effective in test 28/01. Test 31/01, in which the thermocouples had been placed differently, was done because of missing data demanded by thermal simulations. Also the procedure of test 31/01 was different, as the refrigerated circulator was only turned on after 6000 s. The tests were considered successful because they managed to reach a steady state, a good output and only distilled water was produced as well as no contamination of saltwater affected any condenser cloth. In figure 4.5 are shown the plots obtained with the recordable balance along the total duration of the experiments.

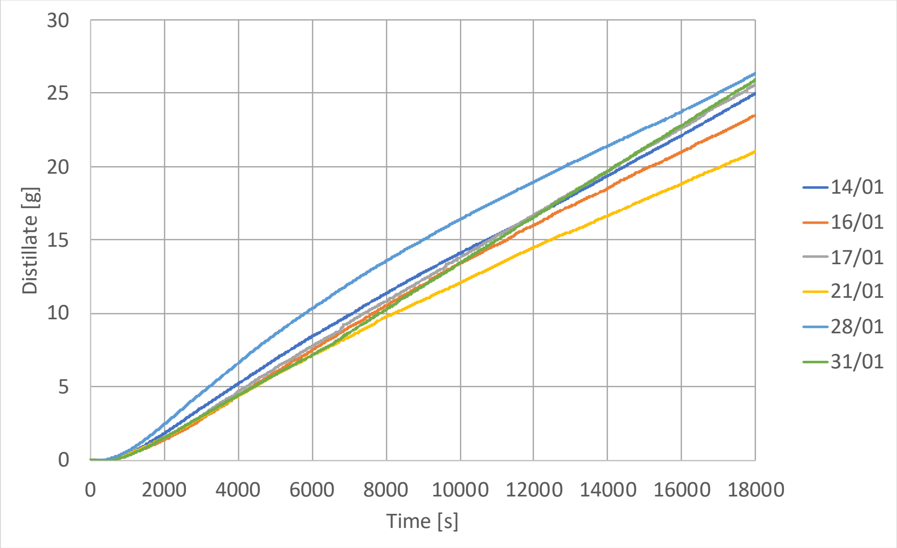

Figure 4.5: Overall distillate produced

All the plots show a common evolution at the beginning, with a little decrease followed by the change of trend around 250 and 300 s. At this moment, the gradient of temperature is enough to establish a flow rate that can overcome the losses of mass due to the evaporation of the water in the basin. From figure 4.5, the most successful test is 28/01; 14/01, 17/01 and 31/01 provide smaller productivities and 21/01 is the least performing.

To better understand the evolution of the performance during the experiments, the specific flow rates in [l/m^{2}h] have been calculated deriving in intervals of 500 s the masses recorded. For normalization purposes, the condensation surface on the cloth has been considered with an area of 125 mm × 20 mm. The results are plotted in figure 4.6. Test 28/01 shows a high peak value at the beginning, which quickly decreases and then slightly increases at the end. Also 16/01 and 21/01 see their performance decrease over the time but less heavily as they do not reach such a strong peak value in comparison to 28/01. Tests 14/01 and 17/01 show a quite stable flow rate after 4000 to 6000 s. Test 31/01, because of the different procedure explained above, after the second transient due to the activation of the refrigerated circulator, shows also a very stable performance after 7000 s.

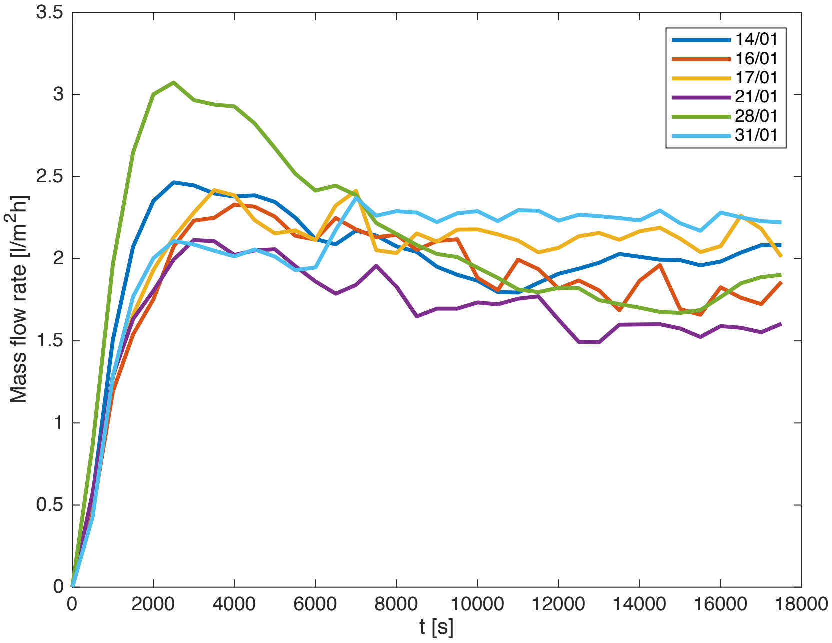

Figure 4.6: Distiller specific flow rates

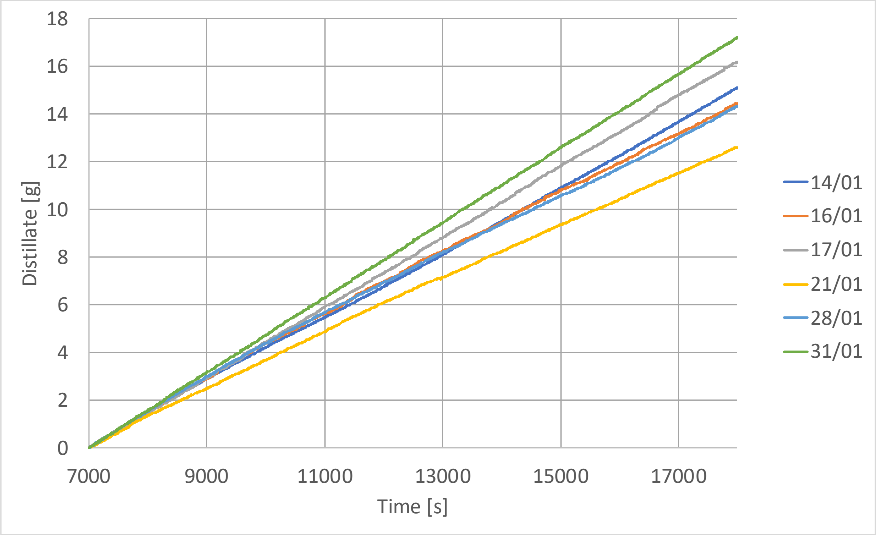

Figure 4.7: Distillate produced during steady state functioning

All the tests show values of specific flow rates very promising considered the fact that the distiller used here has only three stages, while theoretically the maximum output can be reached with approximately fifteen stages [6]. Always in [6], the distiller with three stages and 0,1 μm microporous membranes has a declared productivity of 1,442 l/m^{2}h under one sun, meaning that in this work the new design of the distiller allows a better performance.

To better see which one of the tests gave the best result during the steady state functioning the comparison is done considering the values recorded after 7000 s ≈ 2 h. In figure 4.7 are only plotted the relative values of distillate produced during each experiment during the steady state functioning.

Figure 4.8 depicts the boxplots of the flow rates of the six tests during the steady state functioning. It is possible to observe that test 28/01 is the least stable, while 31/01 is the most. 14/01, 16/01 and 28/01 have comparable performances, while 17/01 and 31/01 show a positive net distinction and 21/01 is visibly inferior. An additional analysis can be carried out observing the temperature profiles existing in the device during each test.

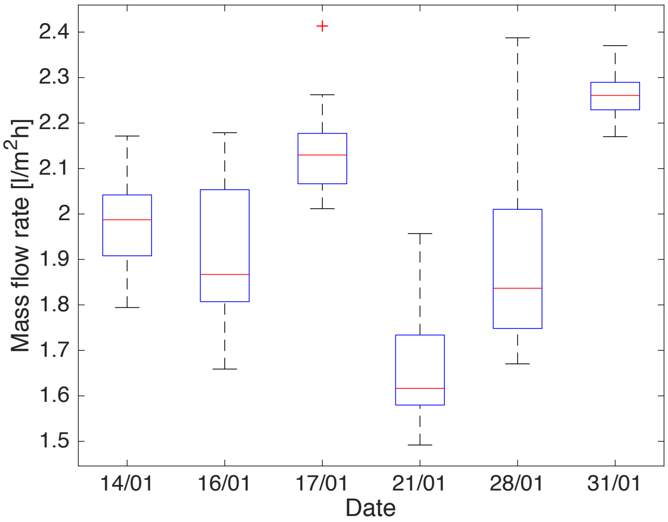

Figure 4.8: Boxplots of the specific mass flow rates: values recorded after 2h.

Figure 4.9 plots the difference of temperature between *Evaporator 1* and *Condenser 3* during the various tests (see figure C.1). As explained in section 2.4, the distillate productivity is closely related to the gradient of temperature. First of all it can be seen that the gradient existing at 300 s, i.e. when the distiller starts producing enough distillate, is around 5 to 7 °C. After roughly 2500 s ≈ 40 min, the system reaches its steady state temperature, meanwhile it reaches the peak rate of productivity. Although tests 16/01 and 17/01 are very similar in their temperature profile, their steady state flow rate aren't. They reach the same peak value but then in 16/01 its performance declines contrary to the other. 14/01 reaches a greater ΔT so it happens to its peak flow rate. However, again its performance decreases with time. The same occurs in an even more pronounced way during

28/01. 31/01 is interesting because it clearly shows the strong correlation between ΔT and J. The temperature profile shares the same shape with the plot of the productivity. It can be seen that when the refrigerated circulator is switched on at 6000 s, the gradient of temperature increases similarly to the flow rate.

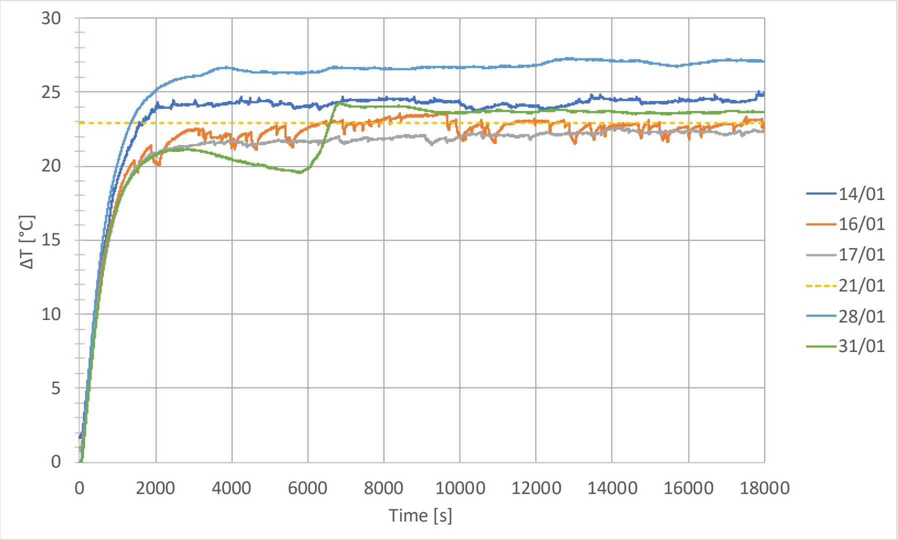

Figure 4.9: Temperature gradients between Evaporator 1 and Condenser 3

Table 4.1: Results of the performance tests: the steady state is considered after 7000 s.

	14/01	**16/01**	**17/01**	**21/01**	**28/01**	**31/01**	**Mean value**
V_{dist} (global) [ml]	25,00	23,52	25,58	21,04	26,36	25,91	$24{,}57 \pm 2$
V_{dist} (steady) [ml]	9,51	9,45	10,30	8,25	9,40	11,02	$9{,}65 \pm 0{,}93$
J (steady) [l/m^{2}h]	1,981	1,904	2,134	1,659	1,890	2,260	$\mathbf{1{,}971 \pm 0{,}2}$
ΔT (steady) [°C]	24,32	22,77	22,13	22,87	26,87	23,72	$23{,}78 \pm 1{,}62$

In table 4.1 are summarised the results of the six tests as well as their mean values. For the flow rate and temperature, the uncertainty was calculated as:

$$u = 2 \cdot \sqrt{\frac{\sum_{i=1}^{6} \sigma_i^2}{6^2} + \frac{\sigma_R^2}{6}} \tag{4.1}$$

where σ_i are the standard deviations of each test and σ_R is the standard deviation of the mean values. Some comments need to be made:

- The tests were carried out with a good level of reproducibility, except from test 31/01 which has been done differently. By the way, after its second transient, also this test managed to become similar to the others. The differences depend on the uncertainties in the initial assembly of the set-up during each test.
- The mean specific flow rates calculated during the steady state functioning allow to evaluate the performance of the distiller and to make it comparable with other

configurations of the same. However, the condensation surface of this device is smaller than the actual surface which receives the heat flux. A distiller occupies a surface of 125 mm × 35 mm, so if the distillate output is referred to the actual surface exposed to the sun, then its value should be 43% smaller. This value must be taken into account during the design phase of a system made of multiple distillers like this.

- The mean flow rate of the six tests is high in comparison with the distillate productivity of the 3-stage distiller in [6] and the other passive technologies cited there. It shows how this technology of desalination is promising compared to other low-price and passive technologies.

In conclusion, after this campaign of experiments the potential of the distiller has been confirmed to be important. More and longer tests could permit to better study the steady state functioning, here just evaluated along 3 h. Improvements in the precision of the assembly procedure should be performed, time and equipment permitting. The results obtained are already the product of many improvements adopted during the weeks of the campaign. Thanks to this characterization it is now possible to estimate partially the performance of the entire prototype object of this work. The experimental campaign was also useful to understand part of the critical aspects in the design of the distiller which needs to be replicated in other seven identical and functional copies.

4.1.4 Heat transfer properties characterization

Besides the performance tests, also the thermal properties have been studied, because some quantities were necessary for the simulations. In addition to distillation perfomance tests, also a characterization of the aluminium heat sink, and of the radiative properties of the PV panel, have been done.

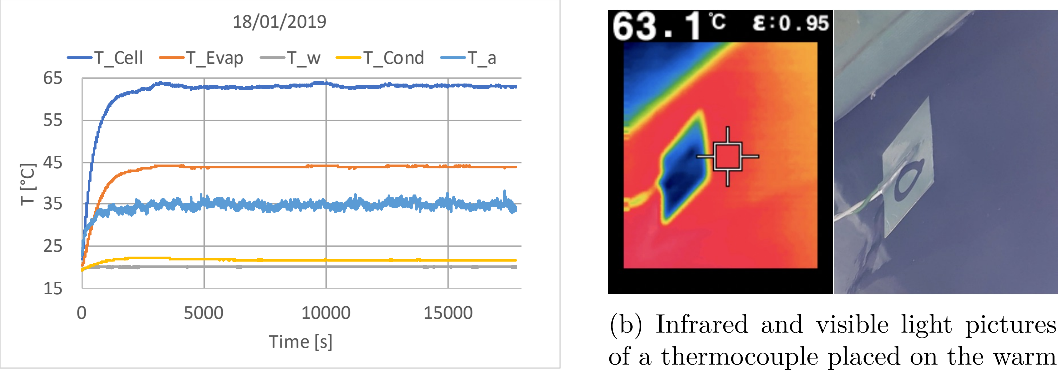

(a) Temperature profile of test 18/01

(b) Infrared and visible light pictures of a thermocouple placed on the warm panel

Figure 4.10: Emissivity characterization

During test 18/01, the emissivity coefficient of the solar panel ε was estimated with a thermal camera. On the surface aimed with the camera, a thermocouple measured the temperature. By adjusting the emissivity considered by the camera to evaluate the temperature of the irradiating surface, the goal was to match the temperature read on the camera with the one measured by the thermocouple. In figure 4.11a the cell temperature reached an average steady state value of 63,2 °C, which approximately corresponded to an emissivity $\varepsilon = 0{,}95$ of the panel. Figure 4.11b shows how this value has been obtained. While the scope aims at the surface, the thermocouple measures the surface's temperature. The thermocouple is sticked with aluminium tape, which appears blue because of its much lower infrared emissivity.

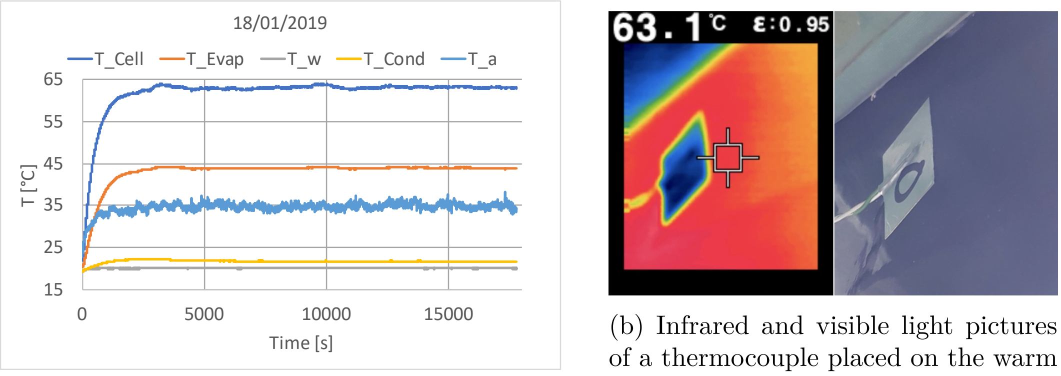

(a) Temperature profile of test 18/01

(b) Infrared and visible light pictures of a thermocouple placed on the warm panel

Figure 4.11: Emissivity characterization

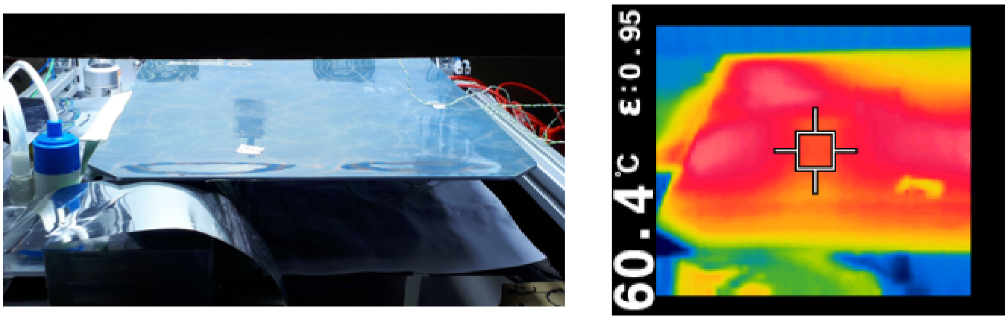

(a)

(b)

Figure 4.12: Visible light and infrared pictures of the warm panel on top of the distiller

During this same test, thanks to the thermal camera, the cooling effect by the distiller on the PV cell is reported. In figure 4.12b the focus is on the area on top of the panel affected by the distiller just below it. The distiller acts as a heat sink on the warm panel, which is proved by the orange rectangular shape seen on the infrared picture, corresponding to the location of the distiller below the panel. The thermal camera also proves that this cooling phenomenon exists because it shows a temperature of 60,4 °C, 3 °C less than the temperature measured in figure 4.11b, which has been measured close to the distiller. For this reason, test 31/01 was carried out with the thermocouples placed differently. Figure 4.13 shows how the thermocouples have been placed on the top (4.13a) and bottom (4.13b) surfaces of the panel just over the location of the distiller.

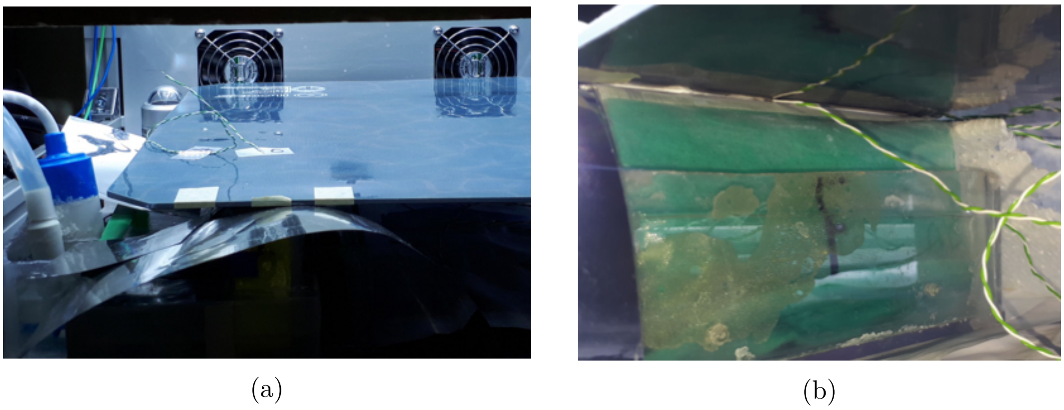
(a) (b)

Figure 4.13: Location of thermocouples on the panel during test 31/01

Observing the temperature profiles in figure C.1, is evident the difference between the temperature of the panel above the distiller and next to it. The latter ranges from 63 °C to 67 °C while, in the particular case of test 31/01, the panel above has an average temperature of 56,7 °C and below of 52,8 °C. This demonstrates the synergic effect which is capable to achieve this configuration made of the PV panel coupled with the distiller. The first provides the heat flux necessary to start the distilling process, meanwhile the latter cools the cells, allowing a gain in efficiency.

The additional experiment to complete the heat transfer characterization consisted in evaluating the heat transfer coefficient of the heat sink, with its fins partially dipped in non-stagnating water. The refrigerated circulator has been implemented identically as during the distillate performance tests, keeping the water temperature at 20 °C. Electrical resistors were sticked on the top surface of the heat sink, which wasted by Joule effect a certain power corresponding to the equivalent incoming heat flux of 1000 W/m^2. By measuring the temperatures on the top surface of the heat sink, of air and water, it was possible to calculate the heat transfer coefficient.

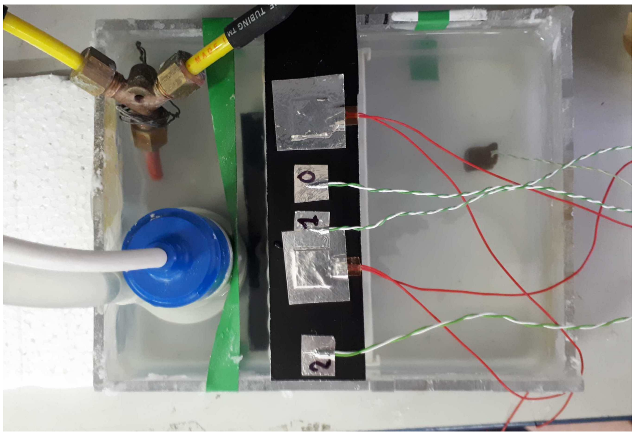

Figure 4.14: Heat sink characterization

The set-up used was made of:

- Aluminium heat sink;
- Variable power supply;
- Resistors;
- Refrigerated circulator;
- Basin for water.

Three thermocouples placed as shown in figure 4.14 measured the temperature of the top surface. This surface was then insulated to dissipate the incoming heat only in the other directions. Since this surface measures 141 mm × 33 mm, the power required to satisfy the heat flux is 4,653 W. With the power supply delivering 16,3 V × 0,29 A = 4,727 W, the equivalent electric heat flux was then $q_{el} = 1016$ W/m^2. After the transient, the steady state mean temperatures recorded during 10 min are listed in table 4.2.

Table 4.2: Average temperatures in °C during the heat sink characterization

$\boldsymbol{T0}$	$\boldsymbol{T1}$	$\boldsymbol{T2}$	$\boldsymbol{T_w}$	$\boldsymbol{T_a}$	$\boldsymbol{T_{HS}}$
21,71	21,8	21,55	20,76	21,18	21,68

T_{HS} is the temperature of the heat sink, being the average of $T0$, $T1$ and $T2$. Since water and air had a similar temperature, and knowing that stagnating air has a negligible heat transfer coefficient compared to circulating water, only the contribution of the latter has been considered to evaluate the heat transfer coefficient of the heat sink. The equilibrium is described by the following equation:

$$q_{el} = U_{HS}(T_{HS} - T_w)$$

The result is $U_{HS} = 1106$ W/m^{2}K. However, an additional estimation was further carried out to measure the thermal resistance of the set-up made of the aluminum plate below the last condenser and sticked to the heat sink. Figure 4.15 shows that the thermocouple recording the temperature of condenser 3 during the performance experiments touches the aluminium plate placed on top of the heat sink. The parts are joined with one strip of double-sided tape, which has a non negligible thickness, which means that an air gap is partially established between the two. This thickness has been measured and is worth $s = 0{,}2$ mm. Considering the tape and the air acting like parallel resistances, and the first occupying 40% of the surface, the transmittance of the junction is worth:

$$U_{gap} = \frac{k_a \cdot 0{,}6 + k_{tape} \cdot 0{,}4}{s} = 478 \text{ W/m}^2\text{K}$$

with $k_a = 0{,}026$ W/mK and $k_{tape} = 0{,}2$ W/mK. Being the heat sink and the gap two series resistances, the effective output transmittance is:

$$U_{out} = \left(\frac{1}{U_{HS}} + \frac{1}{U_{gap}}\right)^{-1} = 334 \text{ W/m}^2\text{K}$$

Thanks to this value it is now possible to better simulate the system in order to complete a full characterization.

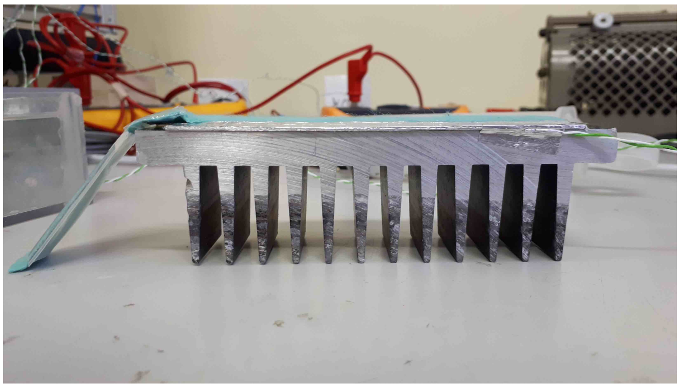

Figure 4.15: Heat sink with condenser 3 and thermocouple location

4.1.5 Analysis of unsuccessful performance tests

Many trials resulted non acceptable because the criteria imposed were not respected, namely a stable productivity after a transient part and no contamination of salt in the distillate. Here are shown some examples and their causes explained. The very first series of experiments started in December, with an experimental set-up in which there was no controlled refrigeration of the saltwater in the feeding basin.

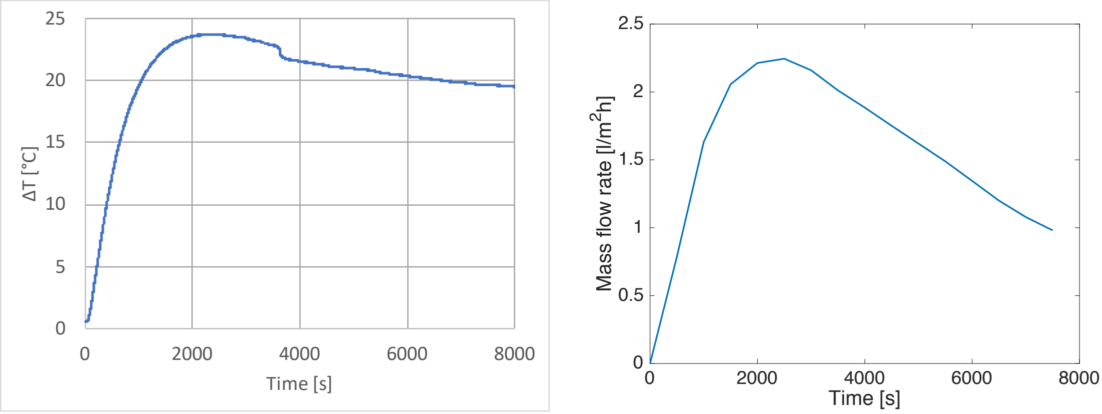

(a) (b)

Figure 4.16: Test 21/12/2018

Figure 4.16a shows the temperature gradient during test 21/12. It can be observed how the system reaches a peak value but afterwards this gradient decreases due to a quicker rise of temperature of the water in the basin, which leads to a growth of the temperature of condenser 3. This partially explains the trend of the specific mass flow rate in figure 4.16b. In fact, as shown previously in subsection 4.1.3, ΔT and J are related each other. Furthermore, during this test the distiller experienced a performance decrease by over 50% in less than 2 h 15 min. The identified cause was the loss of distillate by evaporation from the condenser cloths. The issue was mainly solved by insulating properly the condenser layers in the outer part. By covering with plastic the whole outer part, evaporation of the distillate just produced was avoided. This enhancement leaded to test 14/01.

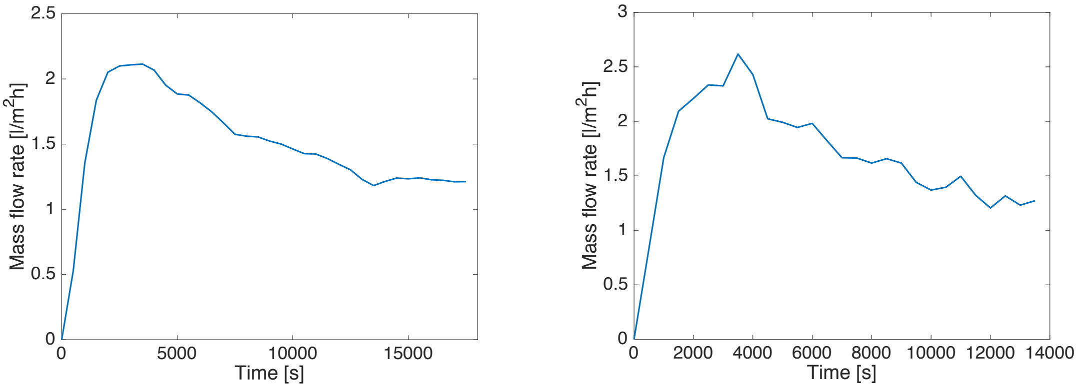

(a) Test 15/01/2019

(b) Test 25/01/2019

Figure 4.17: Specific flow rates of tests 15/01 and 25/01

Figure 4.17 shows two unsuccessful tests. In figure 4.17a test 15/01 experienced a strong decrease after reaching the peak, declining up to 1,2 l/m^{2}h. Even worse during test 25/01 (figure 4.17b), which was executed after the renovation of the distiller, and during which the performance dropped even quicker. The explanation for the first was probably an incorrect mounting of the pieces during the assembly phase described in subsection 4.1.2. For 25/01, the explanation was due to an incorrect design in the lateral sealing of the condensers, which caused again non negligible lateral losses of vapour of distillate.

An unsuccessful test could also be caused by contamination of salt in the distillate. Contamination is only caused during the functioning by some saltwater passing through the membrane, meaning that the membranes were worn out or that the *Liquid Entry Pressure* (LEP) peculiar of the membrane has been exceeded. Wearing happens over the time while repeating several tests in which, during the assembly and disassembly, the manipulation causes small damages to the PTFE layer of the membrane. Overpressure, inversely, is only caused while compressing the distiller too much, or if a small object (e.g. a thermocouple) is introduced in between a cloth and the membrane. In this second case, already a small compression is enough to wear and reach the LEP. Figure 4.18 compares the state of wearing of three membranes used differently. To obtain the picture, the membranes must first be wet in order to highlight damages, i.e. oversized pores and scratches, which absorb water and make transparent the membrane. The first on the left has been used correctly during the tests, so its appearance is only white. In the middle, the membrane has been manipulated in such a way that part of the hydrophobic layer has been scratched, which is visible in the black scattered spots. The last suffered from an overpressure: the scratches are more abundant and organized in a rectangular shape. The area corresponds to the condenser cloth lying underneath. While a small wear causes a small contamination, corresponding to 3 to 5 g/l of salt, overpressure brings it to values equal to the salinity of the evaporator layer just above it (i.e. 35 g/l or more).

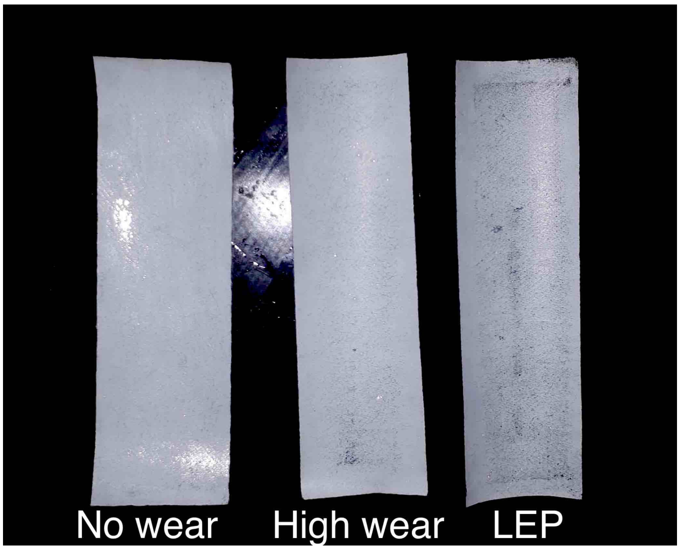

Figure 4.18: Comparison of wearing state in membranes

In conclusion, the system can be fragile because of its design and the materials composing it. Care must be taken during the assembly and disassembly in order to avoid all the issues described previously. Improvements in the global design also must be performed.

4.2 Physical modeling and simulation

This section is dedicated to the modeling characterization of the distiller, which allows to determine the gradient of temperature along the system in detail and to simulate the distiller under different conditions. The first part shows the model implemented and how the solution is carried out. A finite element model on a multiphysics software is also employed to validate the previous one and to better understand the phenomenon.

4.2.1 One dimensional model of passive membrane distillation

Here is explained a physical model which has been previously implemented in [6], but with some additional optimizations performed in this work in order to better fit the experimental results. The model allows to obtain in a unique solution the temperature profile along the different stages and layers inside them, as well as the heat fluxes and the specific flow rates of distillate. The model receives as input data the following quantities: the incoming solar flux q_{Solar}; the effective transmittances of the heat sink U_{out}, and of a cloth and aluminium plate together U_{layer}; T_a and h_a the temperature and heat transfer coefficient of the surrounding air; the air gap thickness d_a due to non ideal contact between membrane and cloth; the mass fraction Y_E of salt in the evaporator layers; the membrane porosity ϵ_m. The code implementing the model first calculates the activity in the evaporator layers $a(Y_E)$ via equation 2.31, the tortuosity τ via equation 2.28 and estimates the effective transmittance of the membrane U_{mem} as follows:

$$U_{mem} = \left(\frac{d_m}{\epsilon_m \cdot k_a + (1 - \epsilon_m) \cdot k_{PTFE}} + \frac{d_a}{k_a} \right)^{-1} \tag{4.5}$$

with k_{PTFE} = 0,25 W/mK. Then solves a system of non linear equations in which the variables are the temperatures and the specific heat fluxes calculated in several nodes corresponding to the boundaries between the different layers of the distiller.

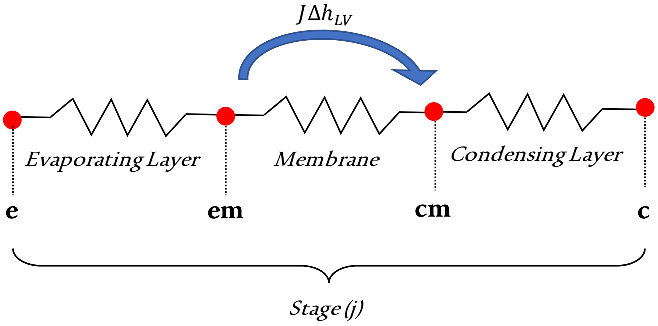

Figure 4.19: Equivalent thermal circuit of one stage of the distiller

Figure 4.19 shows the scheme of thermal resistances along the distiller, together with the heat flux carried by the mass transport of vapour across the membrane, which later condenses releasing the latent heat of vaporization Δh_{LV}. The red dots represent the thermal nodes of each stage. The system of equations for a stage j is, in the evaporating layer is:

$$0 = q_e(j) - U_{layer}(T_e(j) - T_{em}(j)) - q_{l,layer}(j) \tag{4.6a}$$

$$0 = \frac{S_{aluminium}}{S_{condenser}} \cdot q_e(j) - q_{em}(j) - q_{l,layer}(j) \tag{4.6b}$$

where q_e, q_{em} and $q_{l,layer}$ are respectively the specific heat fluxes: at the interface between the top surface of evaporator j and the previous stage; at the interface between evaporator and membrane; of the lateral convective losses in the layer. $S_{aluminium}/S_{condenser}$ = 1,4 is the ratio between evaporator (measuring like the aluminium plate) and condenser's areas. In fact, the heat flux (in [W]) goes through sections with different sizes, thus the specific heat flux (in [W/m^2]) changes depending on the section. Here, it passes from a wide to a narrow section. In the membrane the equations are:

$$0 = q_{em}(j) - U_{mem}(T_{em}(j) - T_{cm}(j)) - J(j)\Delta h_{LV} - q_{l,mem}(j) \tag{4.7a}$$

$$0 = q_{em}(j) - q_{cm}(j) - q_{l,mem}(j) \tag{4.7b}$$

where q_{cm} and $q_{l,mem}$ are respectively the specific heat fluxes: at the interface between membrane and condenser; of the lateral convective losses in the membrane. It can be seen in this case the contribution of the latent heat carried by the vapour transfer, represented by the term $J(j)\Delta h_{LV}$. $J(j)$ is calculated the same way as explained in subsection 2.4.2.

In the condensing layer the equations are:

$$0 = q_{cm}(j) - U_{layer}(T_{cm}(j) - T_c(j)) - q_{l,layer}(j) \tag{4.8a}$$

$$0 = q_{cm}(j) - \frac{S_{aluminium}}{S_{condenser}} \cdot q_c(j) - q_{l,layer}(j) \tag{4.8b}$$

where q_c is the specific heat flux at the interface between bottom surface of condenser j and the next stage. Here, the shape factor is applied inversely because the flux passes from the narrow to the wide section. The system is solved for $j = 3$ stages. The boundary conditions are:

- $q_e(1) = \varepsilon q_{Solar} - h_a(T_{Panel} - T_a) - \varepsilon\sigma(T_{Panel}^4 - T_a^4) + q_{Border}$;
- $j \neq 1 \Rightarrow q_e(j) = q_c(j-1)$;
- $q_c(3) = U_{out}(T_c(3) - T_w))$;

where $T_w = 20$ °C is the temperature of the saltwater; $T_{Panel} = 55$ °C is the average temperature of the panel above the distiller; σ is the Stefan-Boltzmann constant; ε is the panel's emissivity; $h_a = 5$ W/m^{2}K is the heat transfer coefficient of air; U_{out} is the output transmittance; $q_{Border} = 82{,}4$ W/m^2 is an evaluation of additional heat flux coming from the larger surface of the PV panel irradiated from the sun, which has been estimated via a 3D finite element model described in subsection 4.2.4. The flowchart in figure 4.20 shows the computations performed for the model.

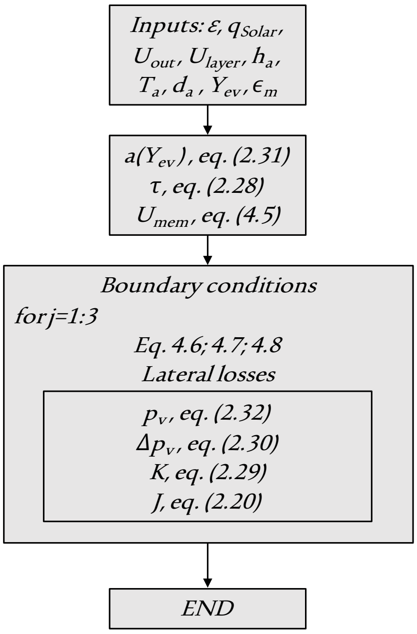

Figure 4.20: Flow chart of the one dimensional distiller model

Thanks to this model, it is possible to simulate a variety of different situations and validate it to the experimental data. In this work, the model has been run with the heat transfer properties measured experimentally and with further approximations and assumptions in order to fit it to the experimental temperature profile of the distiller and specific mass flow rate of distillate.

4.2.2 Preparatory study of the input quantities for the simulations

In this section, the model simulates different operating conditions of the distiller based on the random combination of the eight input arguments stated previously. First are explained the reasons that justify the choice of the ranges of the input variables listed in table 4.3.

Table 4.3: Ranges of input variables used in the simulations of the one dimensional distiller model

	$\boldsymbol{\varepsilon q_{Solar}}$ **[W/m^2]**	$\boldsymbol{U_{out}}$ **[W/m^{2}K]**	$\boldsymbol{U_{layer}}$ **[W/m^{2}K]**	$\boldsymbol{h_a}$ **[W/m^{2}K]**	$\boldsymbol{T_a}$ **[°C]**	$\boldsymbol{d_a}$ **[mm]**	$\boldsymbol{Y_E}$	$\boldsymbol{\epsilon_m}$
min	860	320	360	3	33	0,01	0,033	0,75
max	1060	350	400	7	40	0,09	0,037	0,85

The modeling of the incoming heat flux is affected by the optical properties of the PV panel, as well as the influence of the surrounding ambient and the border effects due to the larger size of the absorbing surface, i.e. the panel. Figure 4.21 depicts the various contributions.

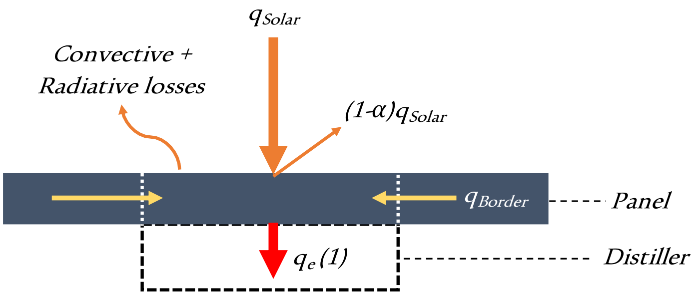

Figure 4.21: Scheme of thermal balance on the PV panel

The first assumption is to consider the panel as a gray body, thus claiming the equality between the absorbance α and the emissivity $\varepsilon = 0{,}95$ estimated in subsection 4.1.4. Its value is considered in a range of ±5%. Moreover, the value of solar flux q_{Solar} is affected by uncertainty due to non uniformity of the beam, accounting for ±51,3 W/m^2 as obtained in subsection 4.1.2. The combination of the range on the emissivity value, plus the uncertainty applied to $q_{Solar} = 1000$ W/m^2, confer the values of εq_{Solar} in the table. Since the panel is a gray body, the radiative losses will be affected also by the variability of the emissivity coefficient.

The thermal conductivity of the layer has been estimated with the following formula [31]:

$$k_{layer} = k_f + r\frac{k_w - k_f}{r_c} \tag{4.9}$$

in which $k_f = 0{,}04$ W/mK is the thermal conductivity of the dry fabric, $k_w = 0{,}6$ W/mK of the water, r is the ratio between the mass of water and the mass of the fabric and r_c is the critical value in which the fabric is saturated with water. From experimental evidence $r \approx 6{,}1$ and $r_c \approx 8$, leading to $k_{layer} = 0{,}5$ W/mK. For a 1,2 mm thick aluminium plate and a 1,3 mm thick cloth, the overall transmittance is $U_{layer} = 360$ W/m^{2}K. The range considers ±5% of the calculated value.

$U_{out} = 334$ W/m^{2}K and $Y_E = 0{,}035$ are just affected by ±5% uncertainty. T_a comes from experimental evidence. h_a is estimated via some calculations of natural and forced convection at low speeds. ϵ_m is taken from [6]. The air gap thickness between membrane and cloths is the most uncertain value, for this reason it has been chosen equal to $d_a = 0{,}5$ mm±0,4 mm.

4.2.3 Testing and analysis of results of the one dimensional model

In this part the conditions of the parameters described above are applied and the results discussed. It is then analyzed how each variable individually affects the system. A last brief study is performed on a hypothetical optimization of the distiller depending on the design variables.

First the model is run with the central values of the parameters in table 4.3, which are taken here as reference conditions.

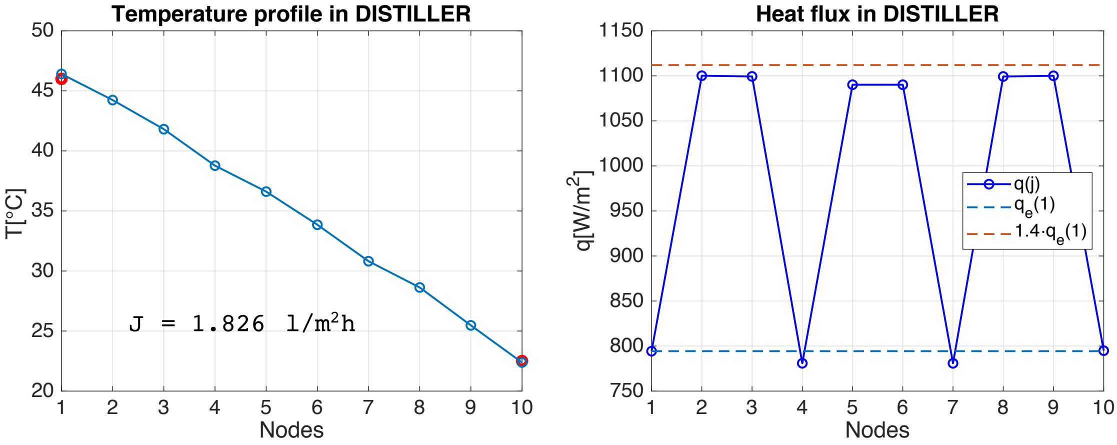

Figure 4.22: Temperature profile and specific heat flux in the distiller. Reference conditions applied in the simulation.

These conditions have been chosen because they allow the model to match its temperature profile with the average experimental temperatures, which are respectively 46 °C in

Evaporator 1 and 22,5 °C in *Condenser 3* as shown in figure 4.22. With these conditions the specific mass flow rate calculated is $J_{sim,ref} = 1{,}826$ l/m^{2}h, which is less than the average experimental value of subsection 4.1.3 but fits in its uncertainty interval, namely $J_{exp,m} = 1{,}971 \pm 0{,}2$ l/m^{2}h. It is important to know that the nodes corresponding to the boundaries of the membranes are nodes 2; 3; 5; 6; 8; 9. The value of each $J(j)$ is strongly related to the temperature gradient across the boundaries of each membrane and to the mean temperature of the membrane, as shown in table 4.4. Even with smaller ΔT on the membrane, the warmer stages produce more than the colder ones.

Table 4.4: Results of the simulation under reference conditions

	Stage 1	**Stage 2**	**Stage 3**
$T_{em}(j)$ [°C]	44,24	36,61	28,63
$T_{cm}(j)$ [°C]	41,81	33,85	25,47
$\Delta T_{mem}(j)$ [°C]	2,43	2,76	3,16
$T_{mem,m}(j)$ [°C]	43,03	35,23	27,05
$J(j)$ [l/m^{2}h]	0,752	0,605	0,469

Figure 4.22 shows on the right side the specific heat flux flowing through the different layers of the distiller. Its trend is due to the shape factor, which causes the rise and drop of its value. The specific heat flux increases from the evaporator to the membrane, while it decreases in the condenser, in each stage. Furthermore, it can be noted the effect of the lateral convection, which acts as a loss from node 1 to 5: $q(2)$; $q(3)$ and $q(5)$ decrease in comparison with the upper limit $S_{aluminium}/S_{condenser} \cdot q_e(1)$. The same happens to $q(4)$ from the lower limit $q_e(1)$. From node 6 the temperature goes below the ambient temperature at 35 °C, which turns the lateral convection into a source of heat, increasing again the values of $q(j)$.

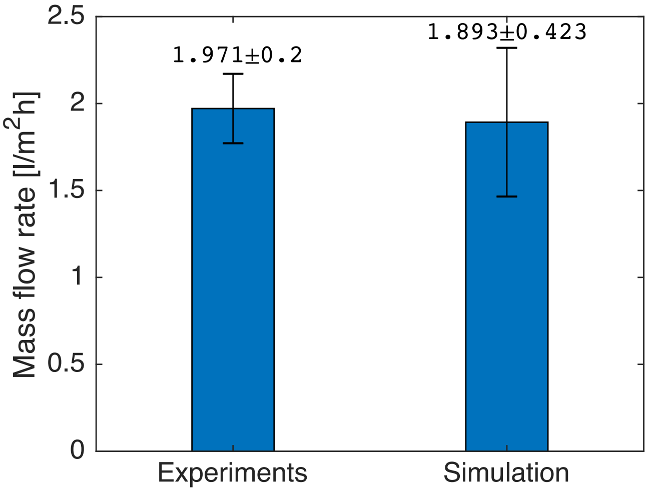

Figure 4.23: Experiments and simulation comparison with mean values and error bars: Result for 500 random simulations considering combination of variables from table 4.3.

Starting from one reference condition, the model is now run with many combinations of input arguments. Each parameter from table 4.3 is affected by a uniform distribution, and the model choses a value in each of them randomly for 500 cases. The global result of the simulation is $J_{sim,m} = 1{,}848 \pm 0{,}413$ l/m^{2}h. The uncertainty value on the simulation corresponds to 1 standard deviation. Figure 4.23 compares this result with the experimental ones. The average value of the simulations is 4% lower than the experimental evidence. The experiments with their uncertainty manage to fall inside the range of uncertainty of the simulations, thus it can be claimed that the model is validated.

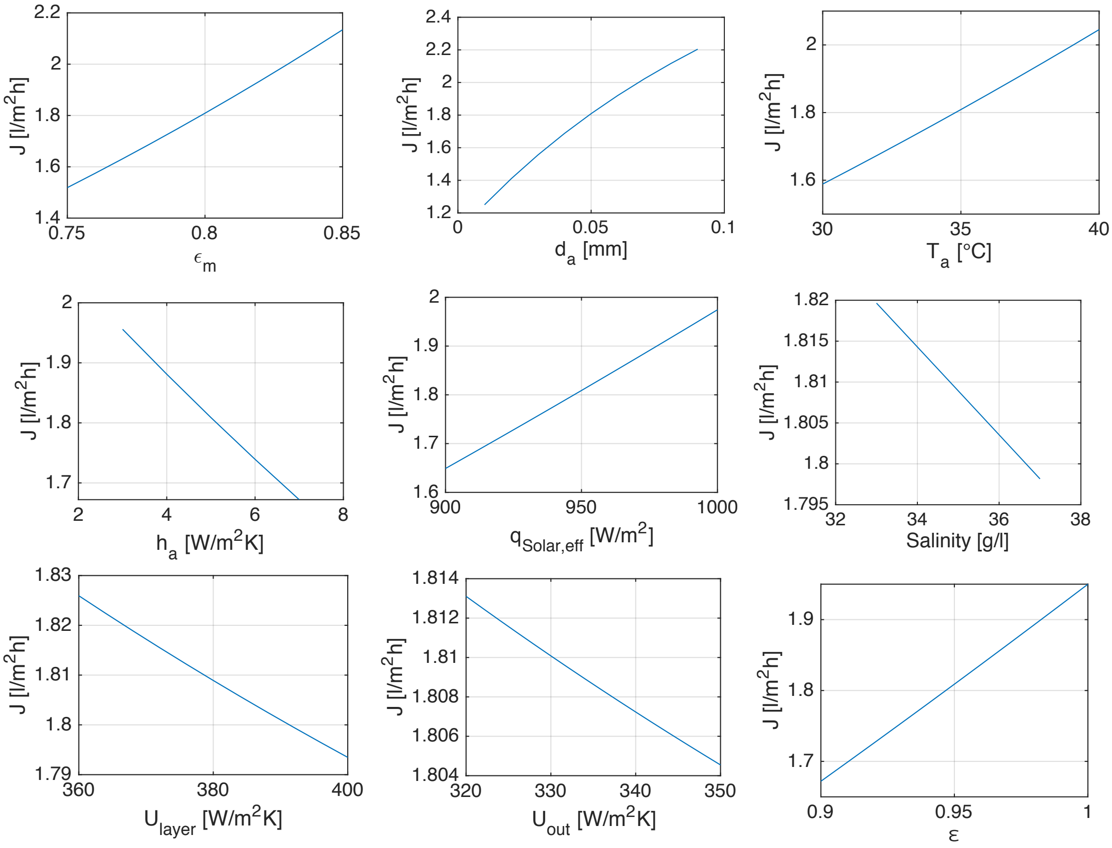

Figure 4.24: Comparison of effect of the parameters on the distillation performance: variation from reference conditions.

By running the model varying only one parameter per time in the range defined previously, the charts in figure 4.24 show the effect of each of them alone on the global performance of the distiller. Some comments can be made:

- Porosity allows a variation of ±14%. Porosity is a characteristic of the membrane employed and varies depending on the material and on the wear state. It affects both the mass transport via the permeability coefficient K and the heat transfer via the membrane transmittance U_{mem}. A larger porosity increases the mass transport and adds more thermal insulation, thus increasing the temperature gradient across the membrane. However, by removing completely the membrane, i.e. having $\epsilon_m = 1$ along the overall gap, the risk of saltwater contamination and losses of distillate due to evaporation increases.

- d_a makes the distillate flow to vary from -33% to $+19\%$. It affects both the mass transport and the thermal insulation. A bigger air gap reduces the first and increases the second. Observing the chart, the increase in performance due to thermal insulation gets weaker and the mass transport resistance stronger. In this case only an air gap caused by a non ideal contact is considered, however it indicates a clue for a hypothetical optimization in which a spacer with a precise thickness can be placed between the membrane and the condenser. Again this solution could increase losses of distillate due to evaporation.

- The convective contribution to the global heat flux flowing from the distiller to the external environment is controlled by T_a and h_a. The analysis can only be approximate as h_a depends also on T_a. The chart of T_a states that the performance should increase because of smaller convective losses on the top surface of the panel. If this is partially true because it allows to keep the system warmer, it is also true that a warmer surrounding air can increase the risk of losses due to evaporation. Moreover, a well ventilated panel, i.e. a bigger h_a, keeps its temperature lower so the global performance decreases.

- The incoming solar flux affects closely the performance. Upwards it is limited by the power of direct sunlight, as the current system cannot be employed in a solar concentrator. However, in the range studied here, the performance decreases by 11%, reaching a still acceptable value.

- In this application, which is distillation of sea saltwater, small salinity differences weakly affect the performance of the distiller. For bigger salinities, the loss would be not negligible and moreover it would have to be studied the effect of fouling and scaling, which would further decrease the performance.

- U_{layer} is bound to the amount of water the capillary cloth can absorb. A dryer cloth increases the thermal insulation so the performance, but a dryer cloth means that it is less capillary, which is a fundamental peculiarity searched to make the system work.

- U_{out} interferes weakly with the range of variability considered here, but a gain in productivity can be obtained reducing its value to a lower magnitude, allowing to increase the average temperature but also increasing the risk of evaporation.

- A bigger emissivity ε of the solar absorbing surface, corresponding also to the absorbance α, obviously allows to absorb more solar power. The counter effect of radiative loss is overcome by the gain in absorption. In this work where the PV panel acts as the solar absorber, the emissivity and the absorbance cannot be different between each other. However, selective solar absorber materials (e.g. TiNOX®) with high α and low ε are commercially available.

This analysis gives some possible indications for a hypothetical optimization of the system in the case of a redesign. A design parameter easily editable is U_{out}. Yet the membrane characteristics are less flexible because they depend on the technology of the membrane. Adding an artificial air gap is also a viable optimization solution. The other parameters are fixed or not pertinent as redesign parameters.

4.2.4 Three dimensional model for thermal profile validation and energetic analysis

To better understand the heat transfer phenomena occurring inside the device, a three dimensional finite elements model is implemented in this subsection. The software used is COMSOL Multiphysics®. This part describes how the model was built, the boundary conditions which have been applied, the results of the simulation and the energetic contributions in the system. In figure 4.25 is shown the geometric model of the system studied.

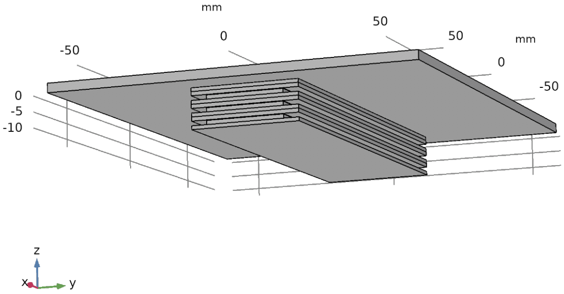

Figure 4.25: 3D model of the system

On top there is one fourth of the PV panel leaning on the distiller. The amount and order of the layers, constituted by evaporator and condenser cloths, membranes and aluminium plates, is the same as what described in subsection 2.4.1; just the heat sink has not been represented but has been replaced by a proper boundary condition. It is important to note the already mentioned difference in width between evaporators, which measure 35 mm, and condensers, which measure 25 mm.

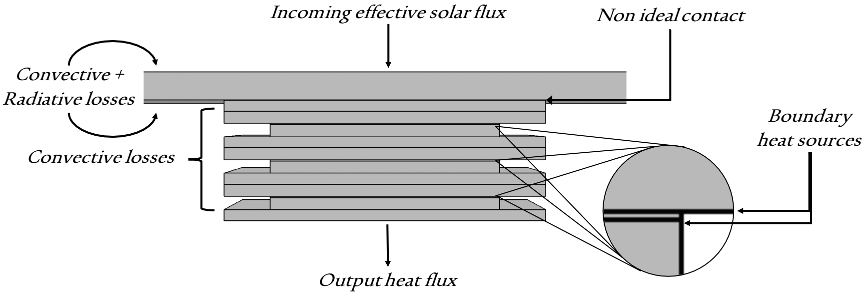

Figure 4.26: Scheme of boundary conditions in the model

The external contributions to the functioning of the system have been modeled via the boundary conditions depicted in figure 4.26. The incoming solar flux, the output heat flux due to the heat sink and the convective and radiative losses have been applied coherently with the one dimensional model. Moreover, a non ideal contact between panel and distiller, which is modeled with a contact resistance, has been added to better match the experimental temperature profile with the simulated one. Eventually, to model the heat transfer by vapour generation and transport across the membrane, boundary heat sources have been calculated as $J(j)\Delta h_{LV}$ and applied on both sides of the membranes. The results are depicted in figure 4.27

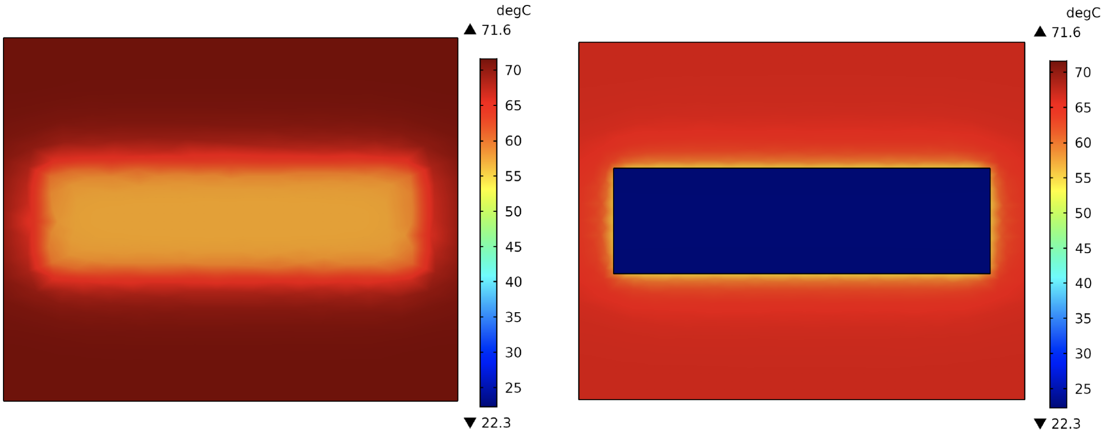

(a) Top (Temperature) (b) Bottom (Temperature)

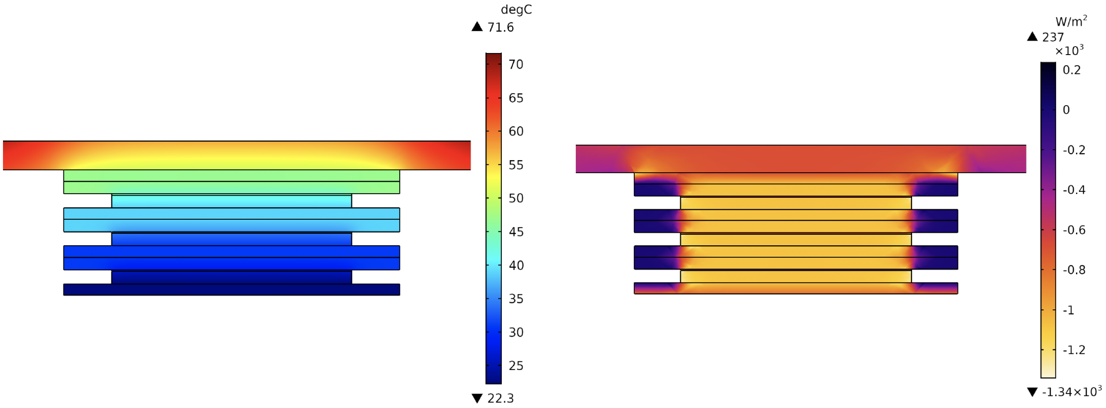

(c) Frontal middle section (Temperature) (d) Frontal middle section (Vertical heat flux)

Figure 4.27: Superficial temperature and heat flux profiles

In figure 4.27a it is possible to note the presence of the distiller under the panel acting as a heat sink, as already seen in figure 4.12b. On the cooled area the panel has a temperature of 57 °C, whereas far from it is of 70 °C. On the bottom side, the panel is cooler, with a temperature approximately of 65 °C. Figure 4.27c shows a net distinction of the temperatures between the panel and the first aluminium plate due to the non ideal contact between them. In the distiller layers it is already possible to see a temperature profile similar to the experimental one, with the first aluminium plate at 46 °C and the last at 22,3 °C. Figure 4.27d demonstrates how the vertical heat flux is more intense in the narrow sections, measuring around 1100 W/m^2, while is negligible on the sides of the wide sections. At the contact between the panel and the first aluminium plate it is possible to note the concentration of the flux from a wider to a narrower section. These results have been compared with the one dimensional model to verify the coherency between both models. Figure 4.28 depicts the temperature and heat flux profiles obtained with the two models.

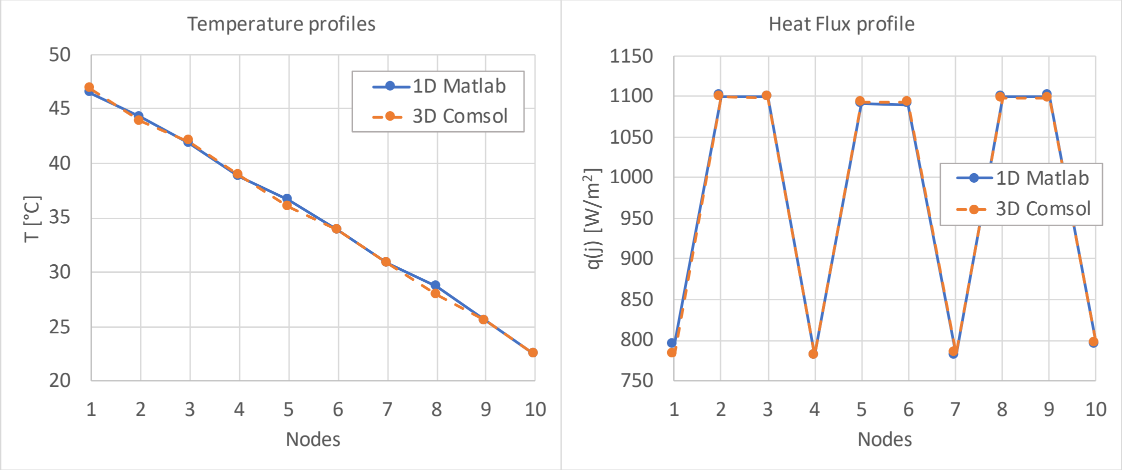

Figure 4.28: Comparison between 1D and 3D models

The differences are small for both profiles, just the temperatures in nodes 2, 5 and 8, corresponding to membrane temperatures T_{em} for all the three stages, are underestimated in the 3D model by respectively 0,89%, 1,72% and 2,68%. All the other quantities match closely for both profiles, thus the two models can be considered to be verified by each other.

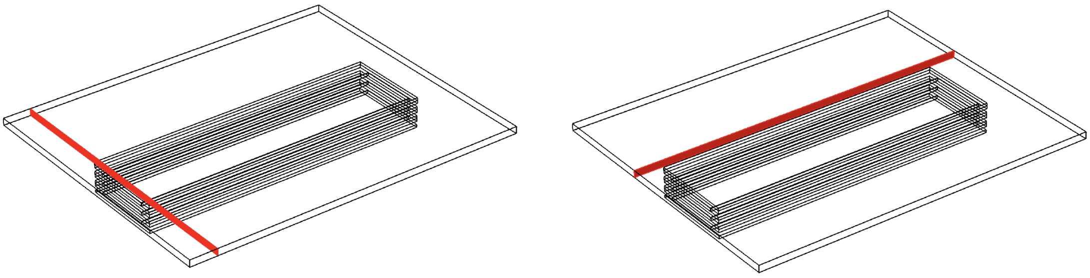

(a) Frontal section

(b) Lateral section

Figure 4.29: Sections studied for the evaluation of border effects in the panel

The solution of the two models is the result of an iterative process, in which one depends from the other. In fact, while the 1D model allows to calculate the specific flow rates $J(j)$, the 3D model is necessary to calculate the border effect contribution to the overall incoming heat flux in the distiller, previously mentioned as q_{Border}. To calculate this magnitude, first the heat fluxes flowing horizontally in the panel have been evaluated in the highlighted sections depicted in figure 4.29. Their mean values are respectively $q_{x,Frontal} = 142{,}2\ \mathrm{W/m^2}$ and $q_{y,Lateral} = 444{,}4\ \mathrm{W/m^2}$. By integrating the first along the two frontal sections measuring 3 mm × 35 mm, and the second along the two lateral sections measuring 3 mm × 125 mm, the overall power incoming from the borders is equal to 360,4 mW. Dividing this value by the aluminium plate area, the additional incoming flux from the borders is equal to $q_{Border} = 82{,}4\ \mathrm{W/m^2}$.

Here it is now performed the energy balance of system thanks to the results obtained with the 3D model. Two reference volumes are considered, which are the part of the PV panel immediately above the distiller, and the distiller throughout its layers.

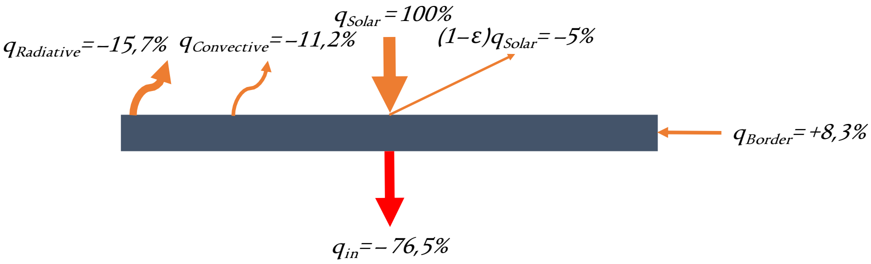

Figure 4.30: Energetic balance on the panel's control volume

The first principle energy balance applied to the first control volume shown in figure 4.30 is:

$$q_{Solar} - (1-\varepsilon)q_{Solar} - q_{Convective} - q_{Radiative} + q_{Border} - q_{in} = 0 \tag{4.10}$$

The result is that the major losses are due to radiative exchange with the ambient, followed by the convection and reflection. The border effects manage to rise positively and with a non negligible 8,3% the overall heat q_{in}, which is finally transferred to the distiller (see table C.2).

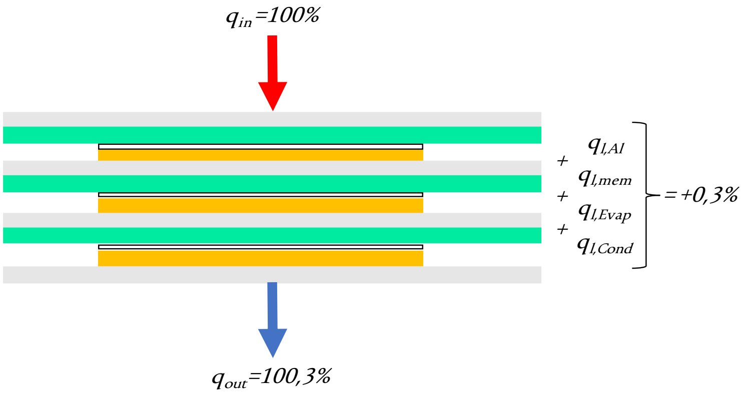

Figure 4.31: Energetic balance on the distiller's control volume

On the distiller's control volume, the lateral convective exchange on the aluminium plates, membranes and cloths summed eventually add a small 0,3% to the heat dumped by the heat sink. The detail of the quantities obtained for the energy analysis are listed in table C.3. This result is coherent with the trend of the heat flux profile in figure 4.28.

The last analysis relates to the energy consumption of the distillation process and to the efficiency of the distiller. The energy consumption per cubic meter produced of distillate is worth:

$$C_d = \frac{q_{in}}{J_{exp,m}} = 388 \text{ kWh/m}^3 \tag{4.11}$$

The consumption is lower by almost 40% with respect to the one of traditional solar stills, which needs 640 kWh/m^3 [32]. This demonstrates the effectiveness of the heat recovery implemented by the distiller thanks to its three stages, in which the two stages after the first one use the latent heat released by the previous stage. In a ten stage configuration, this value has reached 150 kWh/m^3 [6]. As the system generates as unique useful effect the production of distillate, because no power is collected from the panel in the experiments by not connecting its plugs to any user, the efficiency of the overall system will depend only on the amount of distillate produced. The efficiency of a single stage is expressed as follows [6]:

$$\eta(j) = \frac{J(j)\Delta h_{LV} S_{condensation}}{q_{Solar} S_{aluminium}} \tag{4.12}$$

where $S_{condensation}$ = 125 mm × 20 mm and $S_{aluminium}$ = 125 mm × 35 mm. However, in this case the distiller has many stages in which the heat flux carried by the vapour transport in one stage is recovered and used to feed the next stage. This forces to define as *Gained Output Ratio* (GOR) the ratio between the useful product of all the stages and the heat flux provided [33]:

$$GOR = \frac{J_{Tot}\Delta h_{LV} S_{condensation}}{q_{Solar} S_{aluminium}} \tag{4.13}$$

The results for simulated reference conditions and experimental data are listed in table 4.5.

Table 4.5: Efficiencies of single stages and GOR of the distiller. The results obtained for stages 1, 2 and 3 and for Total$_{sim,ref}$ are calculated with values from simulations under reference conditions. For Total$_{exp}$ the result is obtained using experimental values.

	$J\Delta h_{LV}$ [W/m^2]	$\eta(j)$ [%]	GOR [%]
1	482,8	27,6	
2	390,2	22,3	
3	304	17,4	
Total$_{sim,ref}$	1177		67,3
Total$_{exp}$	1243,9		71,1

The GOR demonstrates the ability of this technology to rise the overall efficiency by recovering the latent heat, as its value is about three times the value of the efficiency of the single stages.

In conclusion, the system made of one distiller fed by the waste heat of a PV panel under reference conditions is now fully characterized. In the next chapters is presented and tested the prototype, which contains eight distiller modules identical to the one presented until here. The experiments will replicate similar conditions to what done in this chapter, so the expectations are to reach similar distillation performances and similar thermal profiles on the eight distillers.

Chapter 5

Prototype development

Until here the different systems discussed and tested have not been integrated in a unique and stable solution as the first objective was their individual study. Instead, the aim is now to couple the photovoltaic technology to the passive solar membrane distillation in a device able to guarantee their synergic operation. This chapter is dedicated to the process of design and manufacturing of the prototype discussed in this work, from its first conception to the final assembly. Technical drawings of parts and assemblies can be consulted in the attached documents.

5.1 Design

The design phase is crucial for the effective functioning of the prototype and depends closely on the external resources available, such as design softwares, materials and manufacturing techniques. The resources were provided mostly by the university and partially by personal contribution. Therefore, this section goes through the design process starting from the design criteria, the explanation of the choices made to end with the final concept.

5.1.1 Criteria

The first step in the design of the device is defining the criteria applicable to its intended use. As a passive technology is employed here, the output available is potentially enough to fulfill the energy and water needs of small numbers of people, such as small or impoverished communities, or endangered groups, for example on life-boats. So the basic paradigm is *simplicity*, which must be reflected in the design itself, the functioning and the maintenance. The second criterion, in accordance with the aforementioned needs, is to find a *low-cost* solution to the choice of materials and manufacturing. The device must have a small number of components, no mechanisms or electronics, and need occasional to no maintenance, with operations easy to perform.

The device must also fulfill a specified number of functionalities. It must integrate both the passive membrane distillation and the photovoltaic technologies. The first is obtained by implementing the device presented in subsection 2.4.1. It first needs a heat source, which here is provided by the back side of the PV module, and be fed by saltwater. The heat sink of the distiller is also partially dipped in saltwater. Inside the device, the distillate must be collected and protected from contamination and evaporation. The distillation process is done in the different layers. Finally, the goal is to maximize the output of distillate and the cooling of the cells of the PV module by adding the biggest possible number of distillers underneath the panel, in order to cover most of its surface. So the criteria necessary to make the device functional are to create a structure able to:

- Mount 8 distillers, 2 under each cell, as each PV cell measures 125 mm × 125 mm and each distiller only 125 mm × 35 mm (125 mm × 50 mm, if taking into account the additional space laterally occupied by the cloths);
- Guarantee the thermal contact between PV panel and distillers, i.e. all the distillers must be at the same height of the panel and positioned horizontally;
- Support the distillers vertically;
- Allow the feed of saltwater and dipping of the heat sinks;
- Collect and protect the distillate;
- Be opened easily with a reversible system in order to allow distillate collection and maintenance.

This list of criteria hides several constraints in dimensions and shape of the structure. All the elements need to be designed specifically for the different components which have to be coupled together in a unique device. In the next subsection are explained the technical solutions adopted in the design of the prototype.

5.1.2 Adopted solutions

To respect the criteria and the constraints aforementioned, the choices made are explained in the following lines. These choices depend also on the manufacturing techniques available, but these will be presented in the next section. The main idea in the design of the prototype is to enclose in a unique structure all the other functional components. Inside of it there are the eight distiller modules, which are fitted into their internal structures. On top of them is leaned the PV panel, which is clamped thanks to frames that are coupled with screws to the internal structures. In the remaining space between the internal structures, under the panel, are placed the distillate containers.

Figure 5.1 shows the most important dimensions necessary to the design phase of the internal structures. The idea is to hold the distiller from the edges of the heat sink, while letting free its fins to dive in the water together with the evaporator cloths. Upwards, the structure must reach the exact height of the stack of layers in order to allow the thermal contact between panel and distillers. To do so, a custom made part has been designed to accomplish these different tasks. This part, from now on called *base*, acts as a support for both the distillers and the panel. However it is not made in a unique piece but is decomposed in four components, one for each cell and couple of distillers, plus two other components which only work as supports for the rear part of the panel. The clamping of the panel on the bases is done by fixing it with frames screwed on the bases via wood screws, thus avoiding a threading operation of the holes during the manufacturing process. Figure 5.2 shows as example the part here called *base up-left*. The distiller must be placed inside of it, being oriented with the condenser cloths towards the lower walls of the base so that they can get into the interior of the device and spill the distillate in the containers. The higher walls act as support for the panel and protection from the seawater. The panel must be leaned on top of the base structure, next to the edges, over which the clamping frames are screwed.

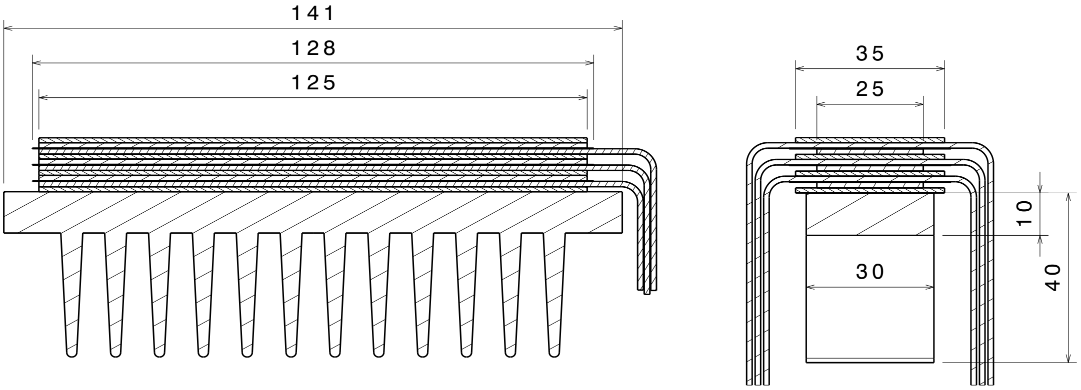

Figure 5.1: Sections of a single distiller module. Dimensions are indicated in mm.

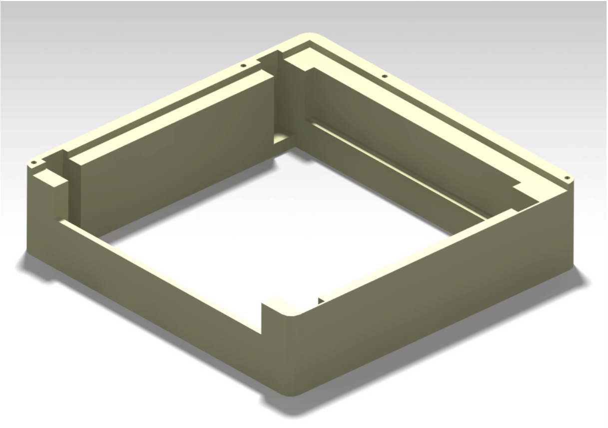

Figure 5.2: Rendering of part *base up-left*

Figure 5.3 highlights all the previously described functionalities the bases: in a base, the heat sink is fitted into it, its fins go below the bottom of the outer cover in the water, the condenser cloths stay inside the device and the green frames clamp the panel to the structure and guarantee the thermal contact with the distillers. Furthermore, the picture shows the external body made of a bottom structure and a top cover frame. Inside the device are placed the distillate containers. An additional component is the protection frame. As the bonding of the base structures and bottom structure is not guaranteed to be waterproof, as well as the material of the base structures (3D printed plastic), the protection frame is aimed to physically avoid saltwater to flood the interior of the structure by acting like a hull. These protection frames are four, one for each hole in the bottom structure, and are bonded to it. The overall result is shown in figure 5.4 while open (5.4a) and closed (5.4b).

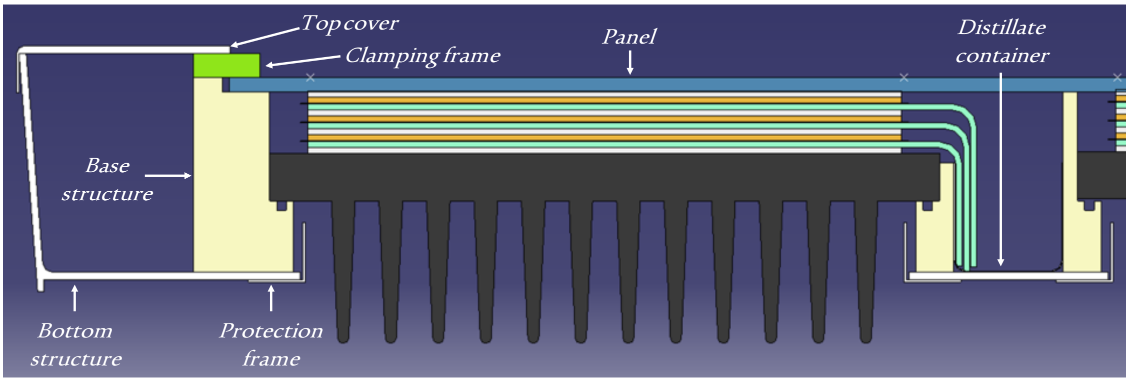

Figure 5.3: Detailed section of the prototype assembly

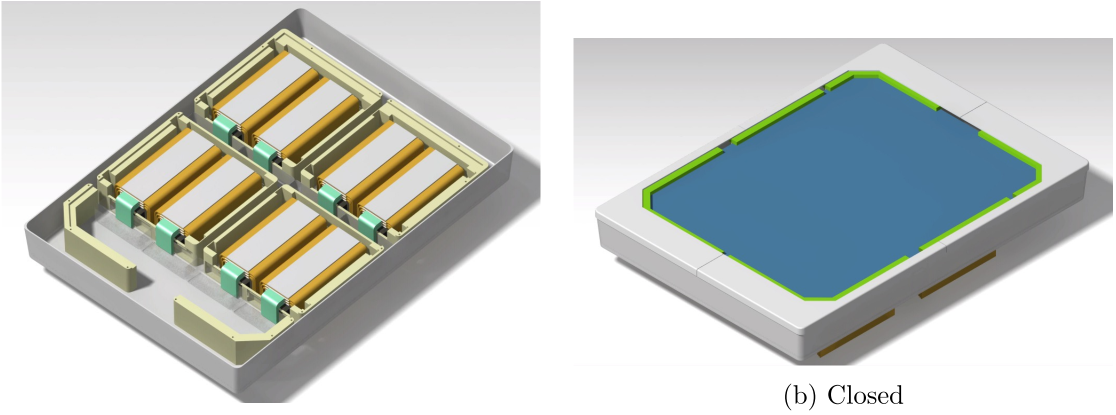

(a) Open

(b) Closed

Figure 5.4: Renderings of open and closed configurations of the prototype

Note in the open configuration that the distillers are all oriented with the condensers backwards, in order to reach the distillate containers. These have been placed in the available spaces existing in the area below the panel and inside the walls of the internal bases. Because of these dimensional constraints, the containers are tailor made too. Once all the distiller modules are mounted inside the prototype and the containers placed, the panel must be placed on top and clamped with the green frames with their screws. Eventually, the top white frames are fitted and complete the coverage of the device. A demonstration of the sequence previously described is shown in figure 5.5.

A simple design for both the distillers and structure is therefore demonstrated here. Their mounting requires easy operations: stacking the layers of the distillers, positioning of components and screwing. The total number of pieces to use during the assembly operations is also small and no moving parts or electronics are required. Furthermore, the electrical plugs of the PV module can be reached by slightly lifting the top covers on the back, allowing the device to be completely functional.

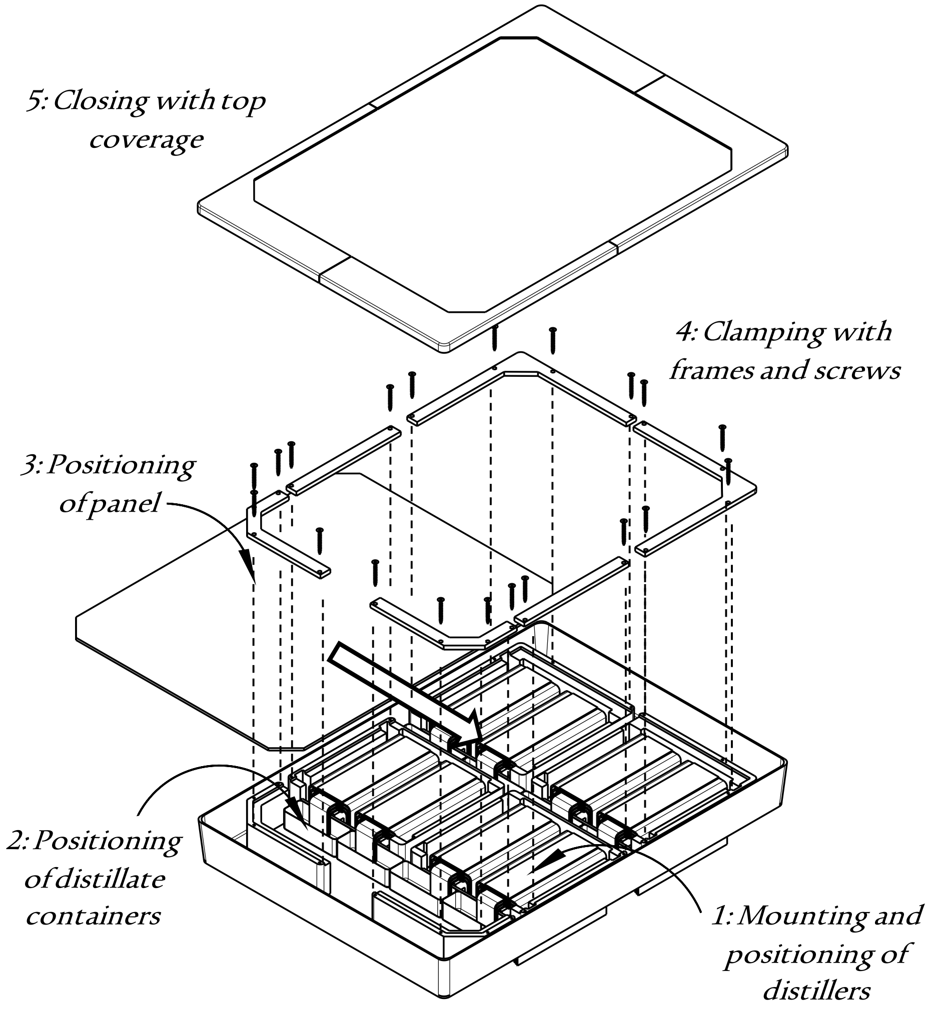

Figure 5.5: Exploded view of the prototype assembly and mounting sequence

5.2 Manufacturing and assembly

This section is dedicated to show which manufacturing processes have been employed and how the parts have been assembled. The processes and materials used were the one available at the university and from personal contribution. The prototype here discussed is mainly composed by the distiller modules and the structure, along with its coverage made with the top frames and PV panel.

The distillers are simple devices in both their components and assembly. Few parts and tasks are necessary to implement one. To create all the eight modules, the following operations were necessary:

1. Cut of hydrophilic cloths, 125 mm × 180 mm for the evaporators, 25 mm × 180 mm for the condensers, three of both for each distiller;
2. Cut with a jigsaw of four 125 mm × 35 mm aluminium plates for each distiller from an aluminium sheet 3 mm thick;
3. Cut of eight 30 mm × 141 mm heat sinks with a cutting machine starting from 100 mm × 160 mm aluminium heat sinks for electronics applications, and subsequent removal of two more fins (see figure 5.6) from each heat sink;

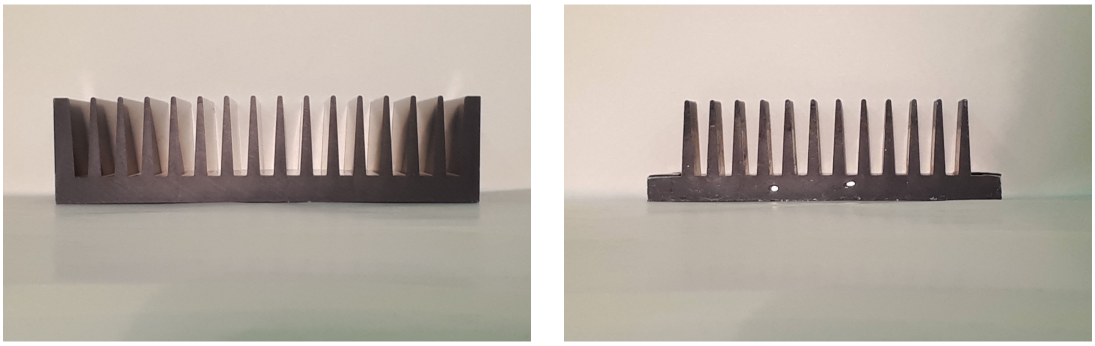

(a) Original part

(b) Custom part

Figure 5.6: Starting point and result of the manufacturing of the heat sinks

4. Bonding of layers in order to form four parts for each distiller (see figure 5.7) and sealing of cloths with plastic;
5. Cut of hydrophobic membranes (0,1 µm pores).

The result is a device in which the materials employed are relatively cheap: kitchen hydrophilic cloths, aluminium plates, PTFE membranes and an aluminium heat sink. The price could be further reduced by replacing the membranes with air gap spacers. The distiller is also easy to assemble because it just needs to stack the four components separated by the membranes.

The other parts of the prototype, namely the outer coverage, internal structures and containers, needed the following manufacturing processes:

1. Cut of four rectangular holes (see technical drawing *Box structure*) and shorten of the lateral walls of a polypropylene box to obtain the bottom structure;

Figure 5.7: Distiller module components. Starting from the left: the first component is Evaporator 1 bonded to the first aluminium plate; the second is Condenser 1 with Evaporator 2, separated by the second aluminium plate; the third is Condenser 2 with Evaporator 3, separated by the third aluminium plate; the fourth is Condenser 3 bonded to the fourth aluminium plate and the heat sink.

2. 3D printing in ABS of the internal structures with a semi-professional, temperature controlled 3D printer, and of the clamping frames with an amateur 3D printer;

3. Production of protective frames, distillate containers and top covers via manual vacuum thermoforming. For this process, wooden moulds (see figure 5.8a) have been specifically created for each different component. The materials employed were 0,2 mm thick polyethylene for the protective frames and containers, and 1,7 mm thick PE for the top frames. After the thermoforming phase, the semi-finished products needed to undergo a cut of the exceeding material and refining. Furthermore, the top covers have been painted in white.

(a) Moulds

(b) Finished products

Figure 5.8: Thermoforming phase

4. Bonding of the protective frames to the bottom of the box structure, and bonding of the bases inside the box structure as depicted in technical drawing *Assembly structure* and figure 5.9.

Eventually, the prototype needs to be assembled as described in the previous subsection. The final result is shown in figure 5.10.

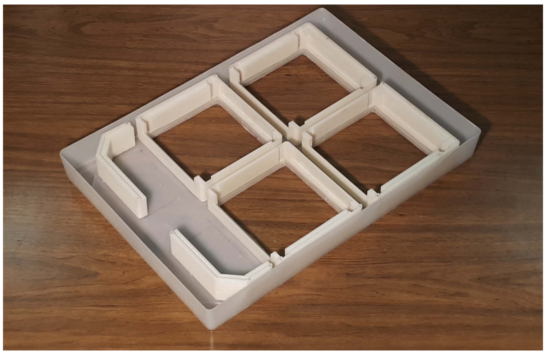

Figure 5.9: Assembled parts of the structure

(a) Open

(b) Closed

Figure 5.10: Prototype assembly

The choice of 3D printing does not agree with the need to reduce the cost of production, but was necessary because of its incomparable flexibility and capability for implementing the required parts. As this is only a prototyping phase, 3D printing is the least expensive way in term of time and costs to get the product done. Apart from that, the global assembly is cheap and easy to build and assemble. A demonstration of its use is presented in the next chapter.

Chapter 6

Prototype testing

6.1 Indoor experimental activity

In this section is presented the experimental campaign carried out to characterise the assembled device. This part shows the effectiveness of the designed prototype, furthermore demonstrating the initial goal to use the recovered waste heat of a PV module to feed the passive membrane distillers. The experiments here are done indoor to guarantee a good repeatability. The experimental set-up, planned procedure and results depiction and analysis are the contents of this section. Detailed results can be found in Appendix D.

6.1.1 Experimental set-up

In this part the global performance of the entire device is tested by measuring the total distillate production of the eight modules. The testing conditions are the same as those of chapter 4, namely incoming power equal to $E = 1000$ W/m^2, salinity of 35 g/l of sodium chloride in water and feed water's temperature of 20 ℃. The material employed is also almost identical and consists of:

- Prototype as shown in chapter 5;
- Solar simulator;
- Refrigerated circulator;
- Data acquisition hardware and software;
- 14 type K thermocouples;
- Pyranometer;
- Saltwater basin;
- Refractometer.

The set-up is made by positioning the prototype on the supports built inside the container, and by placing them under the solar simulator. The level of saltwater is set to ensure that the prototype dives roughly of 3 mm from the bottom side of the structure. So, the fins of the heat sink, as well as the evaporator cloths can be dipped in the water as required. Furthermore, by cooling the bottom of the structure, it is possible to reduce the temperature inside the prototype in order to avoid the evaporation of the distillate.

Figure 6.1: Experimental set-up for prototype testing

The temperature of the feed water is controlled by the refrigerated circulator. The various thermocouples measure the following temperatures: cells 1 and 4 on the bottom side; air inside the device in two points, one above distillate containers A, B, C and D, and one above containers E, F, G and H; air above the panel; water; evaporator 1 and condenser 3 of distiller modules A, B, G and H (nomenclature of cells and distillers are in accordance with figure 6.2).

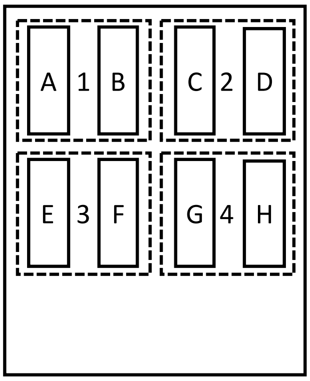

Figure 6.2: Nomenclature scheme: numbers refer to cells, letters to distiller modules and corresponding containers.

Thanks to these temperatures it is possible to evaluate the temperature distribution throughout the panel, i.e. how effective is the cooling provided by the distillers on the cells of the PV panel, and to calculate the temperature gradients that drive the distillation processes in the distillers. Since the distillate containers stay inside the device, which is closed during the test, the only way to evaluate the performance is to measure their weight before and after the test, and calculate a differential mass flow rate. Salinity of saltwater is checked before and after each test, and the salinity of the distillate is checked at the end of the trial.

6.1.2 Experimental protocol

The experimental protocol was made of some preparatory operations and then a list of operations repeated in each test. The first step was to set the power emitted by the lamp similarly to how it was done in chapter 4 by measuring it in nine different points as shown in figure 6.3. The result is an average incoming flux of 1032,6 W/m^2 with a standard deviation of 71,9 W/m^2. The results are presented in Appendix D.

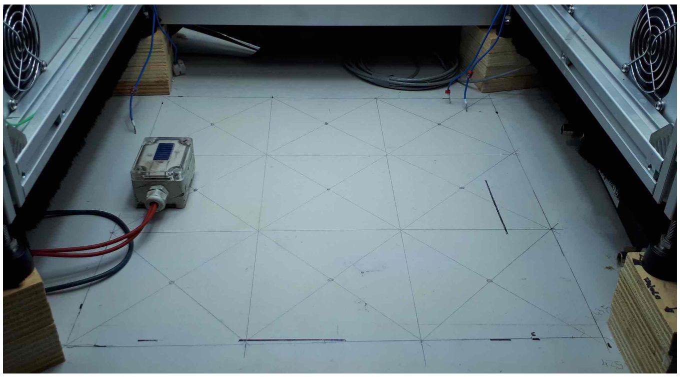

Figure 6.3: Measurement points of the heat flux test

The device then had to be assembled inside the sun simulator. The first time the cloths had to be humidified to reduce transient time. Every distiller had to be assembled by stacking over each other all the layers and by positioning the thermocouples, and then had to be placed in their corresponding positions inside the structure. The device was then placed in the saltwater container, which was then filled to the requested amount. To moisten the condensers, the distillate containers were filled with freshwater. To guarantee the initial hydration of all the cloths, this operation lasts 30 minutes. After this time, the distillate containers were emptied. Once this preliminary phase was completed, the following operations were done each time:

- Check of saltwater salinity before the test;
- Filling with 9 ml of freshwater each distillate container in order to dip already the extremities of the condenser cloths and facilitate initial distillate collection;
- Weighing of tare weight of distillate containers before running the test;
- Positioning of distillate containers inside the device;
- Closing of the device with the panel, the clamping frames and the top covers;

- Activation of the refrigeration circuit;
- Launch of the test for 5 hours;
- Opening of the device and collection of distillate containers;
- Weighing of distillate containers, calculation of net weight of distillate produced, and check of salinity of distillate;
- Check of saltwater salinity after the test.

Between each trial, the prototype was kept assembled and inside the sun simulator. This choice was made because the distillers were able to release by diffusion, during the several hours that separated each trial, the accumulated salt in the evaporators as explained in chapter 2. Then, the aim was to test the prototype in realistic conditions of continuative use, i.e. where the maintenance operations only come after many days. Another reason was also to avoid a time wasting repetition of preliminary operations each day, which could have furthermore added a risk of an inadequate assembly because of the increased complexity of this system.

6.1.3 Results and data analysis

This campaign of tests was pursued during five continuous days, namely during 6/05, 7/05, 8/05, 9/05 and 10/05/2019. The results obtained after each trial were the masses of distilled water produced by each distiller, from which the average specific mass flow rates have been calculated considering the difference of weight of the distillate containers before and after five hours of test. The only exception is for test 6/05, which lasted only four hours. The results published here constitute partially successful tests, i.e. the salinity of distillates was equal to 0 g/l but not all the modules managed to work with their nominal potential.

Table 6.1: Volumes of distilled water produced by the eight modules. 4 h operation for 6/05, 5 h operation for the others.

ΔV [ml]	**6/05**	**7/05**	**8/05**	**9/05**	**10/05**
A	21,34	16,25	14,71	15,57	9,94
B	19,7	18,07	17,24	16,75	11,2
C	23,83	16,51	15,58	7,91	5,67
D	20,14	13,48	11,55	11,64	11,1
E	17,98	17,62	2,75	1,91	0,73
F	21,36	20,63	12,88	18,38	18,04
G	3,1	2,64	-0,59	3,65	3,31
H	17,47	15,15	10,08	12,48	12,2
Total	144,92	120,35	84,2	88,29	72,19

Table 6.1 displays the amount of distillate produced by each module during each day of test. Some comments follow these results: it first can be seen a common decreasing trend for all the modules along the days. Module G never worked and module E stopped

working after 7/05. For this reason, these unsuccessful data are not considered for the following analysis of this subsection, hence modules E and G are excluded from the study. The table shows also the total amounts of distillate produced by the prototype. During day 1, this amount was equal to 145 ml, but it could have been potentially of 205 ml if distiller G worked and if the test lasted 5 h.

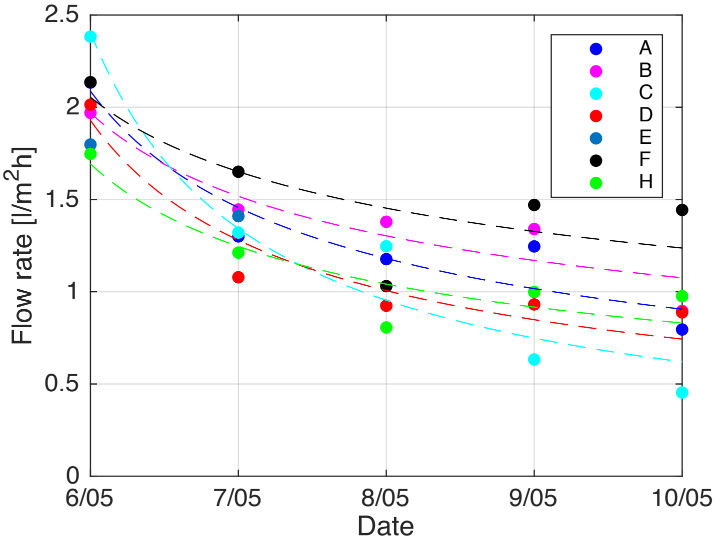

Figure 6.4: Average flow rates during the tests and interpolation curves of each module. Module G is not considered and module E is only displayed for tests 6/05 and 7/05. Flow rates of 6/05 are calculated over 4 h meanwhile the others over 5 h. Interpolation curves are power laws of the type $f(x) = ax^b + c$

Figure 6.4 shows the flow rates obtained from the data of table 6.1. The interpolation curves help in noticing the common decreasing trend in performance of all the modules and can show that some distillers performed better than others. In fact they all show a quite unstable behavior during the days. The modules are characterized by different levels of decrease during the time: module C suffered the most; module A and D slightly less; B, F and H had a less severe decline. This not homogeneous behavior is due to the uncertainty of the assembly operation of the distillers.

Figure 6.5 shows the mean values and error bars of the distillate flow rates of the modules over the five days campaign. Distiller F was the most effective with a mean value of 1,55 l/m^{2}h, followed by B and A at around 1,4 l/m^{2}h and eventually the others at 1,2 l/m^{2}h. These results are smaller by 20% until 38% from the experimental and the simulated results of chapter 4. The variability of the result over the time is very similar between different modules, apart from C which was the less stable. Their performances differ from each other of maximum 25%, which means that globally they had comparable flow rates. However, it must be reminded that distiller G failed completely and E partially for reasons explained later.

Table 6.2 shows the average temperature differential $\Delta T = T_{ev1} - T_{cd3}$, and mean

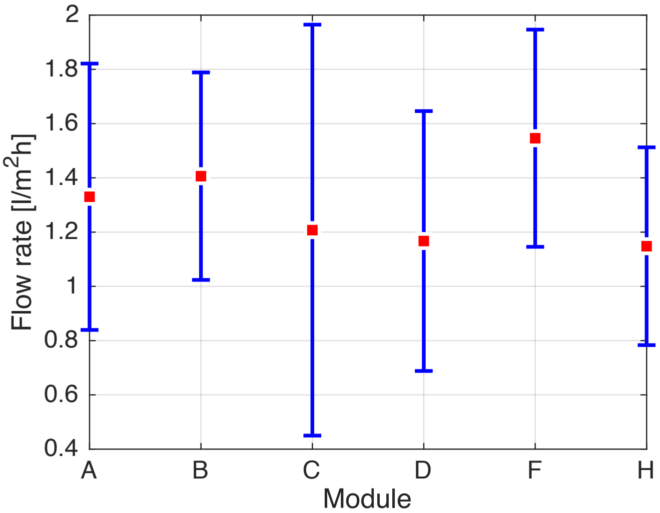

Figure 6.5: Average performance over five days of each functioning module

temperature $T_m = (T_{ev1} - T_{cd3})/2$, between evaporator 1 and condenser 3 of modules A, B, G and H during steady state operation and over the five days campaign. Since modules A, B and H show a similar temperature profile, it can be claimed that the difference in their performances is due to uncertainty in assembly. Theoretically, their flow rate should be around 1,8 l/m^{2}h as calculated by the 1D model. For module G, its temperature profile should be enough, according to the theoretical model, to guarantee a specific distillation flow rate of 1,4 l/m^{2}h. However, no distillation occurred, thus the cause cannot be the insufficient temperature, but only be an assembly problem.

Table 6.2: Global average temperature differentials and mean temperatures of the modules. Steady state is considered as achieved after 1 h of operation.

	A	**B**	**G**	**H**
ΔT [°C]	22,81	21,56	17,86	21,50
T_m [°C]	34,13	33,09	33,78	35,04

The global performance of the prototype over the time is also computed. Figure 6.6 shows how the system suffers from a decrease of its performance. During day 1, it performed a mean value of 2 l/m^{2}h, which is in accordance with the experimental results of chapter 4 of both simulations and experiments. In fact, day 1 reproduced the same conditions of those previous experiments as all the components were new and without any possible salt accumulation in the cloths and membranes. Already after day 2, the performance dropped by 45%. The decrease then seems to stabilize, eventually achieving a 55% decrease after five days.

Considering the results, some global comments are hereby made:

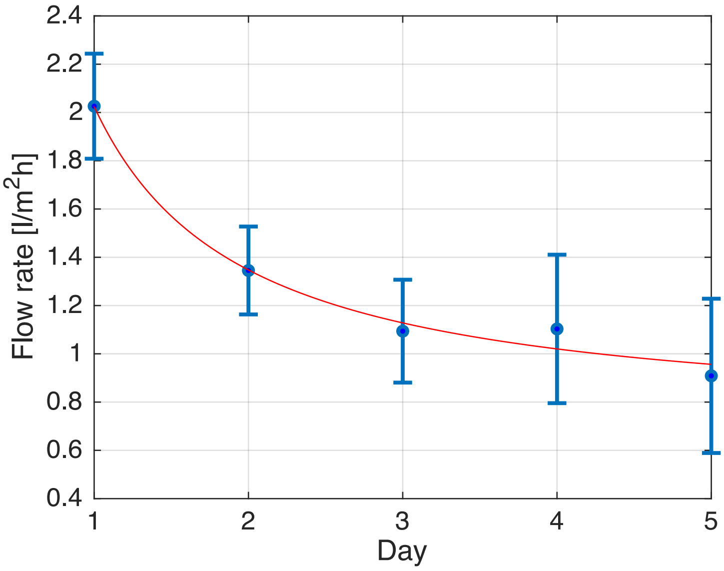

Figure 6.6: Average performance of the prototype during each test and interpolation curve

- From figure 6.5 it can be claimed that the distillate productivity of the passive distillers is quite uniform. However, these values are from 22% to 42% lower than the mean value of 1,971 l/m^{2}h of chapter 4, in which the conditions were the most favorable. The global mean value of productivity of the passive distillers in the prototype is **1,301 ± 0,318 l/m^{2}h**, 34% less than in the best case.

- The trend shown in figure 6.6 can be explained by the phenomenon of *scaling*. Such phenomenon is the progressive clogging of the membrane pores due to the forming of salt crystals on the membrane surface. [25] Although the evaporator cloths manage to clean themselves during nighttime by salt concentration gradient, the salt accumulated on the surface of the membrane gets inside the pores and may not be able to diffuse back to the cloths, so to the source. For this reason, the system would require a rinsing of the membranes or more simply their replacement in order to be effective over the days. These solutions are partially against the main design principles of simplicity, total passivity and little to no maintenance: rinsing or replacement could require the user to open and disassemble the modules, which takes time and adds risks of bad assembly. Otherwise rinsing could be automated using the electric energy produced by the PV panel, thus transforming the device from *passive* into *self-sustained* but with increased complexity.

- Module *G* probably failed because of unexpected errors during its construction or mounting into the device. Instead module *E* stopped working because of an error in assembly. During the collection of distillate after day 2, a mistake in manipulation occurred which caused a reassembly of said distiller. This shows the intrinsic lack of reliability of the technology as currently implemented in this work. With a structured case for the distillers, designed expressly to guarantee a correct and always reversible assembly of the parts, this issue would probably not appear again.

- Another issue of the system is the strong risk of evaporation of the distillate from the distillate basins and the related dipped cloth. During preliminary tests, which results are not presented in this work, after five hours of operation no distillate at all was collected. The containers were completely or almost dry but a clue of the actual correct working of the distillers, e.g. higher salinity of evaporators, showed the cause of the problem. To avoid it, it was necessary to implement two solutions: immersing the prototype some mm under the level of the saltwater to cool the bottom of the structure, which also cools the distillate basins and thus the distilled water; sealing the top of the containers with plastic film leaving just a thin cut on them, enough to insert the condensers, in order to limit free evaporation. The evaporation of distillate happens because of the high temperature of air inside the device, as shown in figure D.1, which achieves up to 50°C. This shows another current issue in the design of the device, which would need a system, passive or active, to reduce the air temperature inside of it. Nevertheless, in a in field experiment, where the heat exchange with the ambient air should be more effective, the internal temperature should be lower, so the evaporation of distillate.

In conclusion, the experimental campaign was successful. The design is effective regarding both technology, structure and assembly, since it manages to distill water and with a satisfying performance. Nevertheless, many problems still affect it. First is a lack of reliability during assembly phase and ongoing operation. Second, the distillation performance is quickly hampered by membrane scaling. Third, there is the risk of loss of distillate due to evaporation. A redesign would be necessary to solve these problems. A completely passive solution cannot be able to work indefinitely, but could be sufficient to fulfill the drinking water needs during a temporary emergency situation. Otherwise, a switch to a self-sustainable but not completely passive design might be the aim for the next version of the system.

6.2 Energetic and exergetic analysis of the cogeneration system

The ultimate goal of this work is to provide a proof of concept of cogeneration between photovoltaic energy and passive membrane distillation. The idea is to use the waste heat from the back side of the PV panel to feed the distillation process and, to rise the electric efficiency of the PV by reducing its temperature. The prototype here tested is conceived to get both advantages. In this section this gain in efficiency is estimated, a global cogeneration efficiency of the system is calculated, and finally an exergetic analysis is made. Experimental data and simulations are used to carry out these analysies. Detailed results are shown in Appendix D.

First the efficiency gain of the PV module is evaluated. It was necessary to begin by measuring the temperature of the panel when exposed under the same conditions of the tests in section 6.1, but without the cooling effect from the distillers. The set-up was basically the same: the prototype was installed over the saltwater basin, closed with the panel and frames but without the distillers inside. Temperatures of cells 1, 2, 3 and 4 have been recorded and mean values calculated considering the steady state reached after 4 min. The result is a mean temperature of the cells of **62,4 °C** (see table D.4). Therefore, the PV efficiency gain is directly proportional to the mean temperature of the cells when the distillers are mounted. This value could not be measured from the experiments as the cells have a non uniform distribution of temperature when the panel is mounted on top of the distillers. So to evaluate it, a 2 dimensional model has been implemented in COMSOL Multiphysics®. The finite elements model is formed by a 140 mm × 140 mm × 3 mm part of the panel. The boundary conditions and mean temperature measurement have been performed in accordance with figure 6.7.

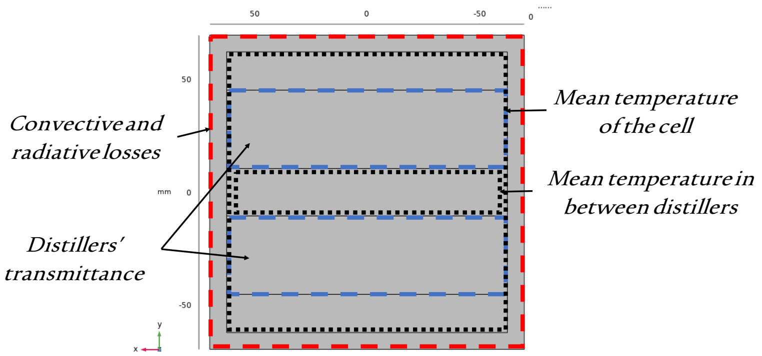

Figure 6.7: Control volume's definition of the 2D model. Red and blue surfaces relate to heat fluxes boundary conditions. Surface average temperature evaluations are made throughout the black rectangles.

On the rectangles highlighted in blue, representing the areas occupied by two distillers, distillers' transmittance has been applied. Its value is approximately equal to:

$$U_{distiller} = \frac{q_{in}}{T_{ev1,m} - T_w} = 31{,}2 \ \frac{\mathrm{W}}{\mathrm{m^2K}} \tag{6.1}$$

being q_{in} = 765 W/m^2 estimated in subsection 4.2.4, $T_{ev1,m}$ = 44,5 °C the average temperature of evaporator 1 during the experiments (see table D.5), and T_w = 20 °C the temperature of the saltwater in the feeding basin. On the top surface and bottom part not occupied by the distillers, convective and radiative losses have been applied similarly to subsection 4.2.4.

The cell's mean temperature in between distillers, evaluated in the rectangle highlighted in figure 6.7, is used to tune the boundary conditions in order to match its value to the experimental values T_{c1} and T_{c4} (see figure D.1). These temperatures are not the actual mean temperature of the cell, because they measure the temperature in the middle of it. In accordance with table D.5, the experimental mean temperature in between distillers is $T_{c14,m}$ = 59,4 °C and from figure 6.8b its simulated value is equal to 59,6 °C. An additional check is made on the temperature of the evaporators, which in the model reaches 45,9 °C, which differs only by +1,4 °C from the experimental one. The results of the simulations are shown in figure 6.8. The experimental assessment via a thermal camera capture is depicted in figure 6.9. The temperature profiles from figures 6.8a and 6.9b match in shape and values (e.g. in figure 6.9b the camera displays 63,1 °C, whereas in the same point measured in the simulation of figure 6.8a the temperature is about 64 °C). Note how in the infrared picture the distillers visibly manage to cool the cells. In fact, in both simulations and experiments, far from the distillers, the top surface of the panel reaches 70 °C while just above them it drops to around 54 °C.

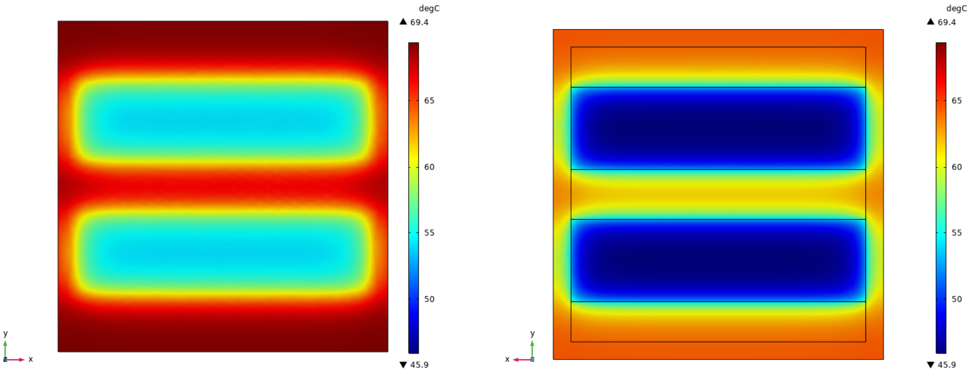

(a) Top (b) Bottom

Figure 6.8: Temperature profiles distribution in the PV panel, considering the coupling with the two distillers below the PV cell.

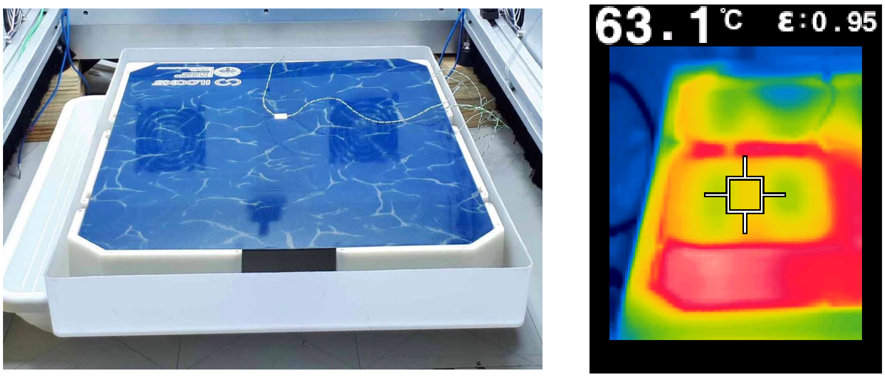

(a) (b)

Figure 6.9: Visible light and infrared pictures of the panel's area cooled by two distillers

As the model reproduces closely reality, eventually it can be used to evaluate the mean temperature of the cell, evaluated as the average surface temperature of the big 125 mm × 125 mm square in figure 6.7. This value is equal to $\boldsymbol{T_{cell,m} = 54{,}2\ ^{\circ}\mathrm{C}}$. It is now possible to estimate the efficiency gain depending on the reduction of the cell's temperature, which affects the maximum power via its temperature coefficient $k_P = -0{,}0361$ W/°C. The absolute efficiency gain is:

$$\Delta\eta_{PV} = \frac{k_P(T_{cell,m} - T_{uncooled})}{E_0 A_{cells}} = +0{,}47\% \tag{6.2}$$

whereas the relative gain, if the maximum power at $T_{uncooled}$ is $P_{mpp}(T_{uncooled}) = 6{,}6$ W so its efficiency is $\eta_{PV}(T_{uncooled}) = 10{,}56\%$, is worth $\Delta\eta_{PV}/\eta_{PV}(T_{uncooled}) = +4{,}5\%$. So this system is able to provide a net efficiency gain to the PV module by recovering the waste heat.

The second part of this section is dedicated to the calculation of the various energetic contribution to the global efficiency. First the incoming useful power in the system, i.e. the solar flux collected by the cells only, as in the remaining portion of the panel (plastic) is immediately lost in heat:

$$P_{solar} = E_0 A_{cells} = 62{,}5 \text{ W} \tag{6.3}$$

As the distillers do not cover the whole surface of the cells, the amount that the eight distillers could potentially receive under direct solar irradiation is:

$$P_{in,distillers} = 8 \cdot E_0 S_{aluminium} = 35 \text{ W} \tag{6.4}$$

However, as shown previously in subsection 4.2.4, only 76,5% of this power gets into the modules because of reflective, convective and radiative losses. So, the effective thermal flux entering the first stage evaporator is equal to $P_{in,eff,distillers} = 26{,}78$ W. The overall assembly of PV+distillers is able to provide electric power and distilled water. The electric output in MPP and at $T_{cell,m} = 54{,}2$ °C, is worth $P_{mpp}(T_{cell,m}) = 6{,}9$ W. As already explained in the aforementioned subsection, to estimate the energetic output corresponding to the distillation process, the product of the latent heat of vaporization and the output of distillate of the eight distillers in the best conditions is taken into account:

$$P_{distillation} = 8 \cdot J_{exp,m} \Delta h_{LV} S_{condensation} = 24{,}88 \text{ W} \tag{6.5}$$

The aim is to define an efficiency in which both electric and distillation processes can be analyzed and compared. Hence, the feed power must be P_{solar} as it is the source of the waste heat. In this work the distillers do not cover all the cells, but in another configuration in could be possible. In subsection 4.2.4, the $GOR = P_{distillation}/P_{in,distillers} = 71{,}1\%$ was mentioned because only the distillation process was judged, however here its meaning would be inadequate. So it is defined the efficiency of *recovery* of the waste heat by the distillation process:

$$\eta_{Recovery} = \frac{P_{distillation}}{P_{solar}} = 39{,}8\% \tag{6.6}$$

Eventually, the global cogeneration efficiency of the prototype, accounting also for the electric contribution being $\eta_{PV}(T_{cell,m}) = 11\%$, is the sum of the two outputs on the incoming power:

$$\eta_{Prototype} = \eta_{Recovery} + \eta_{PV}(T_{cell,m}) = \frac{P_{distillation} + P_{mpp}(T_{cell,m})}{P_{solar}} = 50{,}8\% \tag{6.7}$$

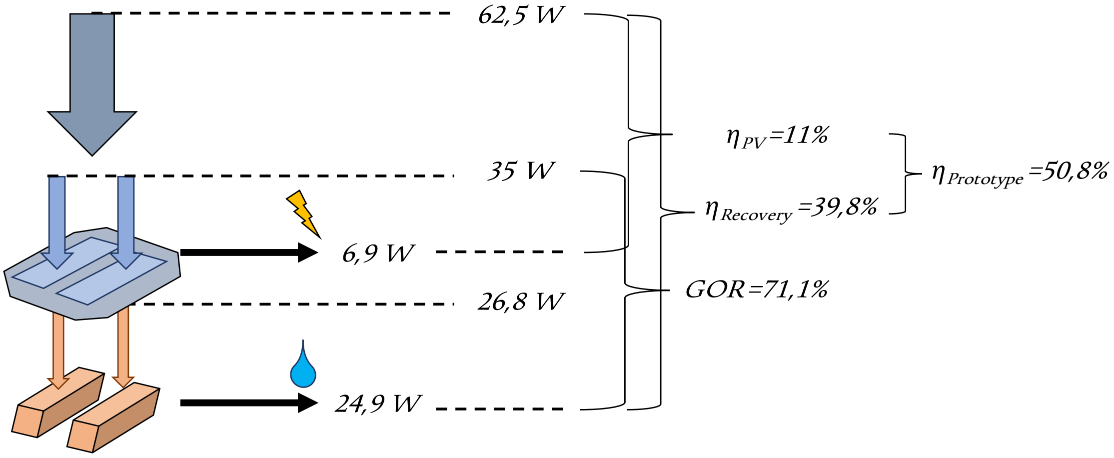

Figure 6.10: Energetic contributions to the efficiencies in the cogeneration prototype

Figure 6.10 summarizes all these contributions. $\eta_{Recovery}$ is lower than the GOR but is more representative of the true efficiency of distillation. The overall efficiency given by the PV and the distillers is satisfying.

However, from an exergetic point of view the performance is remarkably different. *"Exergy is the maximum amount of work obtainable when a thermodynamic system is brought into equilibrium from its initial state to the environmental (dead) state"* [33]. This means that the more the system is far from this *dead* state, the more is the exergy available in the process. The environmental state is defined by a thermomechanical contribution, characterized by the environmental temperature T_{amb} and pressure p_{amb}, and a chemical contribution where the concentrations, here the mass fractions $Y_{i,amb}$ of the i species of the mixture, are the same of the surrounding environment. Furthermore, not all the types of energy contain the same amount of exergy. Mechanical and electric energy can be completely transformed into *pure work*, so they are *pure exergy*. Thermal energy, in accordance with the Second Law of Thermodynamics, cannot be converted all into work but, in the best case of a Carnot's cycle made from a temperature T to the ambient, the work produced is proportional to the Carnot's factor:

$$\theta = 1 - \frac{T_{amb}}{T} \tag{6.8}$$

Therefore, θ indicates the *quality* of the thermal energy involved in the process. Chemical energy is also not completely available to produce work. Similarly to heat transfer, chemical reactions at isothermal and isobaric conditions are not reversible but follow the path indicated by the Gibbs' Free Energy, $G = H - TS$. For a chemical species i in a solution, its Gibbs' Free Energy is equal to its *chemical potential*, which is defined as:

$$\mu_i = \left(\frac{\partial G}{\partial N_i} \right)_{T,p,N_j \neq N_i} \tag{6.9}$$

The above mentioned concepts already anticipate what will be the outcome of the exergetic analysis in the following lines since the system is characterized by a distillation process driven at low temperature. For a generic open system at dead state, the exergy balance is:

$$\sum_{j=1}^{n} \Psi_j - W_t = \sum_{k=1}^{m} \dot{m}_k b_k^t + \Psi_{irr} \tag{6.10}$$

In equation 6.10, $\Psi_j = \phi_j \theta_j$ are the external heat fluxes multiplied by their Carnot's factor, i.e. the temperature at which the fluxes are provided; W_t is the mechanical work and Ψ_{irr} the irreversibility associated to the thermodynamic transformation. $\dot{m}_k$ are the mass flow rates and b_k^t are the total specific exergies (neglecting the mechanical specific energy e_m), defined as:

$$b^t = h - h^* - T_{amb}(s - s^*) + \sum_{i=1}^{q} Y_i \frac{\mu_i^* - \mu_{i,amb}}{M_i} \tag{6.11}$$

where h and s are the specific enthalpy and entropy of formation, M_i is the molar mass of species i and q is the number of species in the mixture. The superscript * defines the *restricted dead state* in which $T = T_{amb}$, $p = p_{amb}$ but $Y_i \neq Y_{i,amb}$. In the case of our system, the ambient conditions are T_{amb} = 20 °C, p_{amb} = 1 atm and $Y_{s,amb}$ = 0,035 the mass fraction of salt in saltwater. The parts of the system analyzed are the panel, the various stages of the distillers, the heat sink and eventually the entire system. The exergy balance in the control volume which encloses the PV cells is equal to:

$$\Psi_{Solar} - \Psi_{Reflective} - \Psi_{Convective} - \Psi_{Radiative} - P_{mpp} - \Psi_{in,eff,distillers} = \Psi_{irr} \tag{6.12}$$

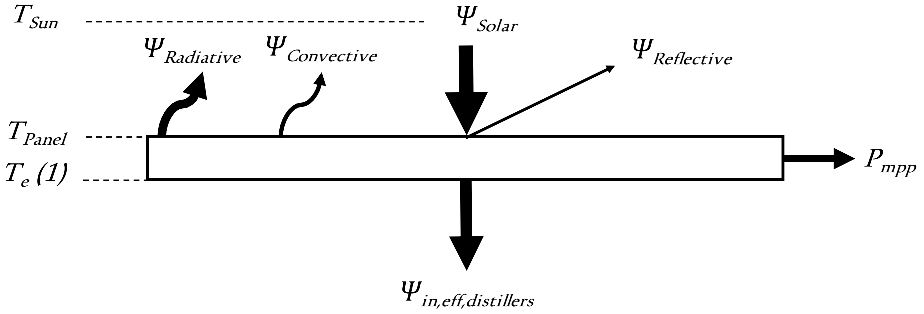

Figure 6.11: Exergetic fluxes to and from the PV cells

The assumptions made are that the panel works at MPP at $T_{cell,m}$ = 54,2 °C; Ψ_{Solar} is provided at T_{Sun} = 6000 K; exergetic losses are exchanged with the environment at T_{panel} = 60 °C and $\Psi_{in,eff,distillers} = \Psi_e(1)$ feeds the first stage at $T_e(1)$ = 46,4 °C in accordance with the simulations of this subsection and of subsection 4.2.3. For each stage j, the exergy balance is:

$$\Psi_e(j) - \Psi_c(j) + \dot{m}(j) b_{dist}^t(j) - \dot{m}(j) b_{salt}^t = \Psi_{irr} \tag{6.13}$$

The assumptions made for each stage are that the losses are negligible; the incoming exergy flux $\Psi_e(j)$ is provided at the temperature of the evaporator $T_e(j)$ and similarly for $\Psi_c(j)$ at $T_c(j)$; for stages 2 and 3, $T_c(j-1) = T_e(j)$; saltwater is provided at $T_w = T_{amb}$,

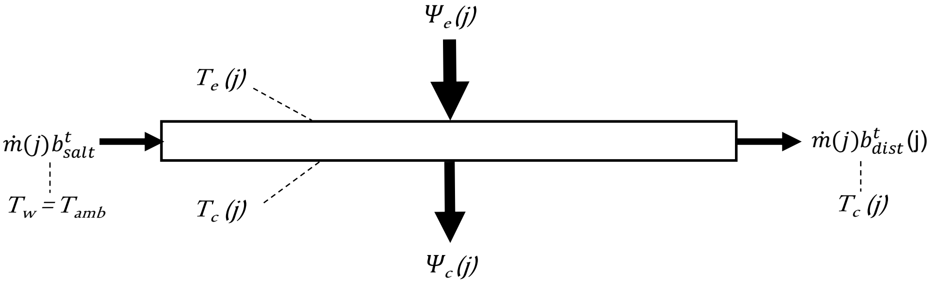

Figure 6.12: Exergetic fluxes in a single distillation stage

which means that its specific exergy is worth $b^t_{salt} = 0$, so its exergetic contribution is null; distillate goes out from the system at $T_c(j)$, contributing to the irreversibility because the remaining thermal energy is lost. The specific exergy of distillate in each stage is worth:

$$\begin{aligned} b^t_{dist}(j) = {} & h(T_c(j), Y = 0) - h(T_{amb}, Y_{s,amb}) \\ & - T_{amb}\left[s(T_c(j), Y = 0) - s(T_{amb}, Y_{s,amb})\right] \\ & + Y_{s,amb}\frac{-\mu_s(T_{amb}, Y_{s,amb})}{M_{NaCl}} \\ & + (1 - Y_{s,amb})\frac{\mu_w(T_{amb}, Y = 0) - \mu_w(T_{amb}, Y_{s,amb})}{M_w} \end{aligned} \tag{6.14}$$

where μ_s and μ_w are the chemical potentials of salt and water in saltwater respectively. For the heat sink, the balance is simple and equal to $\Psi_c(3) = \Psi_{irr}$ as all the exergy is lost to the environment. All the values employed and results are shown in detail in Appendix D.

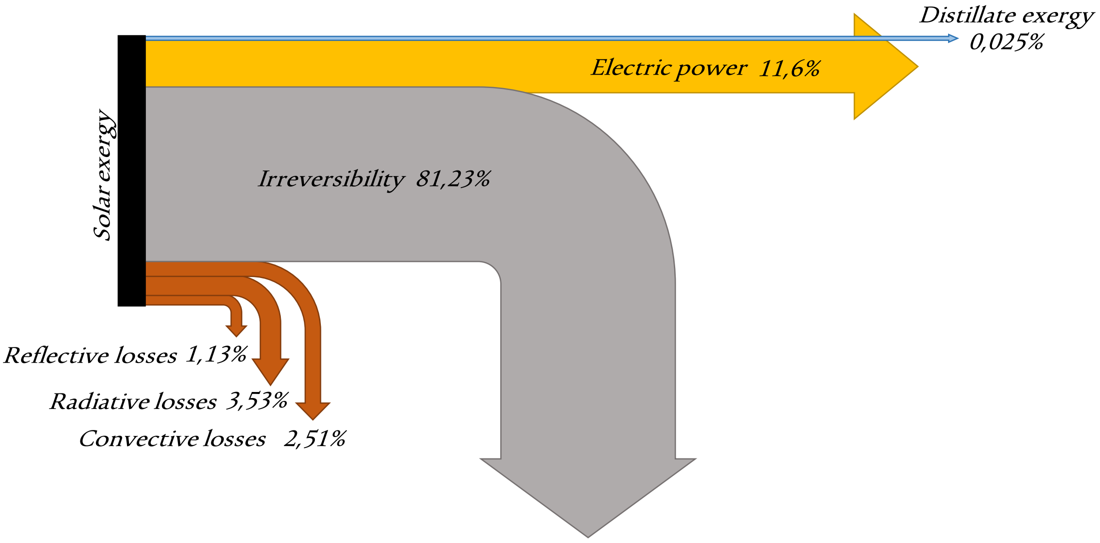

Figure 6.13: Sankey diagram of exergy flows

As represented in figure 6.13, the solar source at 6000 K carries an high value of exergy, that is used by the system at low temperatures (down to 22.5 °C in the last stage), so the system exploits a low useful exergy, which is almost due to the PV module. The distillate exergy is small because the overall flow rate is small, and because its specific exergy b^t_{dist} is small too because of the low temperature. The second law efficiency can be therefore defined as:

$$\eta_{II} = 1 - \frac{\Psi_{irr} + \Psi_{losses}}{\Psi_{feed}} \tag{6.15}$$

being listed below in table 6.3 for the panel, each stage of distillation and the system globally.

Table 6.3: Second law efficiencies in the prototype

	η_{II} [%]
Panel	15,32
Stage 1	72,36
Stage 2	58,93
Stage 3	22,61
Global	11,58

As expected, the PV panel is the least efficient from the exergy point of view. The stages show a decreasing efficiency due to the decrease in the working temperature.

In conclusion, in this subsection it has been demonstrated that this device enables the cogeneration of two completely distinct useful effects, allowing to enclose in one single system the advantages of two. Improvements on the efficiency can be obtained by increasing the distillation surface, which here is optimized for salt removal but not for productivity. Another upgrade could be achieved by increasing the number of stages, which would further increase the productivity.

Conclusion

A more sustainable water supply is a great challenge of the next decades in most countries, since freshwater scarcity outlook is worrying as the population grows and climate change starts to show its outcomes. To face water scarcity, desalination is being increasingly developed around the world. Today, more than 300 million people rely on desalinated water, whose cost has dropped by more than a half over the last three decades. [34] Still, desalination plants are economically and energetically expensive, so only wealthy countries can afford their construction.

In this work it has been shown a low-cost and sustainable alternative to large desalination facilities in cases where they cannot be built for economical reasons. Passive solar membrane distillation, as implemented here, relies only on solar energy and capillarity, is easy to be implemented with inexpensive and broadly available materials. During laboratory experiments, while replicating realistic conditions of solar irradiance (1000 W/m^2 = 1 Sun), saltwater feed temperature (20 °C) and salinity (35 g/l), a desalination rate of up to 2 l/m^2h has been achieved. The energy required by the proposed passive desalination system is competitive in comparison with other solar desalination techniques, since it requires 388 kWh/m^3 of distillate water. During continuative experiments over five days, the average productivity decreases to 1,3 l/m^2h, due to the salt accumulation in the membrane and cloths.. Furthermore, the desalination process is driven by the heat recovered from the back surface of the PV module mounted on top of the prototype, thus demonstrating the possibility to implement a cogenerative solution to water and energy needs. The prototype designed and built in this work allows a global cogeneration efficiency of 50,8%. By recovering the heat from the back of the PV modules, the distillers manage to reduce their temperature by 8 °C, thus allowing a relative PV efficiency gain of 4,5%.

All these promising results do not come without some drawbacks that must be mitigated in further realization of the prototype. First, the global distillate productivity is limited by the size and number of stages of the distillers. In this work they have been designed smaller in comparison to the available space, and with only 3 stages. Then, the productivity rate during continuative operation suffers from the phenomenon of scaling in the membranes, causing a drop of performance up to 55% during five days experiments. Membranes are also delicate and need, for the above mentioned reason or unexpected damages, to be periodically replaced, therefore adding maintenance costs and other risks related to an incorrect assembly. Other aspects that need to be overcome are the evaporation losses of distillate and the quality of the assembly, which is now too related to the skills of the operator. A new design, inspired by the achievements of this work, is needed and should solve these problems by replacing the membranes with air gap spacers, add more stages, increase the total surface of distillation, enhance PV and internal cooling, and prevent by design from an incorrect mounting of the stages' layers.

Nevertheless, new perspectives can be imagined for an evolution or even a transformation of the prototype to make it more attractive. A scale-up of the system here designed up to 1 m^2 could potentially provide the amount of drinkable water for 4 to 5 people a day (3 l/day·person for men; 2,2 l/day·person for women). [35] This desalination technique could be installed in floating installations, and could be advantageous in off-grid areas, mainly undeveloped regions or endangered communities (e.g. after natural disasters, sinking, etc.). The PV technology could be further integrated to enhance the performance and reliability over the time: the electricity from the PV could power a pump to increase the feed of saltwater or to provide the rinsing of the evaporator layers. This is a change from the original paradigm but, if the performance and durability enhancement is worth, the increase in complexity and costs could be conceivable.

Appendices

Appendix A

Solar cells technologies and efficiencies

Table A.1: Overview of single junction cells technologies tested under STC (1000 W/m^2, 25°C, AM1.5 spectrum). Reprinted from [15]

Classification	**Efficiency** [%]	**Area** [cm^2]	V_{oc} [V]	J_{sc} [mA/cm^2]	**FF** [%]	**Test Centre** (date)	**Description**
Silicon							
Si (crystalline cell)	26.7 ± 0.5	79.0	0.738	42.65	84.9	AIST (3/17)	Kaneka, n-type rear IBC
Si (multicrystalline cell)	22.3 ± 0.4	3.923	0.6742	41.08	80.5	FhG-ISE (8/17)	FhG-ISE, n-type
Si (thin transfer submodule)	21.2 ± 0.4	239.7	0.687	38.50	80.3	NREL (4/14)	Solexel (35 µm thick)
Si (thin film minimodule)	10.5 ± 0.3	94.0	0.492	29.7	72.1	FhG-ISE (8/07)	CSG solar (<2 µm on glass)
III-V cells							
GaAs (thin film cell)	28.8 ± 0.9	0.9927	1.122	29.68	86.5	NREL (5/12)	Alta Devices7
GaAs (multicrystalline)	18.4 ± 0.5	4.011	0.994	23.2	79.7	NREL (11/95)	RTI, Ge substrate
InP (crystalline cell)	24.2 ± 0.5	1.008	0.939	31.15	82.6	NREL (3/13)	NREL9
Thin film chalcogenide							
CIGS (cell)	21.7 ± 0.5	1.044	0.718	40.70	74.3	AIST (1/17)	Solar Frontier
CdTe (cell)	21.0 ± 0.4	1.0623	0.8759	30.25	79.4	Newport (8/14)	First Solar, on glass
CZTS (cell)	10.0 ± 0.2	1.113	0.7083	21.77	65.1	NREL (3/17)	UNSW12
Amorphous/microcrystalline							
Si (amorphous cell)	10.2 ± 0.3	1.001	0.896	16.36	69.8	AIST (7/14)	AIST13
Si (microcrystalline cell)	11.9 ± 0.3	1.044	0.550	28.72	75.0	AIST (2/17)	AIST
Perovskite							
Perovskite (cell)	20.9 ± 0.7	0.991	1.125	24.92	74.5	Newport (7/17)	KRICT15
Perovskite (minimodule)	16.0 ± 0.4	16.29	0.978	21.44	76.1	Newport (4/17)	Microquanta, 6 serial cells
Dye sensitised							
Dye (cell)	11.9 ± 0.4	1.005	0.744	22.47	71.2	AIST (9/12)	Sharp17
Dye (minimodule)	10.7 ± 0.4	26.55	0.754	20.19	69.9	AIST (2/15)	Sharp, 7 serial cells
Dye (submodule)	8.8 ± 0.3	398.8	0.697	18.42	68.7	AIST (9/12)	Sharp, 26 serial cells
Organic							
Organic (cell)	11.2 ± 0.3	0.992	0.780	19.30	74.2	AIST (10/15)	Toshiba
Organic (minimodule)	9.7 ± 0.3	26.14	0.806	16.47	73.2	AIST (2/15)	Toshiba (8 series cells)

Table A.2: Overview of multiple junction cells technologies tested under STC (1000 W/m^2, 25°C, AM1.5 spectrum). Reprinted from [15]

Classification	**Efficiency** [%]	**Area** [cm^2]	V_{oc} [V]	J_{sc} [mA/cm^2]	**FF** [%]	**Test Centre** (date)	**Description**
III-V multijunctions							
5 junction cell (bonded)	38.8 ± 1.2	1.021	4.767	9.564	85.2	NREL (7/13)	Spectrolab, 2-terminal
InGaP/GaAs/InGaAs	37.9 ± 1.2	1.047	3.065	14.27	86.7	AIST (2/13)	Sharp, 2-term
GaInP/GaAs (monolithic)	32.8 ± 1.4	1.000	2.568	14.56	87.7	NREL (9/17)	LG Electronics, 2-term
GaInP/GaAs/Si (mech. Stack)	35.9 ± 0.5	1.002	2.52/0.681	13.6/11.0	87.5/78.5	NREL (2/17)	NREL/CSEM/EPFL, 4-term
GaInP/GaAs/Si (wafer bonded)	33.3 ± 1.2	3.984	3.127	12.7	83.8	FhG-ISE (8/17)	Fraunhofer ISE, 2-term
GaInP/GaAs/Si (monolithic)	19.7 ± 0.7	3.943	2.323	10.0	84.3	FhG-ISE (8/16)	Fraunhofer ISE
a-Si/nc-Si multijunctions							
a-Si/nc-Si/nc-Si (thin-film)	14.0 ± 0.4	1.045	1.922	9.94	73.4	AIST (5/16)	AIST29
a-Si/nc-Si (thin-film cell)	12.7 ± 0.4	1.000	1.342	13.45	70.2	AIST (10/14)	AIST13,14

Appendix B

Results of the characterization of the solar module

Table B.1: Irradiance uniformity test: values in [W/m^2] of the five points measured during 10 s (sampling time = 1 s), and mean value with standard deviation. See figure 3.4 for the position of the different testing points.

Time [s]	**C**	**D - L**	**D - R**	**U - L**	**U - R**	**Average**
1	1007,4	1019,1	996,8	1012,8	1004,4	
2	1007,1	1019,3	997,4	1016,1	1004,8	
3	1007,1	1019,2	997,9	1017,0	1005,3	
4	1007,3	1019,2	998,2	1017,2	1005,9	
5	1007,4	1019,6	998,5	1017,5	1006,0	
6	1007,7	1019,7	998,3	1017,9	1005,9	
7	1007,5	1019,8	998,4	1018,1	1006,1	
8	1007,6	1019,7	999,1	1018,4	1006,2	
9	1007,5	1019,8	998,9	1018,6	1006,2	
10	1007,1	1020,1	998,5	1018,4	1006,5	
	1007,4	1019,6	998,2	1017,2	1005,7	**1009,6 ± 8,8**

Table B.2: Mean temperatures [°C] recorded by the thermocouples during STC tests 1, 2 and 3

Thermocouple	**Test 1**	**Test 2**	**Test 3**
T0	23,9	23,7	24
T1	24,8	25,2	25,1
T2	24,4	24,5	24,6
T3	25,8	25,9	26,2
T4 – air	33,3	34,4	33,9

Table B.3: Mean temperatures [°C] recorded by the thermocouples during each step of temperature rise, open-circuit voltages and temperature coefficient's values. 40 s recording of temperature for each step. Constant irradiance $E = 1000$ W/m^2. Reference temperature $T_0 = 25$ °C.

Thermocouple	**Step 12 °C**	**Step 15 °C**	**Step 20 °C**	**Step 25 °C**
T0	26,4	28,5	32	35,4
T1	28,5	30,2	32,6	36,3
T2	27,5	29,6	32,8	36,8
T3	28,7	30,7	34	37,5
$\boldsymbol{T_{mean,cell}}$	27,8	29,7	32,8	36,5
$\boldsymbol{V_{oc}[V]}$	2,640	2,630	2,607	2,583
$\boldsymbol{k_V}$ **[V/°C]**	-0,00501	-0,00507	-0,00600	-0,00617

Table B.4: Characteristics of Solbian® Energy Flyer™ panel. Values provided by Solbian's technical director. The panel has 4 SunPower® cells connected in series like the panel used in this work.

$\boldsymbol{P_{mpp}}$ **[W]**	12,5
$\boldsymbol{k_V}$ **[V/°C]**	-0,0072
$\boldsymbol{k_I}$ **[A/°C]**	0,0026
$\boldsymbol{R_s}$ **[Ω]**	0,1
$\boldsymbol{R_{sh}}$ **[Ω]**	1500

Table B.5: XDISC® ASOLE-13 technical datasheet

$\boldsymbol{V_{oc}}$ **[V]**	2,72
$\boldsymbol{I_{sc}}$ **[A]**	4,72
$\boldsymbol{V_{mpp}}$ **[V]**	2,32
$\boldsymbol{I_{mpp}}$ **[A]**	4,44
$\boldsymbol{P_{mpp}}$ **[W]**	10,3
$\boldsymbol{k_V}$ **[V/°C]**	-0,0084
$\boldsymbol{k_I}$ **[A/°C]**	0,0019
$\boldsymbol{k_P}$ **[W/°C]**	-0,041

Figure B.1: Temperature recording during tests 1, 2 and 3. Time sample: 2 s. Length of Test 1: 36 min 40 s; Length of Test 2: 23 min 20 s; Length of Test 3: 20 min 00 s. Highlighted interval: functioning under short-circuit or near conditions. Note the different behavior in temperature rise for T1 and T2.

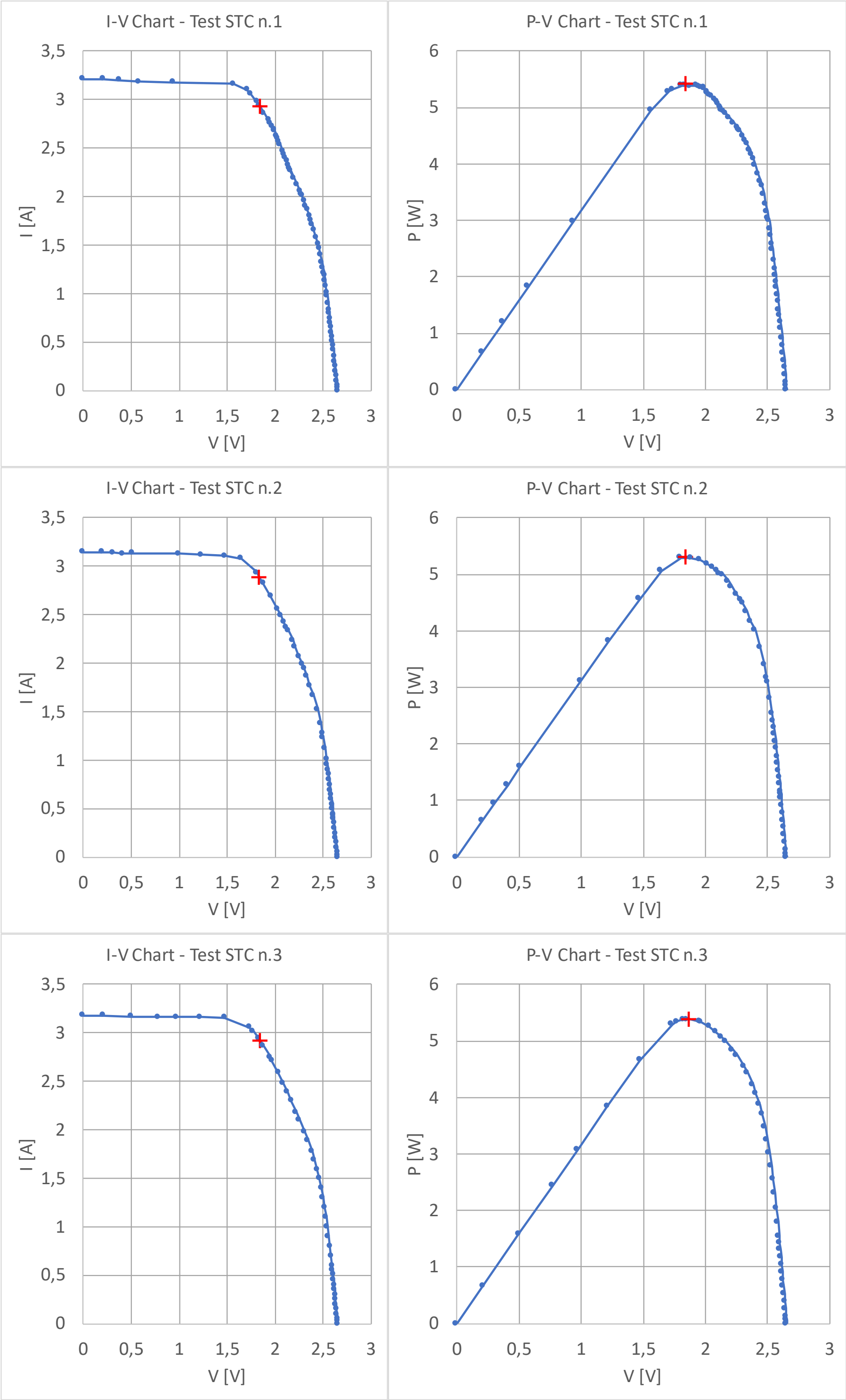

Figure B.2: $I - V$ and $P - V$ charts for STC tests 1, 2 and 3 with highlighted maximum power points. Number of points measured for Test 1: 72; Test 2: 53; Test 3: 47.

Appendix C

Results of the characterization of the passive distiller

Table C.1: Heat flux calibration and uniformity test: values in [W/m^2] of the nine points measured during 10 s (time sample = 1 s), and mean value with standard deviation. See figure 4.3 for the position of testing points.

Time [s]	**C**	**U**	**U - R**	**R**	**D - R**	**D**	**D - L**	**L**	**U - L**	**Average**
1	965,6	972,1	1050,4	976,2	1070,8	964,4	1060,9	930,7	1034,1	
2	965,5	972,2	1050,1	976,3	1070,6	964,0	1061,1	930,5	1034,1	
3	965,7	972,5	1050,0	976,1	1070,5	964,0	1061,3	930,5	1034,0	
4	965,8	972,7	1049,8	976,1	1070,3	964,0	1061,5	930,3	1034,0	
5	965,9	972,6	1049,8	976,2	1070,3	963,5	1061,0	929,7	1034,1	
6	965,9	972,4	1049,7	976,6	1070,5	962,9	1060,8	929,2	1033,9	
7	965,8	972,4	1049,6	976,8	1070,5	962,3	1060,8	928,8	1033,7	
8	965,8	972,4	1049,6	976,8	1070,3	961,9	1060,8	929,2	1033,9	
9	965,9	972,4	1049,6	976,7	1070,1	961,8	1060,8	929,7	1033,4	
10	965,5	972,6	1049,4	976,8	1070,1	961,8	1060,3	929,7	1033,4	
	965,8	972,4	1049,8	976,4	1070,4	963,2	1061,0	929,9	1033,9	**1002,5 ± 51,3**

Table C.2: Heat fluxes in the panel's control volume

	q [W/m^2]
Solar	1000
Radiative	-156,6
Convective	-111,5
Reflective	-50
Border	83
in	764,9

Table C.3: Evaluation of lateral convective exchange on the distiller's layers

Layer	P_l [mW]	q_l [W/m^2]
Al 1	-22,85	-5,22
Evap 1	-4,88	-1,12
Mem 1	-1,92	-0,61
Cond 1	-9,9	-3,17
Al 2	-7,52	-1,72
Evap 2	-1,28	-0,29
Mem 2	-0,13	-0,04
Cond 2	4,52	1,45
Al 3	8,04	1,84
Evap 3	2,38	0,54
Mem 3	1,72	0,55
Cond 3	19,51	6,24
Al 4	24,33	5,56
Total	12,02	4,01

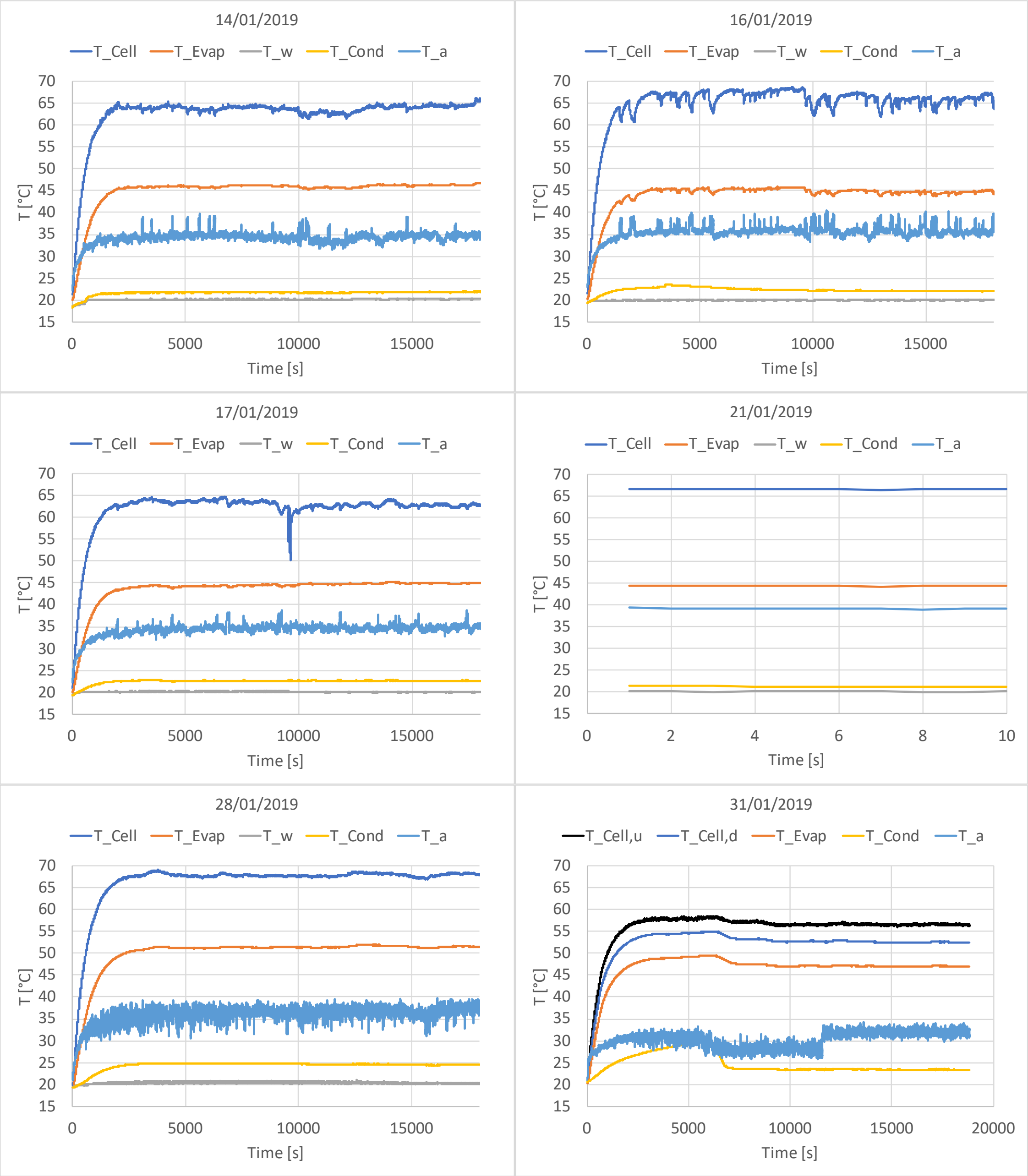

Figure C.1: Characteristic temperatures of the distiller during different tests: During test 28/01 an issue in the recording occurred which had been noticed only at the end; In test 31/01 the temperature of the cell was measured at the boundary of the distiller on top and at the bottom of the panel, furthermore the refrigerated circulator was turned on after 6000 s.

Appendix D

Results of prototype testing

Table D.1: Heat flux calibration and uniformity test: values in [W/m^2] of the nine points measured during 10 s (time sample = 1 s), mean value and standard deviation. See figure 6.3 for testing points representation

Time [s]	**C**	**D - L**	**D - R**	**D**	**L**	**R**	**U - L**	**U - R**	**U**	**Average**
1	1007,9	1049,2	1041,2	905,5	1026,3	978,2	1141,7	1121,2	1024,7	
2	1008,0	1050,3	1042,2	905,0	1026,1	976,0	1143,0	1120,6	1022,3	
3	1008,4	1050,7	1043,7	904,6	1027,0	974,9	1143,0	1121,6	1020,6	
4	1008,4	1051,1	1044,1	904,5	1026,1	974,3	1143,4	1121,7	1019,2	
5	1008,6	1051,3	1043,1	904,3	1026,7	973,5	1141,5	1122,3	1018,5	
6	1008,6	1051,6	1043,5	904,4	1027,0	973,5	1142,6	1123,3	1018,4	
7	1008,5	1052,8	1043,6	904,5	1026,6	973,6	1142,2	1124,0	1018,0	
8	1008,6	1052,4	1043,9	904,1	1027,4	972,7	1142,3	1125,8	1017,5	
9	1009,0	1051,3	1042,9	903,7	1027,7	972,7	1140,6	1126,3	1017,8	
10	1008,3	1050,6	1043,5	903,7	1027,4	973,0	1140,6	1127,9	1017,9	
	1008,4	1051,1	1043,2	904,4	1026,8	974,2	1142,1	1123,5	1019,5	**1032,6 ± 71,9**

Table D.2: Flow rates of the eight modules, mean values per day and per module and global mean value: flow rates are not estimated during failures as they constitute outliers, thus average calculations exclude modules *E* and *G*.

Flow rate	**6/05**	**7/05**	**8/05**	**9/05**	**10/05**	**Average** l/m^{2}h>
A	2,134	1,300	1,177	1,246	0,795	1,330±0,491
B	1,970	1,446	1,379	1,340	0,896	1,406±0,382
C	2,383	1,321	1,246	0,633	0,454	1,207±0,757
D	2,014	1,078	0,924	0,931	0,888	1,167±0,479
E	1,798	1,410	x	x	x	x
F	2,136	1,650	1,030	1,470	1,443	1,546±0,400
G	x	x	x	x	x	x
H	1,747	1,212	0,806	0,998	0,976	1,148±0,365
Average	2,026±0,218	1,345±0,182	1,094±0,213	1,103±0,308	0,909±0,320	1,301±0,318

Table D.3: Temperature differentials and mean temperatures between evaporator 1 and condenser 3 along the five days campaign and average values. Average values after steady state are considered after 1 h.

T [°C]	**6/05**	**7/05**	**8/05**	**9/05**	**10/05**	**Average**
ΔT_A	22,24	22,75	22,91	23,40	22,75	22,81
ΔT_B	20,74	21,51	21,54	22,91	21,10	21,56
ΔT_G	17,19	18,99	16,65	18,44	18,06	17,86
ΔT_H	19,73	21,83	21,16	22,17	22,62	21,50
T_{mA}	34,11	34,19	33,29	35,10	33,97	34,13
T_{mB}	33,03	33,09	32,70	33,67	32,94	33,09
T_{mG}	34,00	34,21	32,86	33,99	33,86	33,78
T_{mH}	35,35	35,54	34,51	34,54	35,26	35,04

Table D.4: Temperature of cells 1, 2, 3, 4 of the PV module in uncooled conditions and air: mean values calculated considering the steady state reached after 4 min.

	T [°C]
1	59,33
2	55,63
3	69,4
4	65,4
Average	62,4
Air	34,43

Table D.5: Temperatures of cell 1 and 4, their mean value and mean temperature of evaporators 1 along the five days campaign and average values. Average values after steady state are considered after 1 h.

T [°C]	**6/05**	**7/05**	**8/05**	**9/05**	**10/05**	**Average**
T_{c1}	56,08	56,64	55,92	58,70	58,13	57,10
T_{c4}	64,63	61,36	59,70	60,59	61,78	61,61
$\boldsymbol{T_{c14,m}}$	60,36	59,00	57,81	59,64	59,95	59,35
$T_{ev1,m}$	44,11	44,89	43,62	45,19	44,58	44,48

Table D.6: Magnitudes for the calculation of the specific exergy of distillate for each stage: values obtained from [33].

Stage j	**1**	**2**	**3**
$h(T_c(j), Y = 0)$ [kJ/kg]	162,5	129,2	94,0
$h(T_{amb}, Y_{s,amb})$ [kJ/kg]	84,0	84,0	84,0
$s(T_c(j), Y = 0)$ [kJ/kgK]	0,556	0,448	0,330
$s(T_{amb}, Y_{s,amb})$ [kJ/kgK]	0,296	0,296	0,296
$\mu_s(T_{amb}, Y_{s,amb})$ [kJ/kg]	68,5	68,5	68,5
$\mu_w(T_{amb}, Y = 0)$ [kJ/kg]	-2,902	-2,902	-2,902
$\mu_w(T_{amb}, Y_{s,amb})$ [kJ/kg]	-5,45	-5,45	-5,45
$b^t(j)$ [kJ/kg]	2,467	0,873	0,101

Table D.7: Fluxes, Carnot’s factors and Exergies in the prototype

	ϕ [W]	θ	Ψ [W]
Panel			
Solar	62,5	0,951	59,5
Reflective	5,6	0,12	0,7
Convective	12,4	0,12	1,5
Radiative	17,5	0,12	2,1
Irreversibility	x	x	46,1
Stage 1			
e(1)	26,8	0,083	2,21
c(1)	26,8	0,06	1,61
Irreversibility	x	x	0,61
Stage 2			
e(1)	26,8	0,06	1,61
c(1)	26,8	0,036	0,95
Irreversibility	x	x	0,66
Stage 3			
e(1)	26,8	0,036	0,95
c(1)	26,8	0,008	0,22
Irreversibility	x	x	0,74
Heat sink			
Irreversibility	x	x	0,22

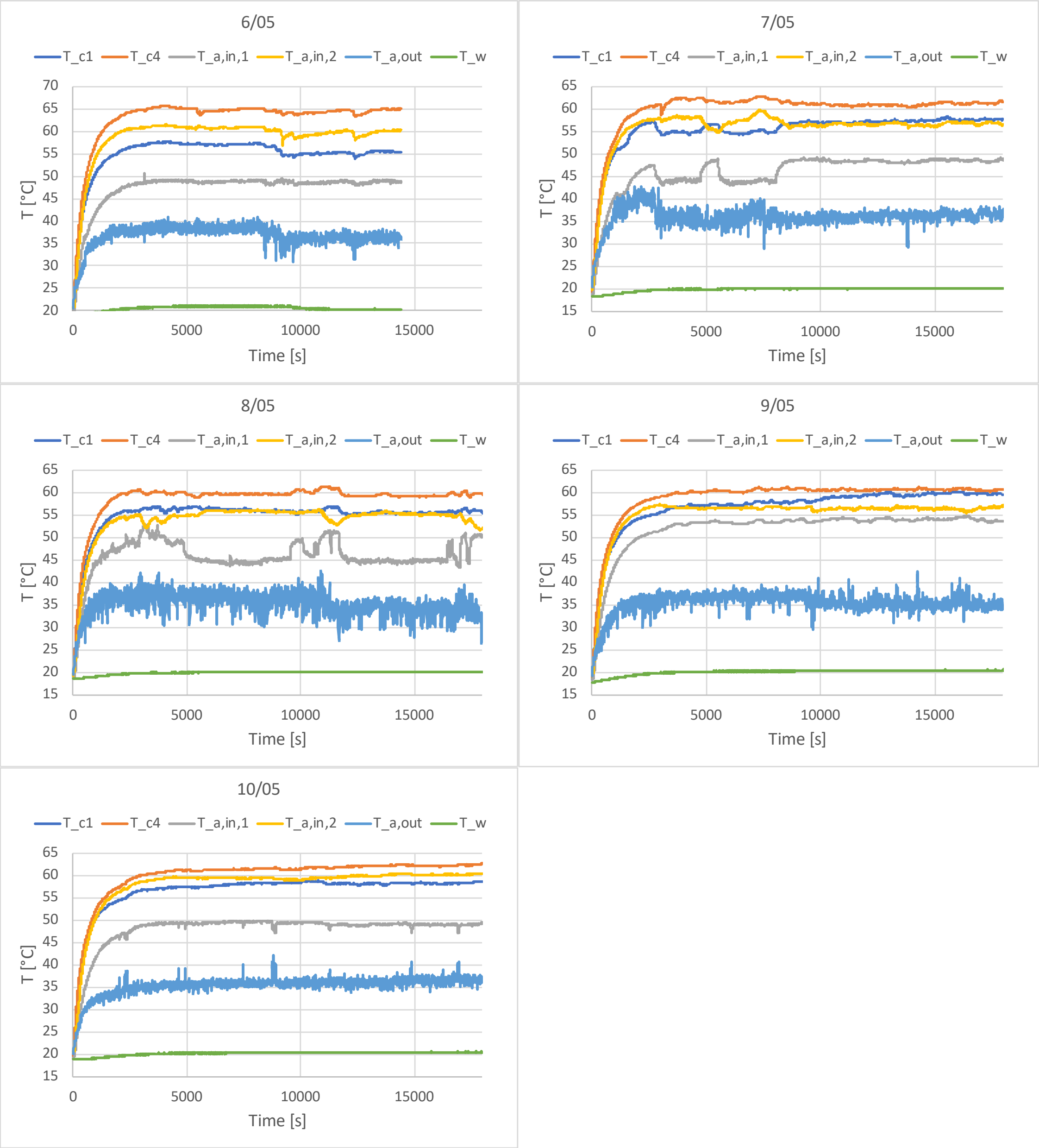

Figure D.1: Characteristic temperatures of the prototype during the tests: recordings of cells 1 and 4, air inside the device in upper (1) and bottom (2) parts, air outside above the panel and water.

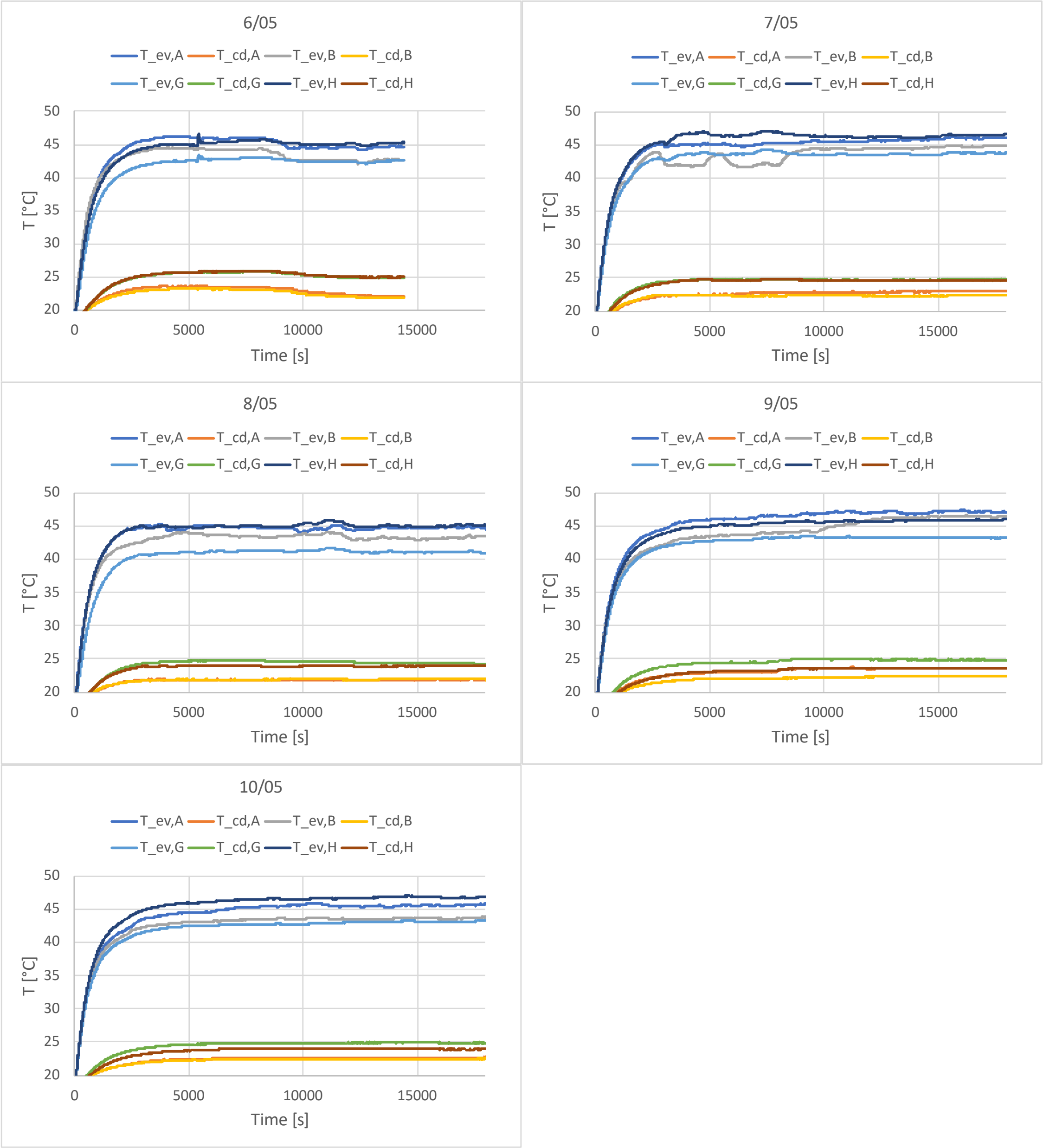

Figure D.2: Characteristic temperatures of four out of eight distillers of the prototype during the tests: recordings of evaporator 1 and condenser 3 of modules A, B, G and H.

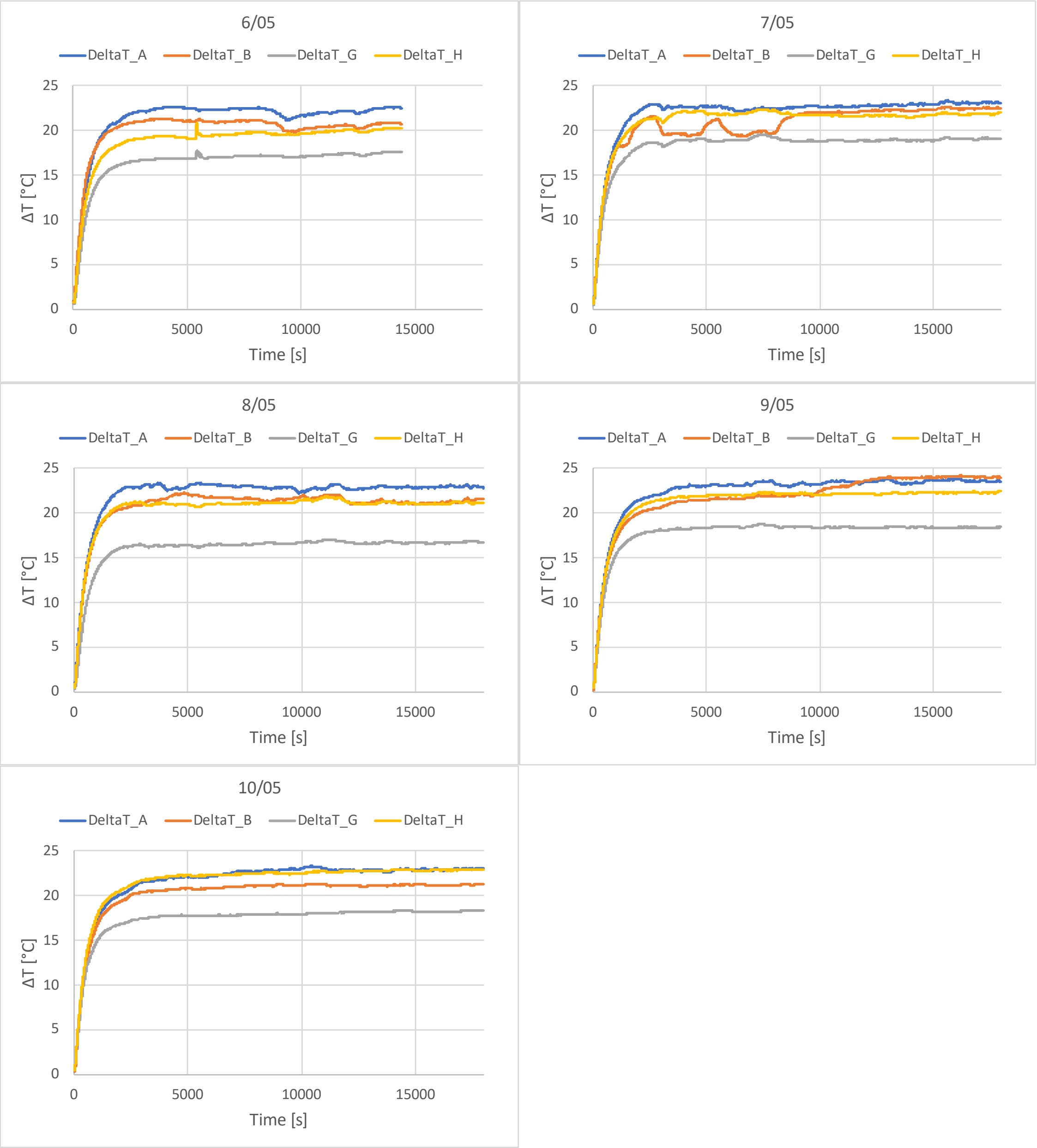

Figure D.3: Temperature differentials of four out of eight distillers of the prototype during the tests: recordings of modules A, B, G and H.

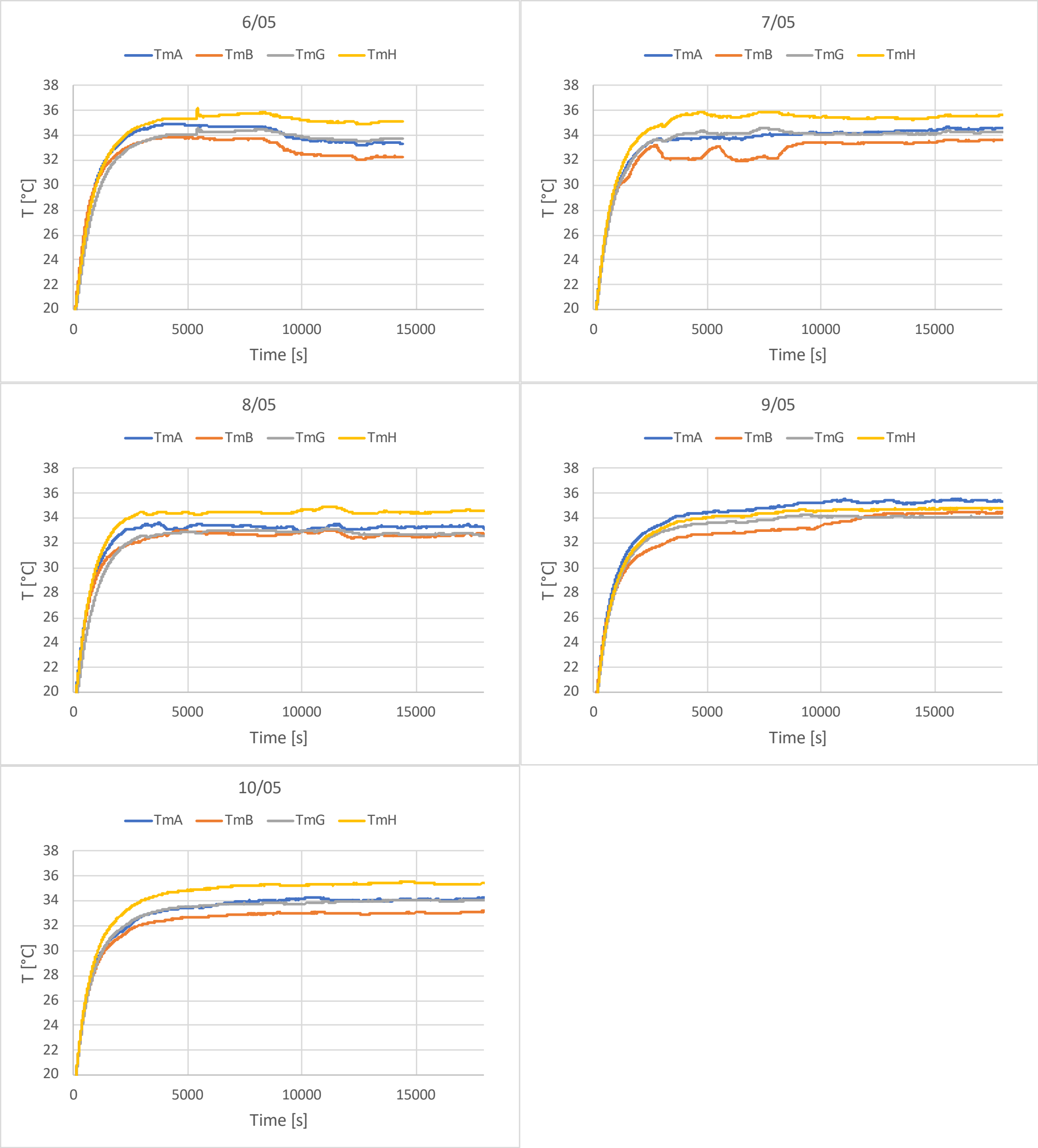

Figure D.4: Mean temperatures of four out of eight distillers of the prototype during the tests: recordings of modules A, B, G and H.

Bibliography

[1] www.fao.org/nr/water/aquastat

[2] www.unwater.org

[3] *Sustainable Development Goal 6: Synthesis Report 2018 on Water and Sanitation* United Nations, p. 18–20, 2018.

[4] Tsao J., Lewis N., Crabtree G., *Solar FAQs*, Sandia National Laboratories, 2005.

[5] MacKay D.J.C., *Solar energy in the context of energy use, energy transportation and energy storage*, Philosophical Transactions of the Royal Society A: Mathematical, Physical and Engineering Sciences, 2013.

[6] Chiavazzo E., Morciano M., Viglino F., Fasano M., Asinari P., *Passive solar high-yield seawater desalination by modular and low-cost distillation*, Nature Sustainability, Vol. 1, p. 763–772, 2018.

[7] Neamen D.A., *Semiconductor Physics and Devices: Basic Principles*, Third Edition, McGraw-Hill, p. xii–xiii, 2003.

[8] Fraas L.M., *Low-Cost Solar Electric Power*, Springer, Chapter 1, 2014.

[9] Solanki C.S., *Solar Photovoltaics: Fundamentals, Technologies and Applications*, Third Edition, PHI Learning Private Limited, 2015.

[10] Oku T., *Solar Cells and Energy Materials*, De Gruyter, p.31–41, 2017.

[11] Vossier A., Hirsch B., Gordon J.M., *Is Auger recombination the ultimate performance limiter in concentrator solar cells?*, Applied Physics Letters 97, 193509, 2010.

[12] Villalva M.G., Gazoli J.R., Ruppert F.E., *Modeling and circuit-based simulation of photovoltaic arrays*, Brazilian Journal of Power Electronics, Vol. 14, no. 1, pp. 35–45, 2009.

[13] Nayak B.K., Mohapatra A., Misra B., *Non Linear I-V Curve Of PV Module: Impacts On MPPT And Parameters Estimation*, International Journal of Engineering Research Technology, Vol. 1, Issue 8, October - 2012.

[14] Ranabhat K., *An Introduction to Solar Cell Technology*, Journal of Applied Engineering Science, Vol. 14, p. 481–491, 2016.

[15] Green M.A., Hishikawa Y., Dunlop E.D., Levi D.H., Hohl-Ebinger J., Ho-Baillie A.W.Y., *Solar cell efficiency tables (version 51)*, Prog Photovolt Res Appl. 2018;26:3–12.

[16] Fisher G., Seacrist M.R., Standley R.W., *Silicon Crystal Growth and Wafer Technologies*, Proceedings of the IEEE, Vol. 100, p. 1454–1474, 2012.

[17] www.addisonengineering.com/about-wafers.html

[18] Jordan D.C., Kurtz S.R., *Photovoltaic Degradation Rates: An Analytical Review*, National Renewable Energy Laboratory, 2012.

[19] Kalogirou S.A., *Seawater desalination using renewable energy sources*, Progress in Energy and Combustion Science n. 31, p. 242–281, 2005.

[20] Alkaisi A., Mossad R., Sharifian-Barforoush A., *A review of the water desalination systems integrated with renewable energy*, Energy Procedia n. 110, p. 268–274, 2017.

[21] Zotalis K., Dialynas E.G., Mamassis N., Angelakis A.N., *Desalination Technologies: Hellenic Experience*, Water, n. 6, p. 1134–1150, 2014.

[22] Kumar P. V., Kumar A., Prakash O., Kumar Kaviti A., *Solar stills system design: A review*, Renewable and Sustainable Energy Reviews, n.51, p.153–181, 2015.

[23] Sethi S., Wetterau G., *AWWA Manual M61*, American Water Works Association, Chapter 1, 2011.

[24] *Water Desalination Using Renewable Energy: Technology Brief*, IEA-ETSAP and IRENA© Technology Brief I12 – March 2012

[25] Alkhudhiri A., Darwish N., Hilal N., *Membrane distillation: A comprehensive review*, Desalination n. 287, p.2–18, 2012.

[26] Deshmukha A., Elimelech M., *Understanding the impact of membrane properties and transport phenomena on the energetic performance of membrane distillation desalination*, Journal of Membrane Science, n.539, p. 458–474, 2017.

[27] Khayet M, Matsuura T, *Membrane Distillation: Principles and Applications*, Elsevier, Chapter 11, 2011;

[28] Yun Y., Mab R., Zhang W., Fane A.G., Li J., *Direct contact membrane distillation mechanism for high concentration NaCl solutions*, Desalination, n.188, p.251–262, 2006.

[29] Rekioua D., Matagne E., *Optimization of Photovoltaic Power Systems: Modelization, Simulation and Control*, Springer, p.72–74, 2012.

[30] Attivissimo F., Di Nisio A., Spadavecchia M., *Validation of a Photovoltaic Electrical Model against Experimental Data*, IEEE International Instrumentation and Measurement Technology Conference, 978-1-4577-1772-7, 2012.

[31] Slavinec M., Repnik R., Klemenčič, *The impact of moisture on thermal conductivity of fabrics*, ANALI PAZU, 6/ 2016/1-2, str. 8-12.

[32] Thomas K.E., *Overview of Village Scale, Renewable Energy Powered Desalination*, National Renewable Energy Laboratory, U.S. Department of Energy, 1997.

[33] Lienhard V J.H., Mistry K.H., Sharqawy M.H., Thiel G.P., *Thermodynamics, Exergy, and Energy Efficiency in Desalination Systems* Desalination Sustainability: A Technical, Socioeconomic, and Environmental Approach, Chpt. 4, Elsevier Publishing Co., 2017. ISBN: 978-0-12-809791-5.

[34] Robbins J., *As Water Scarcity Increases, Desalination Plants Are on the Rise*, Yale Environment 360, Yale School of Forestry & Environmental Studies, 2019.

[35] *Panel on Dietary Reference Intakes for Electrolytes and Water. Dietary reference intakes for water, potassium, sodium, chloride, and sulfate / Panel on Dietary Reference Intakes for Electrolytes and Water, Standing Committee on the Scientific Evaluation of Dietary Reference Intakes, Food and Nutrition Board.*, Institute of Medicine (U.S.), Chapter 1, 2005.